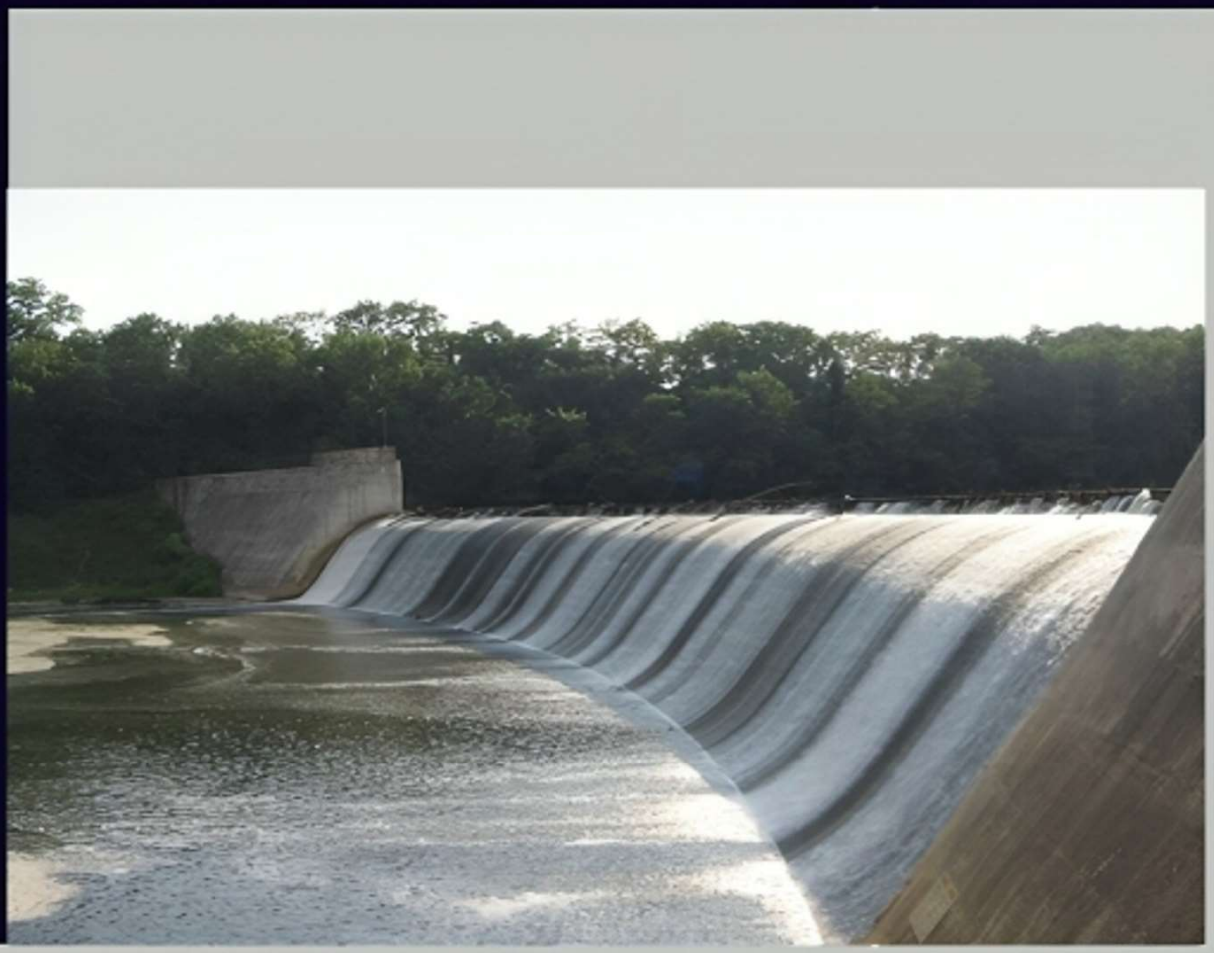
Iranian Hydraulic Association

Shahid Chamran University of Ahvaz

Journal of Hydraulic Structures

Scientific Professional Journal



October 2025
Volume 11, Issue 4

ISSN (Online): 2345-4156
https://jhs.scu.ac.ir/

Aims and Scope

Journal of Hydraulic Structures is an interdisciplinary journal which publishes high-quality peer-reviewed articles addressing the latest developments and applied methods in analysis and design, construction, maintenance, management, and operation policy of Hydraulic Structures.

The Journal aims at providing an efficient route to fast-track publication, within 10-12 weeks after manuscript submission.

The general areas covered by the Journal include:

- Advances in numerical and analytical methods applicable to hydraulic structures
- Hydro informatics and soft computing
- Hydraulic aspects of hydraulic structures
- Applied surface and subsurface hydrology and hydrometeorology
- Forecasting approaches in water resources engineering
- Economic and social aspects of hydraulic structures
- Uncertainty analysis and risk management in hydraulics and water resources engineering
- Application of Nanotechnology in hydraulic structures
- Geotechnics of hydraulic structures
- Damage detection techniques
- Technical and methodological advances in application, design/selection, production, construction materials of hydraulic structures.
- Application of Artificial Intelligence techniques in all aspects of hydraulic structures.

General Information:

Title: Journal of Hydraulic Structures

Publisher: Shahid Chamran University of Ahvaz

ISSN (Print): 2345-413X

ISSN (Online): 2345-4156

Website: https://jhs.scu.ac.ir/

Address: Faculty of Civil Engineering and Architecture, Shahid Chamran University of Ahvaz, Ahvaz, Iran

Email: jhs@scu.ac.ir

Journal of

Hydraulic Structures

Shahid Chamran University of Ahvaz

Director-in-Charge: Prof. Ali Haghighi

Editor-in-Chief: Prof. Hamid R. Ghafouri

Managing Editor: Dr. Amir H. Shafiee

Contents:

01

Studying the impact of climate change on hydroelectric energy production (Case study: Karun 4 Dam)

Ferdous Karimi Alkoohi; Hosein Ghorbanizadeh Kharrazi; Seyyed Mahmood Jazayeri Moghaddas; Mohsen Solimani babarsad; Saeb Khoshnavaz Koumleh

16

Application of Intelligent Models in Investigating the Energy Dissipation in Labyrinth Weirs with Various Cycles Form

Hamidreza Abbaszadeh; Reza Tarinejad; John Abraham

33

Placement of data transmission equipment in the flood warning system based on the Internet of Things (case study : Jiroft Dam Basin)

Marzieh Mohseni; Amineh Naseri; leila sheikhmamoo

47

Analysis of Supply Chain Risks in Concrete Dam Construction

Mohammad Mirzaahmadi; Hamed Sarkardeh; Ali Katebi; Ayda Mirzaahmadi

57

Optimizing Minor Drainage Tunnel Position to Mitigate Groundwater Inflow in Main Tunnel Projects

Hadi Farhadian

68

An Experiment on the Effect of Sills with Orifices Under a Sluice Gate on Energy Dissipation and Hydraulic Jump

Rasoul Daneshfaraz; Reza Norouzi; Behnaz Akhondi; Mehdi Djahanghiri

Studying the impact of climate change on hydroelectric energy production (Case study: Karun 4 Dam)

Ferdous Karimi Alkoohi [1], Hossein Ghorbanizadeh Kharrazi [*,1] ,Mohsen Soleimani Babarsad [1], Seyed Mahmood Jazayeri Moghaddas [1],Saeb Khoshnavaz Koumleh [1]

1. Water and Environmental Sciences Research Center, Shoushtar branch,Islamic Azad University, Shoushtar, Iran.

***Corresponding Author:**
Hossein Ghorbanizadeh Kharrazi,

Email: h.ghorbanizadeh@gmail.com
Received: 2025.01.03
Accepted: 2025.01.28
J. Hydraul. Struct., 2025; 11(4):1-15
DOI: 10.22055/jhs.2025.48662.1333

ABSTRACT

In this manuscript, the primary goal is to assess how climate change affects the accessibility and fluctuation of aquatic reserves, which directly impacts the performance and reliability of hydroelectric energy production. The study aims to understand changes in precipitation patterns, snowmelt timings, and extreme weather events, which influence river flow dynamics, reservoir levels, and overall energy generation capacity. It also seeks to identify adaptive strategies to mitigate negative impacts and ensure sustainable hydropower development in the face of a changing climate. This study evaluates the performance of the Karun 4 Dam power plant, one of the country's most critical electricity generation facilities, under the impacts of climate change. A multi-criteria decision-making approach (TOPSIS) was used to identify the most reliable General Circulation Models (GCMs) and reduce uncertainty. Additionally, the IHACRES conceptual model was employed to simulate the runoff process, while the Differential Evolution (DE) algorithm was applied to optimize hydropower energy production. The findings show a projected temperature increase from 2040 to 2061 of 1.95°C and 2.34°C under the RCP 4.5 and RCP 8.5 scenarios, respectively, compared to the baseline period (1984-2005). Furthermore, the study predicts a reduction in inflow runoff to the Karun 4 reservoir by an average of 19% and 43% under the aforementioned scenarios. Based on the results, the decrease in reservoir inflow in future periods is expected to reduce annual electricity production by 9% under the RCP 4.5 scenario and 18% under the RCP 8.5 scenario relative to the plant's nominal capacity.

KEYWORDS
Climate Change, Hydropower Energy, Reservoir Operation, Uncertainty, Karun 4 Dam.

1. Introduction

Produced and consumed energy sources, especially renewable energy sources, have a very important value. Renewable energy sources such as solar, wind, hydro, and geothermal energy are sustainable methods that provide about 14% of the world's energy needs [1] [2] Among the stated options, hydroelectric power plants are known as the most important source of renewable energy due to their unique nature [3]. Switching from fossil fuels to renewable energy sources is essential for attaining global environmental sustainability. [4]. The current movement is further bolstered by transformations noted in geopolitical dynamics., which have led to disruptions in the supply chains of conventional fuels.

For instance, the 2022 conflict in Ukraine has demonstrated that natural gas is not a viable interim fuel for transitioning to a fully renewable energy system, particularly when its supply is unreliable. It has been stated that a worldwide Reducing carbon emissions in power systems is essential to meet the United Nations Sustainable Development Goals and the objectives of the Paris Agreement. [5] [6]. According to recent World Bank estimates, Out of the 38 countries in the Organization for Economic Co-operation and Development, fewer than 25% of their electricity is generated from ref14renewable sources. However, there are considerable variations among these countries. Wind, solar, and hydropower are acknowledged as the primary sources of variable renewable energy (VRES) due to their global availability and technological advancement. Also in a review climate change has significant impacts on hydropower potential, freshwater fisheries, and hydrological responses in snow-dominated basins. It discusses how global warming affects precipitation patterns, leading to earlier spring snowmelt and changes in river flow dynamics. The article highlights that small-scale, high-altitude hydropower reservoirs are especially susceptible to temperature variations. It also highlights the importance of considering these impacts for future hydropower projects and water resource management.[8]. Nevertheless, their variability is a challenge that scientists are working to address in order to enhance their contribution to power grids. [9]. While hydroelectric power plants have many advantages over fossil fuels and other renewable sources, they are directly dependent on the amount of water flow and are very sensitive to weather conditions. Therefore, the survival of hydropower projects in the current or planned state is affected by climate changes and spatial-temporal changes in river flow [10] [11]. The International Energy Agency has identified the reduction of access to water as one of the major risks associated with climate change for the energy sector. So, the effects of climate change could cause serious problems in future hydropower plant plans, making them unjustifiable from an economic point of view. Therefore, it is necessary to conduct studies on the effects of climate change during the useful life of the hydroelectric dam, with the results being vital in the long-term management of the dam and the production of hydroelectric energy [12].

In their study, Zapata et al. used two integrated evaluation models of data from four climate models to analyze the effects of climate change on global and regional energy consumption under two RCP 2.6 and RCP 6 scenarios [10]. The general results of this study pointed out a reduction in the use of fossil fuel resources for most regions, especially North America and Europe, under the RCP 6 scenario. It was also noted that under the RCP 6 scenario in Asia, except for China and India, climate change will increase the use of hydroelectric and wind energy. Emphasizing the share of renewable energy in the energy market and its increasing growth, Bhatt et al. investigated the impact of climate change on renewable energy production through new criteria [13]. Craig et al.'s study titled "Overcoming the Communication Gap Between Energy System and Climate Modeling" stated that since a system model's energy is the basis for decision-making by energy system planners and operators, energy system modeling has faced a transformation due to changes in weather conditions caused by climate change [14]. When Mirani et al. evaluated hydroelectric energy production and exploitation of the Kesem dam reservoir under the influence of climate change using a HEC-HMS hydrological model to estimate the river flow and the outputs of the MODSIM 8.1 simulator model using the information of RCP 4.5 climate scenario, they determined that the average production of hydroelectric energy will decrease by 0.64% in the short term (2050-2021) and 0.82% in the long term (2051-2080). Also,

in the case of the RCP 8.5 climate scenario, it was found that energy production will decrease by 1.06% and 1.35% in the short term and long term, respectively. Even the RCP 4.5 scenario showed high energy production fluctuations in this basin and decreased energy production [15]. Acknowledging the lack of research on the impact of future stream drought on hydropower generation in China, Zhao and colleagues created a model to predict future hydropower output. Their research incorporated four global hydrological models and four global climate models across two emission scenarios. Findings revealed that, in comparison to the base period of 1951 to 2005, over 25% of hydropower plants are projected to see a 20% reduction in energy production relative to the base period average. [7].

Carlino et al. stated that more than 300 hydroelectric projects are ref18under consideration across the African continent to meet energy sector needs based on population growth and increased energy demand. They showed that due to the uncertainties related to weather, climate, social, and economic changes, only 40 to 68% of hydroelectric power plants will be economically suitable. They also stated that for reliability against climate change, an increase of 1.8 to 4 percent of investment in this continent is needed [16]. Gurriaran et al. used three climate scenarios, SSP 126, SSP 370, and SSP 585, aiming to determine climate change's impact on energy demand and carbon dioxide emissions in Japan from 2020 to 2100. They stated that the impact of climate change on carbon dioxide emissions from electricity generation has regional and seasonal differences. This study determined that the amount of future electricity demand in most regions of Japan will increase the most in May, June, September, and October [17]. Osman et al. (2023) explored various facets of renewable energy, including production costs, the impacts of climate change, the environment, the economy, and decarbonization efforts. They noted that in certain regions, hydroelectric and wind energy production could decline by as much as 40% due to the effects of climate change. [18]. figure 1 illustrates management and optimal exploitation of water resources systems with the aim of increasing productivity and the ability to meet future needs requires extracting the rules of exploitation of reservoirs and optimal allocation in climate change conditions. Determining and checking the status of a water resources system in a situation where a phenomenon such as climate change affects it increases the reliability of long-term plans and also increases the level of reliability of these systems in providing water to achieve their set goals. The important goals of the dams built in Iran’s Karun, Dez, and Karkheh basins include curbing severe floods, water storage and management, as well as the production of hydroelectric energy. Therefore, this study’s primary goal is to investigate the functioning of Karun Dam 4’s water resources system in the coming periods, the number of changes in the production of the power plant of this complex, and to optimize the amount of production. The progression of the study is outlined below in the flowchart in figure 1.

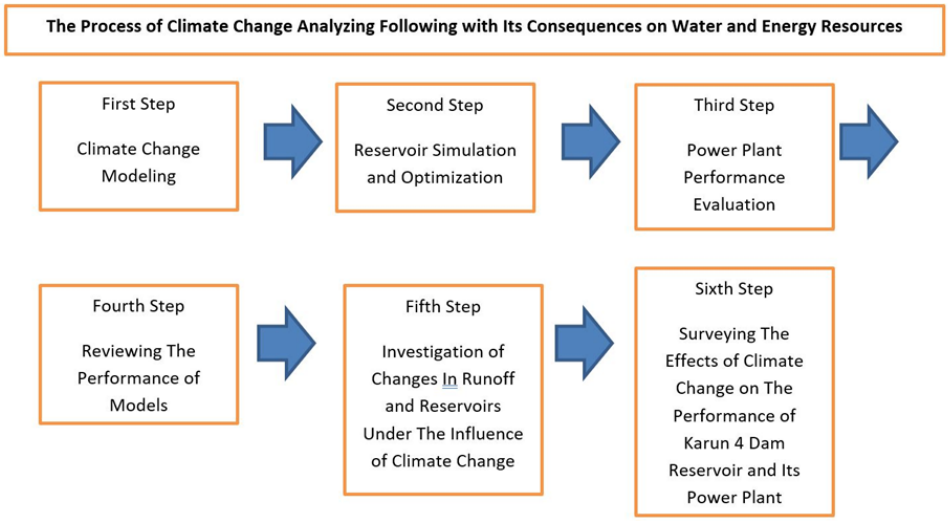


Figure 1. Flowchart of the Research Process

2. Materials and methods

2.1 Study area

Karun Dam 4 is the largest double-arched concrete dam in Iran and the fifth-highest dam in the world. Located in the Chaharmahal and Bakhtiari provinces in southwestern Iran, this dam covers an irrigation basin of approximately 14,500 square kilometers. Constructed with the objectives of regulating the Karun River's annual flow at 3.7 billion cubic meters, flood control, and hydroelectric energy production, the Karun 4 hydropower plant features four turbines, each with a capacity of 255 megawatts. This makes it one of the key hydroelectric power producers in Iran. The dam's strategic location and its significance in energy provision underscore the importance of its management and operation.

The four turbines at the plant each generate 255 MW, with a design height of 161.5 meters, and the plant's nominal output is 1000 MW. Notably, in the model presented, the power plant's load coefficient is treated as a separate variable for each month, typically higher in the warmer months than in the colder ones. Thus, effective management of this coefficient can enhance the balance in energy production and distribution. Table 1 details the characteristics of the studied stations.

Table 1. Characteristics of the Study Stations

No	Station Name	Geographic length	Geographic width	Elevation (meters)
1	Dokouheh	48.15	32.44	**280**
2	BashtAbad	48.24	32.24	**1686**
3	Dezk Abad	48.05	32.49	**2261**
4	Borogen	48.27	48.27	**2245**
5	Morghak	50.50	32.48	**949**
6	Manj	50.63	31.55	**2046**
7	Emam Gheys	51.30	31.75	**2125**
8	Kohrang	50.7	32.26	**2372**
9	Shahre Kord	50.85	32.28	**2057**

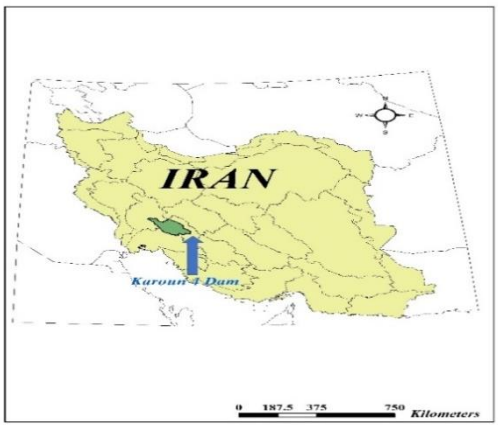


Figure 2. Location of Karun 4 Dam at the Basin Outlet and its Position within Iran

2.2 Research method

This research was conducted in four stages to achieve its objectives:

1- Climate change modeling,
2- Selection of the optimal scenarios,
3- Runoff simulation, and
4- Simulation and optimization of reservoir performance under the influence of climate change.

2.2.1. Climate change modeling

The first step involved downloading daily data from 20 selected models from the fifth report series (CMIP5). Following this, climate change data was processed, and the output of general circulation models (GCMs) was utilized. One critical pre-processing step when using GCMs is skew correction, which involves using observational and recorded regional data and statistical methods, such as fitting statistical functions and correcting potential errors. Table 2 displays the general characteristics of the selected general circulation models, along with their references and development centers.

Given that researchers prioritize achieving results with high accuracy and reliability, reducing the uncertainty in the output of the selected GCMs is essential. To enhance the precision of climate change studies, instead of randomly using all or a portion of the models, only those with better performance are utilized. Preacher and Merkle noted that in recent years, selecting models with superior performance to reduce uncertainty can lead to more dependable results.

Table 2. GCMs Used in this Study

N	Model	N	Model	N	Model	N	Model
1	ACCESS1.0	6	CESM1(BGC)	11	GFDL-ESM2G	16	MIROC-ESM
2	BCC-CSM1.1	7	CNRM-CM5	12	INM-CM4	17	MPI-ESM-MR
3	BNU-ESM	8	CSIRO-Mk3.6.0	13	IPSL-CM5A-LR	18	MPI-ESM-LR
4	CanESM2	9	GFDL-CM3	14	IPSL-CM5A-MR	19	MRI-CGCM3
5	CCSM4	10	GFDL-ESM2M	15	MIROC5	20	NorESM1-M

2.2.2 Selection of the best scenarios

The TOPSIS multi-criteria decision-making methods (further explained in the following section) were used to evaluate the performance of GCMs in this study. Because this approach necessitates selecting and ranking better-performing models, the models should be chosen based on better evaluation indices. Depending on the type of output data used (temperature and precipitation), the following indices have been utilized [19].

The Normalized Root Mean Square Error Index (NRMSE) is one of the most

commonly used indices for evaluating simulated data in various. This index assigns a lower NRMSE value to any model with high accuracy in simulating data and whose values are closer to observational data.

In 2001, Taylor introduced the Taylor Index, one of the best evaluation indices. Due to its high efficiency and accuracy, the Taylor index was used in this study to evaluate the performance of models in estimating observational data during the baseline period. The advantage of the Taylor index over other evaluation indices is that it simultaneously utilizes evaluation criteria, correlation, standard deviation, and the squared differences of model estimation errors. The final Taylor index is calculated to assess the capability and performance of GCMs in simulating climatic variables as follows.

$$S_{Taylor} = \frac{4(1+R)^k}{(\sigma+\frac{1}{\sigma})^2(1+\mathrm{R}_0)^k} \quad (1)$$

R_0 is the maximum value of the correlation coefficient, and if $\sigma \to 1$, then $R \to R_0$, and the Taylor index will reach its maximum value, meaning that the model's performance is completely identical. Conversely, the Taylor index approaches zero when the standard deviation of one model relative to another or observational data is higher. Taylor has suggested that penalty values should be considered for models with low correlation coefficients when simulating climatic variables (precipitation and temperature).

The TOPSIS multi-criteria decision-making method

Introduced by Hwang and Yoon in 1981, this method is among the most widely employed in multi-criteria decision-making. It prioritizes options based on their similarity to the ideal solution. Essentially, in the TOPSIS approach, the best option is the one closest to the ideal answer (efficient), while the worst is furthest from it (inefficient). This method's significant feature is its ability to simultaneously utilize both quantitative and qualitative criteria.

In this study, evaluation metrics were calculated after generating baseline rainfall and temperature data using 20 different climate models. The TOPSIS method was then applied to rank the performance of these climate models, and the top models were selected. Additionally, a composite state of the outputs from general circulation models was used to minimize uncertainty and offer a reliable range of results.

Given the critical importance of the Karun 4 Dam, this study employed RCP scenarios 4.5 and 8.5, representing pessimistic and medium emission levels, respectively. It assessed their impact on the incoming runoff volume to the dam and future hydropower generation. To extract large-scale climate scenarios and simulate variations from the top-performing GCMs identified in the previous stage, specific equations for temperature and precipitation were used to derive the relative differences.

$$\Delta T_i = (\bar{T}_{GCM,fut_i} - \bar{T}_{GCM,base_i}) \quad (2)$$

$$\Delta P_i = (\frac{\bar{P}_{GCM,fut_i}}{\bar{P}_{GCM,base_i}}) \quad (3)$$

In the above equations, ΔPi and ΔTi represent climate change scenario simulations for precipitation and temperature for a long-term average over 21 years in each month; in other words, the 21-year average of simulated precipitation for the future period (2061-2040) and the 21-year average of simulated precipitation for the baseline period (2005-1984) for each month. The same method was applied to temperature. In the previous stage, appropriately performing climate models were selected, and in this stage, using those models, temperature and precipitation data for both RCP 4.5 and RCP 8.5 scenarios were generated and prepared for input into the Lars model. The Lars model estimates the probability distributions governing the data periods, including wet and dry periods, precipitation, temperature (minimum and maximum), and daily radiation from a semi-empirical distribution [20].

2.2.3. Runoff simulation

The IHACRES rainfall-runoff model

Introduced in 1993 by Jakeman and Hornberger, this is a conceptual model for rainfall-runoff processes. This model consists of two main nonlinear modules: the reduction module and the linear hydrograph module. Figure 3 illustrates the general structure of this model. From the figure, it is clear that during the simulation process, precipitation r_k and temperature t_k are first converted to effective rainfall u_k by the nonlinear module at each time step k, and then in the linear section, the unit hydrograph is transformed into surface runoff at time step k.

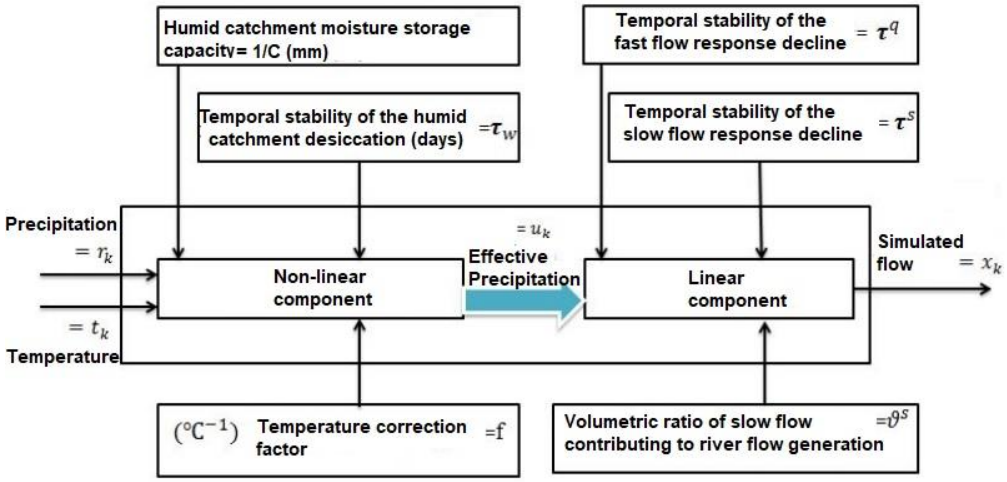


Figure 3. Schematic Representation of the Rainfall-runoff Simulation Process in the IHACRES Model (Sadeghi et al., 2015) [21]

To evaluate the performance of the IHACRES model in simulating the rainfall-runoff process of the Karun 4 dam basin, the model must first be calibrated and then validated. In this study, daily averages of rainfall and temperature data from the basin, along with recorded data from the Dukouheh hydrometric station at the basin outlet, are used to simulate river flow in the basin and assess the model's performance. Various criteria can be used in rainfall-runoff modeling to evaluate model efficiency, but the three most commonly employed criteria used to assess model accuracy are the Root Mean Square Error (RMSE), Mean Absolute Error (MAE), and Nash-Sutcliffe efficiency coefficient. These are further explained in equations 4 to 6.

$$RMSE = \sqrt{\frac{1}{T}\sum_{t=1}^{T}(Q_o^t - Q_m^t)^2} \quad (4)$$

$$MAE = \frac{1}{T}\sum_{t=1}^{T}|Q_o^t - Q_m^t| \quad (5)$$

$$NS = 1 - \frac{\sum_{t=1}^{T}(Q_o^t - Q_m^t)^2}{\sum_{t=1}^{T}(Q_o^t - \overline{Q_o})^2} \quad (6)$$

In the above equations, Q_o^t is the observed flow rate, $Q_m^t$is the estimated flow rate by the model, and t is the time step.

2.2.4. Reservoir Simulation and Optimization

Considering that the goal of this study is to examine the performance of the Karun 4 Dam reservoir in generating hydropower energy under climate change conditions, the performance of the dam's hydropower plant must be simulated and optimized.

After calibrating the precipitation-runoff model using recorded data from the baseline period and generating precipitation and temperature data under various climate scenarios for future periods, the river flow

under different climate scenarios is calculated. However, a simulation of the hydropower production is required to estimate the impact of climate change on hydropower generation from the reservoir. Since the main purpose of the Karun 4 Dam is flood control and hydropower production, the power plant's capacity is determined using the following Equation as a function of water flow (Q) and reservoir water level (H) in a concave nonlinear equation.

$$PPW = f(Q, H) \quad (7)$$

The following objective function was used in this study to examine the effects of climate change on the amount of hydropower generated at the plant due to changes in reservoir inflow.

$$F = Min \sum_{t=1}^{T} \left[1 - \frac{PW_t}{PW_{max}}\right]^2 \quad (8)$$

In this equation, PW represents the production rate, as given by the equation below.

$$PW_t = Min \left[9.81 \times \frac{\gamma \times e \times o_t \times \overline{H_t}}{PF \times 1000}, PW_{max}\right] \quad (9)$$

Next, the average water level is calculated using the following equation.

$$\overline{H_t} = \frac{H_t + H_{t+1}}{2} - TW \quad (10)$$

In the above Equation, PF is the plant efficiency factor, and TW is the tailwater level. The objective function is based on the following continuity equations: overflow volume, evaporation, reservoir volume, and release amount.

$$V_{t+1} = V_t + IN_t - O_t - Spill_t - Ev_t \quad (11)$$

$$Spill_t = \begin{cases} V_{t+1} - V_{max} & V_{t+1} > V \\ 0 & otherwise \end{cases} \quad (12)$$

$$Ev_t = Area_t \times H_t \quad (13)$$

$$V_{\min} \le V_t \le V_{\max} \quad (14)$$

$$O_{\min} \le O_t \le O_{\max} \quad (15)$$

2.2.5. Optimization of the Reservoir Plant's Performance Under Climate Change

This section uses an optimization algorithm to evaluate the objective function of Equation 13 and determine its optimal value. Among various optimization algorithms, the Differential Evolution (DE) algorithm has been used for this study. The Differential Evolution algorithm, introduced by Storn and Price in 1996, is a population-based metaheuristic optimization technique. This algorithm is similar to genetic algorithms in terms of its crossover and mutation operators, but it uses the difference of randomly chosen vectors instead. The DE algorithm consists of three main operators: mutation, crossover, and selection.

Furthermore, the DE algorithm uses a multi-strategy classification approach, denoted as DE/x/y/z, where x, y, and z correspond to the mutation vector and the type of crossover operator (either binomial or exponential).

Power Plant Performance Evaluation

To assess how the reservoir optimally allocates the required water in the baseline and future periods under climate change, two indices—reliability and vulnerability—are used and briefly explained below.

The reliability index is defined based on the probability of meeting the water demand in the simulation period using the available water, and it reflects the plant's ability to generate power at its nominal capacity over the long term [22].

$$R_e = \frac{N_{t=1}^{n}(D_t \le R_t)}{n} \; t = 1,2,\ldots n \quad (16)$$

The vulnerability index is defined as the ratio of demand magnitude during periods of water shortage to the total production and reflects the probability that the plant will

not be able to generate power at its nominal capacity.

$$V_u = \frac{\sum_{t=1}^{n}(D_t - R_t | D_t > R_t)}{\sum_{i=1}^{n} D_t} \quad t = 1,2,\dots n \qquad (17)$$

3. Results and Discussion

3.1 GCM Performance Evaluation

To evaluate and select models of the Karun 4 Dam watershed with better performance in simulating climate variations with higher confidence during the baseline period (1984-2005), daily temperature and precipitation data from various General Circulation Models (GCMs) were compared with observed data averaged using the Thiessen method. The results of this comparison are shown in Table 3 using the NRMSE and S-Tylor indices.

Table 3. Evaluation Index Values for GCMs

		NRMSE		S-Tylor	
	GCM	P	T	P	T
1	GFDL-ESM2M	0.59	0.10	0.45	0.88
2	inmcm4	0.75	0.10	0.39	0.88
3	ACCESS1-0	0.71	0.09	0.43	0.90
4	bcc-csm1-1	0.70	0.09	0.40	0.89
5	BNU-ESM	0.67	0.09	0.39	0.89
6	CSIRO-Mk3-6-0	0.58	0.07	0.48	0.89
7	GFDL-CM3	0.67	0.10	0.37	0.88
8	GFDL-ESM2G	0.69	0.10	0.42	0.88
9	IPSL-CM5A-LR	0.71	0.10	0.28	0.83
10	IPSL-CM5A-MR	0.70	0.10	0.31	0.84
11	MIROC5	0.64	0.09	0.42	0.88
12	CanESM2	0.59	0.08	0.45	0.89
13	CCSM4	0.69	0.10	0.38	0.89
14	CESM1-BGC	0.69	0.09	0.35	0.88
15	CNRM-CM5	0.67	0.09	0.38	0.90
16	MPI-ESM-MR	0.63	0.08	0.42	0.90
17	MRI-CGCM3	0.66	0.14	0.40	0.88
18	NorESM1-M	0.64	0.10	0.42	0.88
19	MIROC-ESM	0.62	0.07	0.44	0.90
20	MPI-ESM-LR	0.75	0.08	0.42	0.89

The evaluation of the performance of GCMs using the TOPSIS method showed that the CSIRO-Mk3-6-0 and CanESM2 FIJ models performed the best in simulating climatic parameters. Based on all criteria, five models, including CSIRO-Mk3-6-0, CanESM2, GFDL-ESM2M, MIROC-ESM, and MPI-ESM-MR, were selected and used in this study. Figures 4 and 5 show the simulated temperature and precipitation changes under both RCP scenarios.

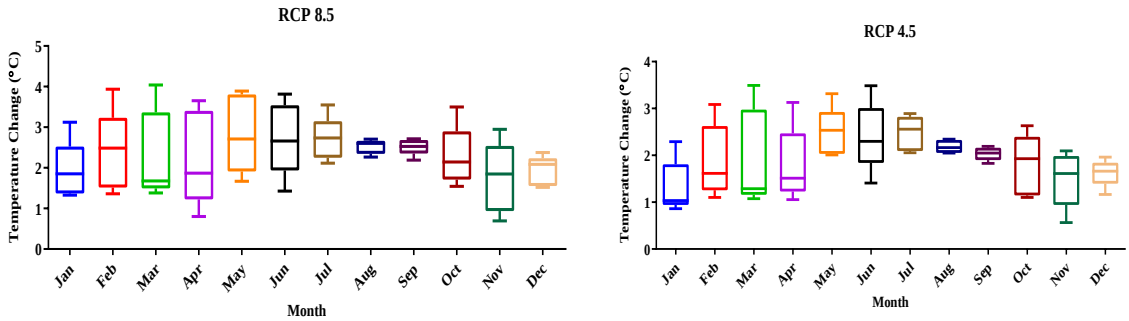


Figure 4. Boxplot Chart of the Average Increase in Expected Temperature using the Selected Five GCMs under RCP 4.5 and RCP 8.5 Scenarios

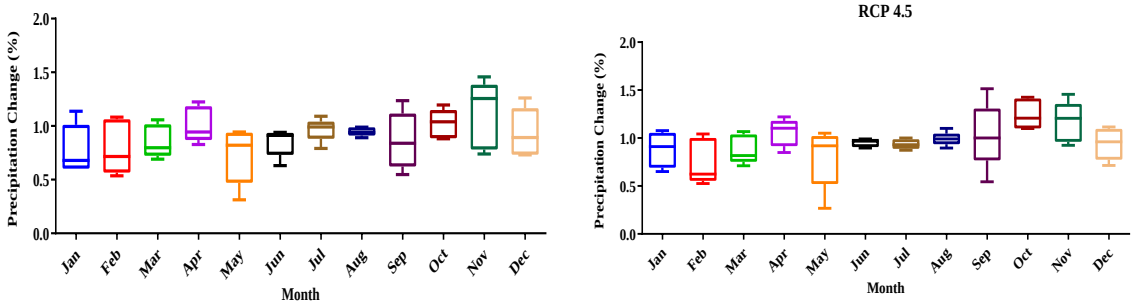


Figure 5. Boxplot Chart of the Average Expected Rainfall Changes using the Selected Five GCMs under RCP 4.5 and RCP 8.5 Scenarios

To reduce the existing uncertainty and increase confidence in the results, each of the five selected GCMs was weighted based on the method described in the previous section. The model whose simulated temperature and precipitation changes were closer to the observed changes during the baseline period at the watershed level was given a higher weight for that month. Based on the results from downscaled climate scenarios generated by the LARS model and the output of the GCMs (Table 4), the expected increase in annual average temperature is 1.95°C under RCP 4.5 and 2.34°C under RCP 8.5 at the Karun 4 Dam watershed. Regarding precipitation, a decrease of 3.52% is expected under RCP 4.5 and a 7.62% decrease under RCP 8.5 at the watershed.

Table 4. Results from Examining Seasonal and Annual Simulated Temperature and Rainfall Changes during the Future Period under Climate Change Influence

Season	Simulated temperature changes (degrees Celsius)		Simulated rainfall changes (percentage)	
	RCP 4.5	RCP 8.5	RCP 4.5	RCP 8.5
Winter	1.99	2.26	1.34	-5.96
Spring	2.25	2.65	-7.5	-13.01
Summer	2.09	2.52	0	0
Fall	1.45	2.02	-6.45	-15.71
Annual	1.95	2.34	-3.52	-7.62

3.2 Results on Changes in Inflow Runoff Volume to the Reservoir Under Climate Change

To understand the changes in inflow runoff volume to the Karun 4 reservoir due to climate change, it is essential to evaluate the precipitation-runoff model's ability to simulate hydrological processes at the watershed level. The IHACRES model was employed for this purpose, with calibration and validation periods chosen to reflect both drought and wet conditions. The calibration period spanned from 1984 to 1998, while the validation period covered 1999 to 2005. The model demonstrated satisfactory performance in estimating the monthly runoff volume for the Karun 4 watershed, as illustrated in Figure 6.

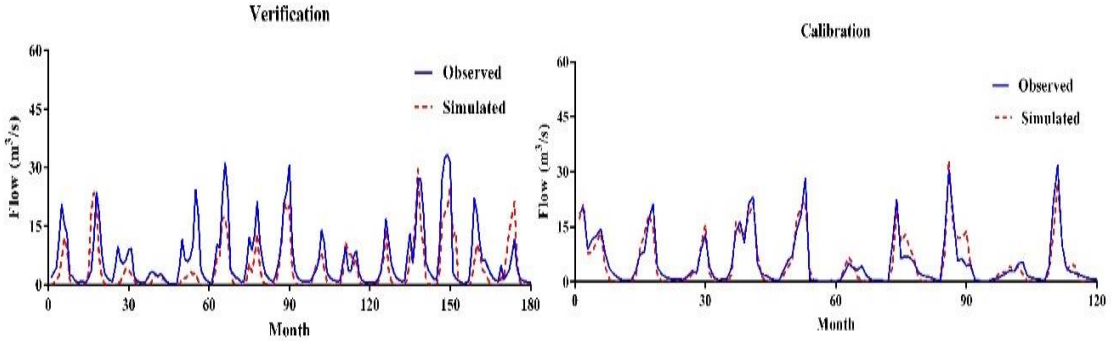


Figure 6. Evaluation of the IHACRES Model Performance in Simulating the Rainfall-runoff Process

The R2 value in the calibration period was 0.75 with RMSE = 80; in the validation period, R2 was 0.78 with RMSE = 40.

After confirming that IHACRES accurately simulates the precipitation-runoff process, the next step is to assess how changes in temperature and precipitation will impact the runoff volume entering the Karun-4 reservoir in the future, which is crucial for evaluating turbine performance. The simulated time series data of temperature and precipitation were used to model the runoff from the upper catchment of Karun-4 Dam. Considering the previous findings, which indicate an increase in temperature and a decrease in precipitation, it is predicted that the runoff volume entering the reservoir will decrease in the future compared to the baseline period. As illustrated in Figure 7, the total runoff volume is expected to decline under both scenarios. The projections indicate a 28% reduction in runoff volume under the RCP 4.5 scenario and a 43% reduction under the RCP 8.5 scenario.

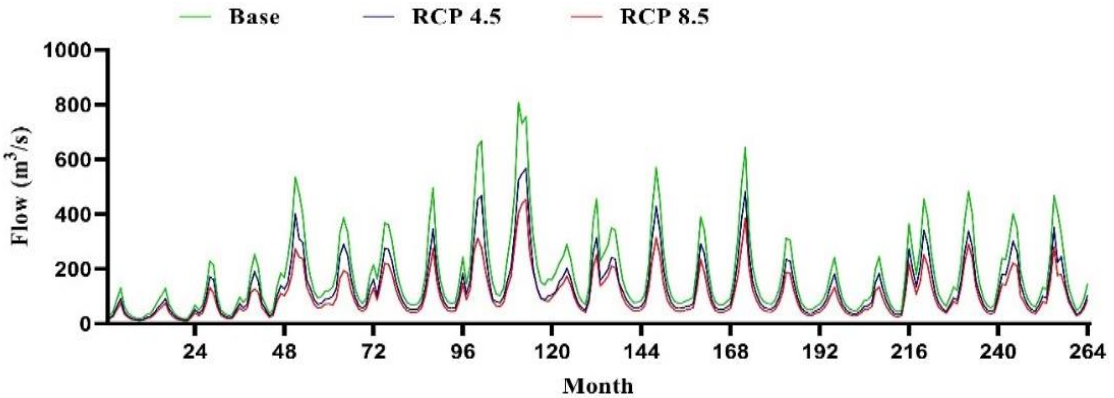


Figure.7 Comparison of the Baseline and Future Periods' Monthly Average Runoff Volume Entering the Reservoir under the Influence of Climate Change

Based on these results, the reduction in the volume of runoff entering the reservoir (outflow from the catchment) due to the increase in temperature and the decrease in precipitation will impact the performance of the reservoir as well as hydroelectric power generation in the future period.

3.3 Results of the Study on the Effects of Climate Change on the Performance of the Karun-4 Dam Reservoir and Hydroelectric Power Plant in Energy Production

After reviewing the long-term average changes in key climatic parameters (temperature and precipitation) at the catchment scale, as well as the volume of runoff entering the Karun-4 Dam reservoir—considered the most significant factor influencing the performance and amount of hydroelectric power production—the simulation of hydroelectric energy production has been conducted based on the results presented in the previous sections. Table 5 provides the specifications of the Karun-4 Dam turbine.

Table 5. Karun 4 Dam Power Plant Specifications

Specification	Number/Unit	Specification	Number/Unit
Turbine	4	Number and type of generators	4 synchronous generators
Turbine power	255 megawatts	Output power of each generator	263 megavolt-amperes
Nominal discharge	95.7	Nominal voltage of each generator	15.75 kilovolts
Design head	161.5 meters	Generator rotation speed	187.5 revolutions per minute
Nominal water outlet from turbine	171 cubic meters per second	Nominal generator current	12,500 amperes
Transformer	12 primary units / 1 reserve	Primary nominal voltage	15.75 kilovolts
Nominal power of each transformer	100 megavolt-amperes	Secondary nominal transformer voltage	410 kilovolts

Based on the results presented in Table 6 and the previous sections' findings, hydroelectric energy production is expected to decrease by 9% compared to the baseline under the RCP 4.5 scenario in the future period. Considering the assumptions of the RCP 8.5 scenario and the results from its application in the previous sections, the total reduction in power production at the Karun-4 Dam power plant in the future period is predicted to be 18%. Accordingly, the system's reliability is expected to decrease by 30% under the RCP 4.5 scenario and by 56% under the RCP 8.5 scenario in the future period compared to the baseline period. The table below presents the energy production, as well as the system reliability and vulnerability values for the Karun-4 Dam power plant in both the baseline and future periods under the stated climate change conditions. Figure 8 shows the monthly changes in electricity production under baseline conditions and considering climate change scenarios.

Table 6. Comparison of Electricity Production and Evaluation Criteria for the Karun 4Dam Turbine System during the Baseline and Future Periods under Climate Change Influence

	SumPower	Reliability	Vulnerability
Base	220549.53	49.62	0.16
RCP 4.5	200659.21	34.47	0.23
RCP 8.5	179049.60	21.59	0.32

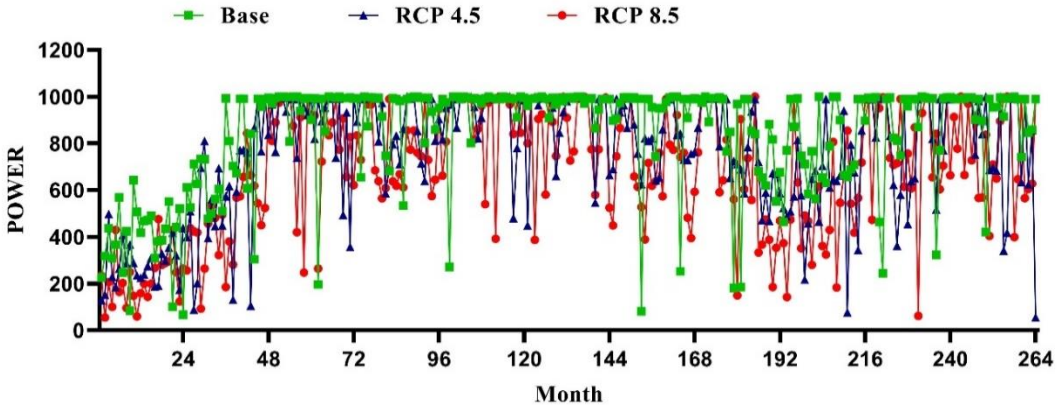


Figure 8. Comparison of the Total Average Monthly Energy Production during the Baseline and Future Periods under Climate Change Influence

4. Conclusion and Recommendation

Based on the results of this study, it is expected that, there will be an increase in temperature and a decrease in precipitation in the upstream catchment of Karun-4 in the future periods compared to the baseline period. Specifically, the annual average temperature is projected to increase by 1.95°C under the RCP 4.5 scenario and 2.34°C under the RCP 8.5 scenario. Additionally, annual precipitation is expected to decrease by 3.52% under the RCP 4.5 scenario and 7.62% under the RCP 8.5 scenario in the Karun-4 catchment area.

According to the results of this study, the volume of runoff exiting the catchment and entering the reservoirs, influenced by the effects of climate change on temperature and precipitation (two key factors affecting the precipitation-runoff process), is expected to decrease by an average of 19% under the RCP 4.5 scenario and by 43% under the RCP 8.5 scenario.

Given these results, assuming such a decrease in the average runoff volume entering the Karun-4 reservoir, the performance of this strategic reservoir will face significant challenges. It is certain that, in addition to the reduced reliability of the system's performance at the Karun-4 Dam, there will be an increase in the vulnerability of the dam's power plant in the future periods. The findings of this study indicate that the reduction in the volume of runoff entering the reservoir and changes in the seasonality of runoff can impact the operation and management of the reservoir and should be carefully considered by the operators.

Given this power plant's significance and strategic position in supplying a portion of the country's electricity, the reduction in total electricity production from the Karun-4 power plant is another important study result. Specifically, a reduction in the power plant's energy production of approximately 9% under the RCP 4.5 scenario and about 18% under the RCP 8.5 scenario should not be unexpected.

Additionally, it is suggested that in future studies, more detailed flowcharts are presented to show the correlation between parameters and climate changes so that deeper analyses can be achieved. The authors finish their paper on a positive note by talking about the benefits of their work and possible future work. With this limited study, it is not known whether this finding can be applied to all clinical scenarios. Notwithstanding these limitations, this study has proven that Ultrasound can potentially serve as a more efficient alternative to X-rays in diagnosis. Future directions include studying the effects of different ultrasound pulsing schemes on pain relief. Another interesting direction would be to consider applications in nonhuman primates.

References

1. Panwar, N. L., Siva Reddy, V., Ranjan, K. R., Seepana, M. M., & Totlani, P. (2013). Sustainable development with renewable energy resources: a review. World Review of Science, Technology and Sustainable Development, 10(4), 163-184.
2. Suman, A. (2021). Role of renewable energy technologies in climate change adaptation and mitigation: A brief review from Nepal. Renewable and Sustainable Energy Reviews, 151, 111524.
3. Panwar, N. L., Kaushik, S. C., & Kothari, S. (2011). Role of renewable energy sources in environmental protection: A review. Renewable and Sustainable Energy Reviews, 15(3), 1513-1524.
4. Sims, R. E. (2004). Renewable energy: a response to climate change. Solar energy, 76(1-3), 9-17.
5. Kapica, J., Canales, F. A., & Jurasz, J. (2021). Global atlas of solar and wind resources temporal complementarity. Energy Conversion and Management, 246, 114692.
6. Therán Nieto, K. R., & Rodríguez Potes, L. (2018). Hábitat sostenible. Adaptación y mitigación frente al cambio climático. Hacia los territorios resilientes. Módulo Arquitectura CUC, 21(1), 63-96.
7. Zhao, X., Huang, G., Li, Y., & Lu, C. (2023). Responses of hydroelectricity generation to streamflow drought under climate change. Renewable and Sustainable Energy Reviews, 174, 113141.
8. Shan-e-hyder Soomro, A. Soomro, S. Batool, Jiali Guo, Yinghai Li, Yanqin Bai, Caihong Hu, Muhammad Tayyab, Zhiqiang Zeng, Ao Li, Yao Zhen, Kang Rui (2024). How does the climate change effect on hydropower potential, freshwater fisheries, and hydrological response of snow on water availability. Applied Water Science, 14(65),64-96.
9. Denholm, P., Brinkman, G., & Mai, T. (2018). How low can you go? The importance of quantifying minimum generation levels for renewable integration. Energy Policy, 115, 249-257.
10. Zapata, V., Gernaat, D. E., Yalew, S. G., da Silva, S. R. S., Iyer, G., Hejazi, M., & Van Vuuren, D. P. (2022). Climate change impacts on the energy system: a model comparison. Environmental Research Letters, 17(3), 034036.
11. Zolghadr-Asli, B., Bozorg-Haddad, O., & Chu, X. (2019). Effects of the uncertainties of climate change on the performance of hydropower systems. Journal of Water and Climate Change, 10(3), 591-609.
12. Beheshti, M., Heidari, A., & Saghafian, B. (2019). Susceptibility of hydropower generation to climate change: Karun III Dam case study. Water, 11(5), 1025.
13. Bhatt, U. S., Carreras, B. A., Barredo, J. M. R., Newman, D. E., Collet, P., & Gomila, D. (2022). The potential impact of climate change on the efficiency and reliability of solar, hydro, and wind energy sources. Land, 11(8), 1275.
14. Craig, M. T., Wohland, J., Stoop, L. P., Kies, A., Pickering, B., Bloomfield, H. C., Browell, J., De Felice, M., Dent, C. J., & Deroubaix, A. (2022). Overcoming the disconnect between energy system and climate modeling. Joule, 6(7), 1405-1417.
15. Mirani, K. B., Ayele, M. A., Lohani, T. K., & Ukumo, T. Y. (2022). Evaluation of hydropower generation and reservoir operation under climate change from Kesem Reservoir, Ethiopia. Advances in Meteorology, 2022(1), 3336257.
16. Carlino, A., Wildemeersch, M., Chawanda, C. J., Giuliani, M., Sterl, S., Thiery, W., Van Griensven, A., & Castelletti, A. (2023). Declining cost of renewables and climate change curb the need for African hydropower expansion. Science, 381(6658), eadf5848.
17. Gurriaran, L., Tanaka, K., Takahashi, K., & Ciais, P. (2023). How climate change may shift power demand in Japan: Insights from data-driven analysis. Journal of Environmental Management, 345, 118799.
18. Osman, A. I., Chen, L., Yang, M., Msigwa, G., Farghali, M., Fawzy, S., Rooney, D. W., & Yap, P.-S. (2023). Cost, environmental impact, and resilience of renewable energy under a changing climate: a review. Environmental chemistry letters, 21(2), 741-764.
19. Preacher, K. J., & Merkle, E. C. (2012). The problem of model selection uncertainty in structural equation modeling. Psychological methods, 17(1), 1.

20. Semenov, M. A., Barrow, E. M., & Lars-Wg, A. (2002). A stochastic weather generator for use in climate impact studies. User Man Herts UK, 1-27.
21. Sadeghi, Siddhadi, Ghasemiah, Nejad, S., & Javad, S. (2015). Assessment of the Hydrological Model IHACRES' Performance in Humid Regions: A Case Study of the Noorud Basin, Gilan. Water and Soil Science (Isfahan University of Technology), 19(73), 73-83.
22. Hashimoto, T., Stedinger, J. R., & Loucks, D. P. (1982). Reliability, resiliency, and vulnerability criteria for water resource system performance evaluation. Water resources research, 18(1), 14-20.

© 2025 by the authors. Licensee SCU, Ahvaz, Iran. This article is an open access article distributed under the terms and conditions of the Creative Commons Attribution 4.0 International (CC BY 4.0 license) (http://creativecommons.org/licenses/by/4.0/).

Application of Intelligent Models in Investigating the Energy Dissipation in Labyrinth Weirs with Various Cycles Form

Hamidreza Abbaszadeh [*,1], Reza Tarinejad [1], John Abraham [2]

1. Faculty of Civil Engineering, University of Tabriz, Tabriz, Iran.
2. School of Engineering, University of St. Thomas, St. Paul, MN 33901, USA

***Corresponding Author:**
Hamidreza Abbaszadeh

Email: ha.abbaszadeh@tabrizu.ac.ir
Received: 2024.11.14
Accepted: 2025.02.21
J. Hydraul. Struct., 2025; 11(4):16-32
DOI: 10.22055/jhs.2025.48309.1329

ABSTRACT

Weirs play a crucial role as hydraulic structures in the regulation and control of water flow. This study investigates the relative energy dissipation in labyrinth weirs, examining various configurations, scales, and cycle types, using advanced computational models like Support Vector Machine (SVM), Random Forest (RF), and Artificial Neural Network (ANN). In SVM modelling, the results from different kernel functions reveal that the Radial Basis Function (RBF) kernel outperforms polynomial, linear, and sigmoid kernels in predicting relative energy dissipation. For the RBF kernel, the statistical metrics were found to be (R=0.907), (Mean RE%=1.38), (RMSE=0.0153), and (KGE=0.744) in test phase. where RE, Mean RE, RMSE and KGE represent the Relative Error, Mean Relative Error, Root Mean Square Error and Kling Gupta Efficiency, respectively. In contrast, in the ANN model, the multilayer perceptron (MLP) network showed higher accuracy than the RBF network, achieving 0.969, 0.73%, 0.007, and 0.968 for the same indicators. For the RF model, these values were recorded as 0.878, 1.78%, 0.0192, and 0.362, respectively. Comparative analysis indicates that the ANN model offers superior predictive performance over SVM and RF models. Additionally, non-linear polynomial regression equations, derived from dimensionless parameters, are proposed for estimating relative energy dissipation. Notably, single-cycle weirs exhibited the greatest energy dissipation among the configurations studied.

KEYWORDS

Energy dissipation, Labyrinth weirs, Soft computing, Weir cycle.

1. Introduction

When discussing flow control structures, weirs represent one of the most significant types. Weirs commonly used for measuring flow, regulating flow levels, and controlling the flow of irrigation and drainage channels. Labyrinth weirs are used in increase efficiency. The amount of flowing passes over the weirs during the flood peak is significant, so the presence of a weir with a high water discharge coefficient is necessary. The ability of a weir to transmit water depends upon the crest length and upstream head. Consequently, by making changes to the geometry (increasing the crest length) in a constant channel width, the carrying capacity increases. For this purpose, labyrinth weirs are more practical than linear weirs, which flow through them more than linear weirs. Today, nonlinear weirs like triangular, trapezoidal, oblique, and parabolic are built in one or more cycles.

Another characteristic of weirs is their ability to dissipate flow energy. The ability to predict this effect enables designers to more accurately calculate changes to flow energy in the system and thus properly design downstream slabs. Most research on labyrinth weirs has focused on their discharge coefficients. However, there is a significant gap in the study of energy loss associated with these types of weirs, highlighting the need for further research and modeling. Additionally, the application of intelligent models to predict energy loss has received limited attention. Energy dissipation is a critical factor in the design of hydraulic structures, especially in weirs, as it directly impacts the downstream flow conditions and the potential for scour or structural damage. In the context of weir design, the primary goal is to ensure that the energy of the flowing water is effectively dissipated to prevent damage to the structure and minimize erosive forces downstream. In weir structures, energy dissipation occurs when the flow transitions from high-velocity supercritical conditions to subcritical conditions, often as a result of flow obstructions such as the weir crest. The amount of energy dissipated is a function of various parameters, including the geometry of the weir, the flow depth, and the velocity of the water. In labyrinth weirs, which are characterized by their non-linear geometry and multi-cycle designs, the energy dissipation process is significantly more complex than in traditional straight-crested weirs.

Hay and Tylor [1] did the first studies on labyrinth weirs. They provided diagrams for the weir design. Tullis et al. [2] investigated trapezoidal plan labyrinth weirs with 6 to 18 apex angles. They described the discharge coefficient (C_d) and its dependence on parameters such as the upstream water level, weir height weir length, and apex angle. Kumar et al. [3] indicated that C_d decreases and length of the interference zone increases as the weir apex angle decreases. Monjezi et al. [4] conducted research on the C_d of arched weirs with a triangular plan form. They concluded that arching weirs increases the efficiency of linear arched weirs and labyrinth arched weirs by up to 21% and 57%, respectivly. Azimi and Hakim [5] studied the rectangular labyrinth weir and showed its suitability for the $h_0/P<0.4$ (h_0 is the head, and P is the weir height). Ayaz and Mansoor [6] analyzed the C_d of labyrinth weirs using ANN model. The results indicated that the ANN successfully predicted the discharge coefficient. The results of Samadi et al. [7] showed that increasing the number of cycles in labyrinth weirs reduces the C_d. Ben Said and Ouamane [8] conducted an experimental and numerical study of rectangular labyrinth weirs. Their results indicated that there is a good agreement between the experimental and numerical results. Also, a weir with a round inlet increases the weir efficiency by 5% compared to a smooth inlet. Zare et al. [9] studied a circular labyrinth weir with various slopes. Their results showed that the highest C_d is for a slope of 60° and the lowest for a state without a slope. Shehata et al. [10] conducted a laboratory study of labyrinth trapezoidal weirs in flow and scour control. Their study indicated that a 60° apex angle provided better results in reducing scour depth and length compared to other angles and a straight weir.

The flow energy dissipation has been investigated in stepped spillways, ogee weirs, chutes, etc. [11-14]. Mohammadzadeh-Habili et al. [15] checked relative energy dissipation (EDR) in labyrinth weirs, resulting that EDR decreases linearly with increasing y_c. Ghaderi et al. [16] conducted a numerical analysis of the C_d and EDR in labyrinth weirs, revealing that C_d values range from 0.4 to 0.8, while EDR varies between 0.6 and 0.3. Furthermore, labyrinth weir structures dissipate between 85% and 70% of flow energy for dimensionless ratios of $1 \geq h_0/P \geq 0.1$ [17]. Furthermore, the research of Idrees and Al-Ameri [18] showed that trapezoidal configurations increase energy

dissipation rates by over 92%. Selim et al. [19] conducted a numerical study of piano key and trapezoidal labyrinth weirs. Their results showed that the energy loss of trapezoidal labyrinth weirs increases with increasing side wall angle. Piano key weirs are preferred over labyrinth trapezoidal weirs at lower ratios ($h_0/P \leq 0.2$), while trapezoidal labyrinth weirs with smaller angles are recommended at higher weir ratios.

While prior studies (e.g., Tullis et al. [2], Kumar et al. [3], Monjezi et al. [4]) have extensively explored discharge coefficients (C_d) in labyrinth weirs, they often overlook the critical aspect of energy dissipation. Only a few studies, such as Haghiabi et al. [17], specifically address EDR, and even these are limited to specific weir configurations and flow conditions. Most prior research relies on empirical equations or experimental analysis for modeling hydraulic performance. Although these approaches provide valuable insights, they lack the generalizability and predictive accuracy required for diverse real-world applications. Existing studies primarily focus on a narrow range of weir geometries (e.g., trapezoidal and triangular forms). However, the influence of different cycle types and configurations on energy dissipation has not been systematically evaluated. For instance, research by Selim et al. [19] and Idrees and Al-Ameri [18] briefly mentions geometric impacts but lacks detailed modeling of their effects on EDR.

Several key hydraulic phenomena contribute to energy dissipation in labyrinth weirs:

Flow Contraction and Expansion: As water approaches the labyrinth weir, it is first subjected to flow contraction, which increases the flow velocity. Upon crossing the weir crest, the flow expands rapidly. These sudden changes in flow direction and velocity lead to the formation of turbulent zones, which are the primary contributors to energy loss.

Flow Separation and Reattachment: The unique geometry of labyrinth weirs, such as the triangular or trapezoidal cycle shapes, induces flow separation at the crest of each cycle. As the flow separates, vortexes and turbulent eddies are generated. These vortices and their subsequent reattachment downstream create localized energy dissipation zones, enhancing the overall energy loss in the system. This phenomenon is particularly prominent in multi-cycle labyrinth weirs.

Hydraulic Jump: For larger flow discharges, the flow may become supercritical (high velocity) as it flows over the crest of the weir. When this supercritical flow transitions to subcritical flow downstream, a hydraulic jump is formed. During the hydraulic jump, a significant portion of the flow's kinetic energy is converted into turbulent energy, resulting in substantial energy dissipation. In labyrinth weirs, the multiple cycles often promote the formation of such jumps at various locations, further increasing the energy dissipation.

Turbulent Flow in Weir Cycles: In labyrinth weirs, the multi-cycle design creates a series of bends and turns for the flow. These changes in direction cause the flow to become turbulent, with vortices and eddies dissipating kinetic energy. The turbulence is particularly strong in the regions between the weir cycles, where the flow interacts with the weir surface and the channel bed.

Cavitation and Flow Impingement: In some cases, the flow may impinge on the weir surface, generating localized areas of high shear stress and turbulence. This can lead to the formation of cavitation bubbles, which contribute to further energy loss. Although cavitation is not always a significant factor in labyrinth weirs, it can become relevant under high flow conditions.

The discussion of these hydraulic phenomena lays the foundation for understanding the energy dissipation process in labyrinth weirs. By considering these phenomena, we can better appreciate how the geometry and flow characteristics of a labyrinth weir influence the efficiency

of energy dissipation. This understanding provides the necessary context for exploring advanced computational models, such as those based on machine learning, to predict energy dissipation more accurately. The complexity of the flow and energy dissipation process in labyrinth weirs, therefore, necessitates the development of robust predictive models that account for the dynamic and non-linear nature of these systems.

A considerable number of previous studies have focused on investigating the flow rate of labyrinth weirs. The research on the labyrinth weir's energy dissipation has been done in a limited way, and except for a few researches, it has not been carried out yet widely. Given the inherent uncertainties surrounding energy dissipation modeling in previous studies, further investigation into intelligent modeling approaches for energy dissipation in labyrinth weirs with varying plan forms appears essential. Accordingly, this study focuses on analyzing the energy dissipation in labyrinth weirs with triangular and trapezoidal configurations across various cycle types. Using experimental data, the performance of intelligent modeling techniques-including ANN, SVM, and RF algorithm−has been evaluated in predicting energy dissipation.

2. Materials and Methods

Here, the data of Haghiabi et al. [17] have been used. Triangular and trapezoidal plan labyrinth weirs with single and double cycles were used. The EDR in the labyrinth weir is calculated according to Equation (1) [15,17].

$$E_0 = y_0 + \frac{q^2}{2gy_0^2}$$
$$E_1 = y_1 + \frac{q^2}{2gy_1^2} \quad (1)$$
$$EDR = \frac{\Delta E}{E_0} = \frac{E_0 - E_1}{E_0}$$

In the above equations, E_0 and E_1 represent the specific energy of the flow (L), y_0 and y_1 represent the flow depth (L), q is the flow rate per unit width of the channel (L^2T^{-1}), g is the gravitational acceleration (LT^{-2}), and ΔE is the energy dissipation (L).

According to Haghiabi et al. [17] and Equation (2), the most significant parameters affecting EDR are:

$$EDR = f_1(W_c, W_{cy}, L_{cy}, L_{cr}, P, V_0, h_0, g, \rho) \quad (2)$$

In Equation (2), h_0 represents the flow depth above the weir (L), V_0 is the velocity (LT^{-1}), g is the gravitational acceleration (LT^{-2}), P represents the weir height (L), ρ is the specific gravity of water (ML^{-3}), W_c is the channel width (L), W_{cy} is the width of one weir cycle (L), L_{cy} is the length of one weir cycle (L), L_{cr} total length of the crest (L). According to Haghiabi et al. [17] and Buckingham theorem as dimensional analysis technique and by considering the V_0, g and ρ as repetitive parameter, the non-dimensional parameters are derived as Equation (3). Since the flow upstream of the weir is subcritical, the effect of the Froude number can be ignored. The Reynolds number can also be neglected due to the turbulence of the flow. Figure (1) indicates the picture of the triangular and trapezoidal plan labyrinth weir.

$$EDR = f_2\left(\frac{h_0}{P}, \frac{W_c}{W_{cy}}, \frac{L_{cy}}{W_{cy}}\right) \quad (3)$$

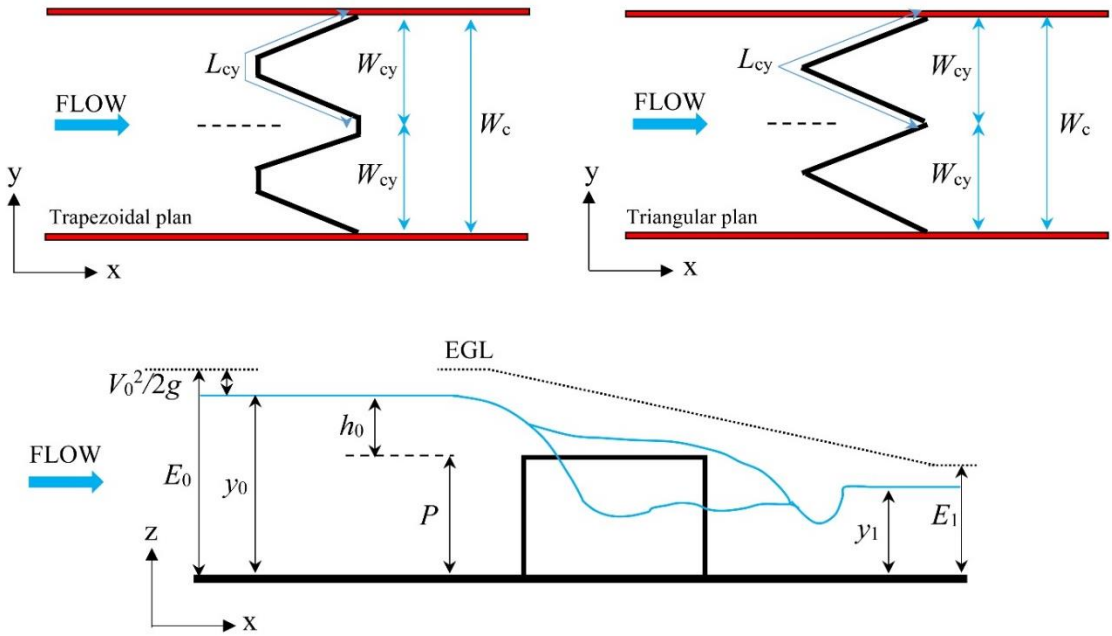


Figure 1. View of the labyrinth weir [17]

2.1. Support Vector Machine (SVM)

SVM is a supervised learning model widely applied for both classification and prediction tasks [20]. The algorithm employs constrained optimization to minimize structural penalty, thereby achieving an optimal response. It functions by estimating a model that associates the dependent variable with several independent input parameters [21,22]. The function can be written as Equation (4):

$$f(x) = \sum_{i=1}^{N} \bar{a}_i \emptyset(X_i)^T \emptyset(X) + b \qquad (4)$$

The a_i represents the mean Lagrange coefficients. Calculating ø(X) can be very complicated. The SVM regression uses a kernel function that depends on the size of the training data and the dimensions of the feature vector. In practice, four types of Lin. kernel, Poly. kernel, Sig. kernel, and Radial Basis Function kernel (RBF) are used.

$$K(X_i, X_j) = (X_i, X_j) \qquad (5)$$

$$K(X_i, X_j) = \left(1 + (X_i, X_j)\right)^d \qquad (6)$$

$$K(X_i, X_j) = tanh\left(-a(X_i, X_j) + C\right) \qquad (7)$$

$$K(X_i, X_j) = exp(-\|X - X_i\|^2/\sigma^2) \qquad (8)$$

2.2. Artificial Neural Network (ANN)

ANN comprises input layers, hidden layers, and output layers that collectively facilitate decision-making processes. Within this structure, neurons serve as fundamental units that transform input signals before transmitting processed information to subsequent layers. The architecture of the network consists of interconnected mathematical operations, often nonlinear, that enable complex interactions across layers, resulting in sophisticated and nonlinear behaviors. Although each neuron functions independently, the network as a whole demonstrates cohesive behavior. While ANNs share certain similarities with human neural activity, there are notable differences in terms of training processes, operational behavior, and computational capacity [23].

2.3. Random Forest algorithm (RF)

RF is a supervised learning model that typically leverages the bagging method, which combines multiple learning models to enhance overall performance. In RF, multiple decision trees are constructed and

merged, resulting in superior predictive accuracy [24]. Random forests are applicable to both classification and regression tasks. During the training or model-fitting phase, the RF model maps input data to outputs by learning from data relevant to the target problem domain. Through this process, the model identifies and learns underlying relationships within the data to accurately predict the desired output values [25].

2.4. Statistical indicators

Here, the following statistical indicators were employed [26-28]:

$$RE\% = \frac{X_{Obs} - X_{cal}}{X_{Obs}} \times 100 \quad (9)$$

$$RMSE = \sqrt{\frac{\sum_{i=1}^{n}(X_{Obs} - X_{Cal})_i^2}{n}} \quad (10)$$

$$KGE = 1 - \sqrt{(R-1)^2 + (\beta-1)^2 + (\gamma-1)^2}$$
$$\beta = \frac{\overline{X_{Cal}}}{\overline{X_{Obs}}}, \gamma = \frac{CV_{Cal}}{CV_{Obs}}$$
$$R = \frac{[\sum_{i=1}^{n}(X_{Obs\,i} - \overline{X_{Obs}}) \times (X_{Cal\,i} - \overline{X_{Cal}})]}{\sum_{i=1}^{n}(X_{Obs\,i} - \overline{X_{Obs}}) \sum_{i=1}^{n}(X_{Cal\,i} - \overline{X_{Cal}})} \quad (11)$$

Here, Equation (9 to11) represent the percentage relative error, root mean square error, and King Gupta Efficiency, respectively. Also, in Equation (12), R, β and γ represent the coefficient of correlation, ratio of the mean cal to the mean obs and ratio of the standard deviation of cal to the standard deviation of the observed, respectively.

3. Results and Discussion

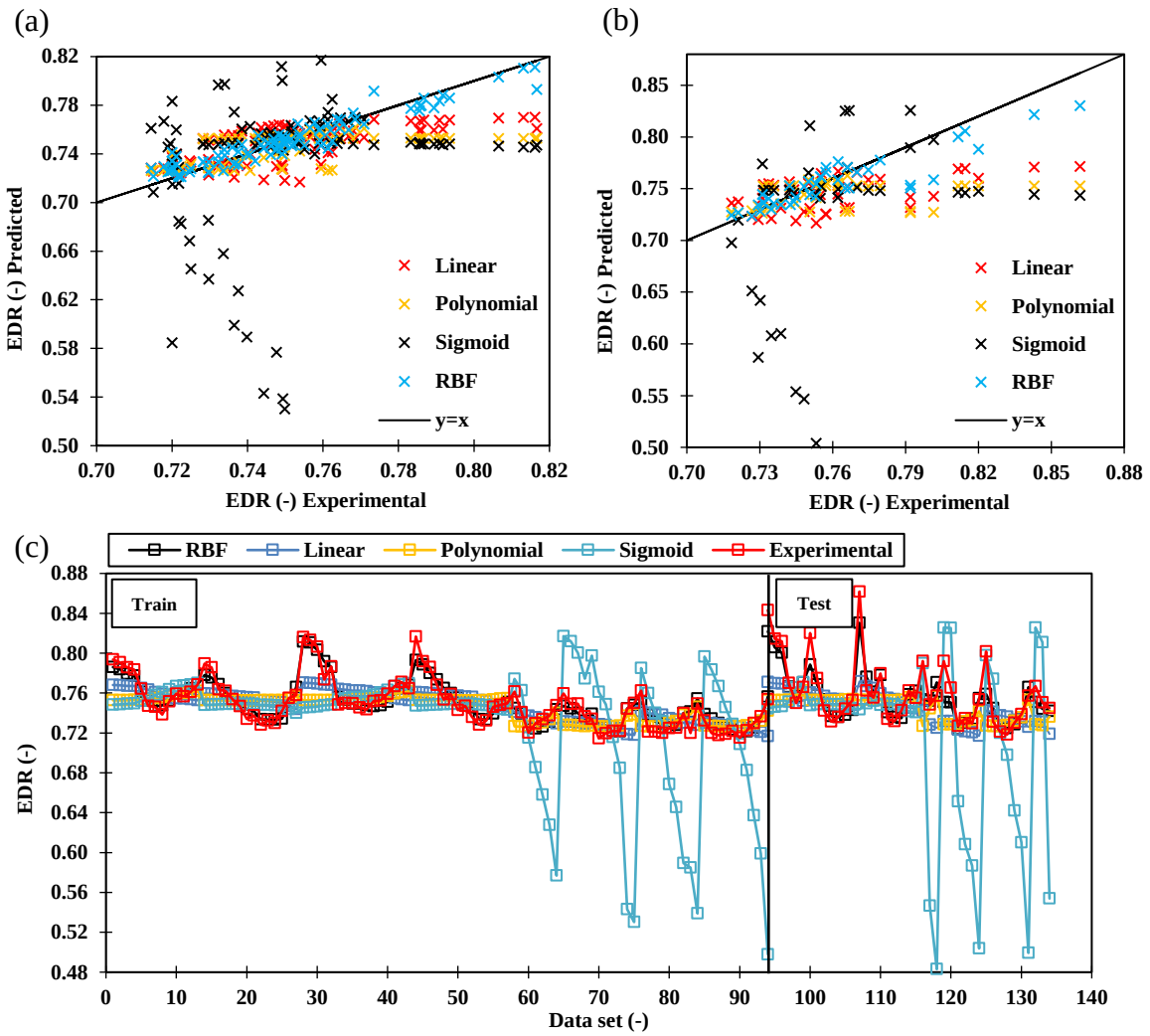
The objective was to assess the applicability of modern data mining techniques for estimating EDR. A dataset comprising 70% of the data was allocated for the training phase, and the remaining 30% for testing.

As indicated in Table (1), among the Lin., Poly., RBF, and Sig. kernels, the RBF was identified as the optimal choice for the SVM. The comparison among obs and cal values of EDR is illustrated in Figures (2a and b) for various kernels. Additionally, various data sets are depicted in Figure (2c). The RBF demonstrated significantly higher accuracy compared to the other kernels, effectively predicting EDR with notable precision.

Figures (2d and e) present the statistical performance indicators for the RBF during the training phase, with values of 0.952, 0.0076, 0.0078 and 0.865 for R, RMSE, Mean RE, and KGE, respectively. For the testing phase, the corresponding values were 0.907, 0.0153, 0.0138, and 0.744, respectively. Figures (2f and g) further illustrate that the superior kernel maintains a wide range of data points within the $\pm$3% RE band. Specifically, in the training phase, 100% of the data points fall within this error band, while 96% of the data points in the testing phase also fall within the same margin.

Table 1. The results of the test statistical indices of various kernels in the SVM

Indicators	Lin.	Poly.	RBF	Sig.
Coefficient of correlation	0.530	0.239	0.907	0.292
Kling Gupta Efficiency	0.308	0.007	0.744	-0.912
Root Mean Square Error	0.0319	0.0359	0.0153	0.0992
Mean Relative Error %	3.150	2.937	1.38	8.564



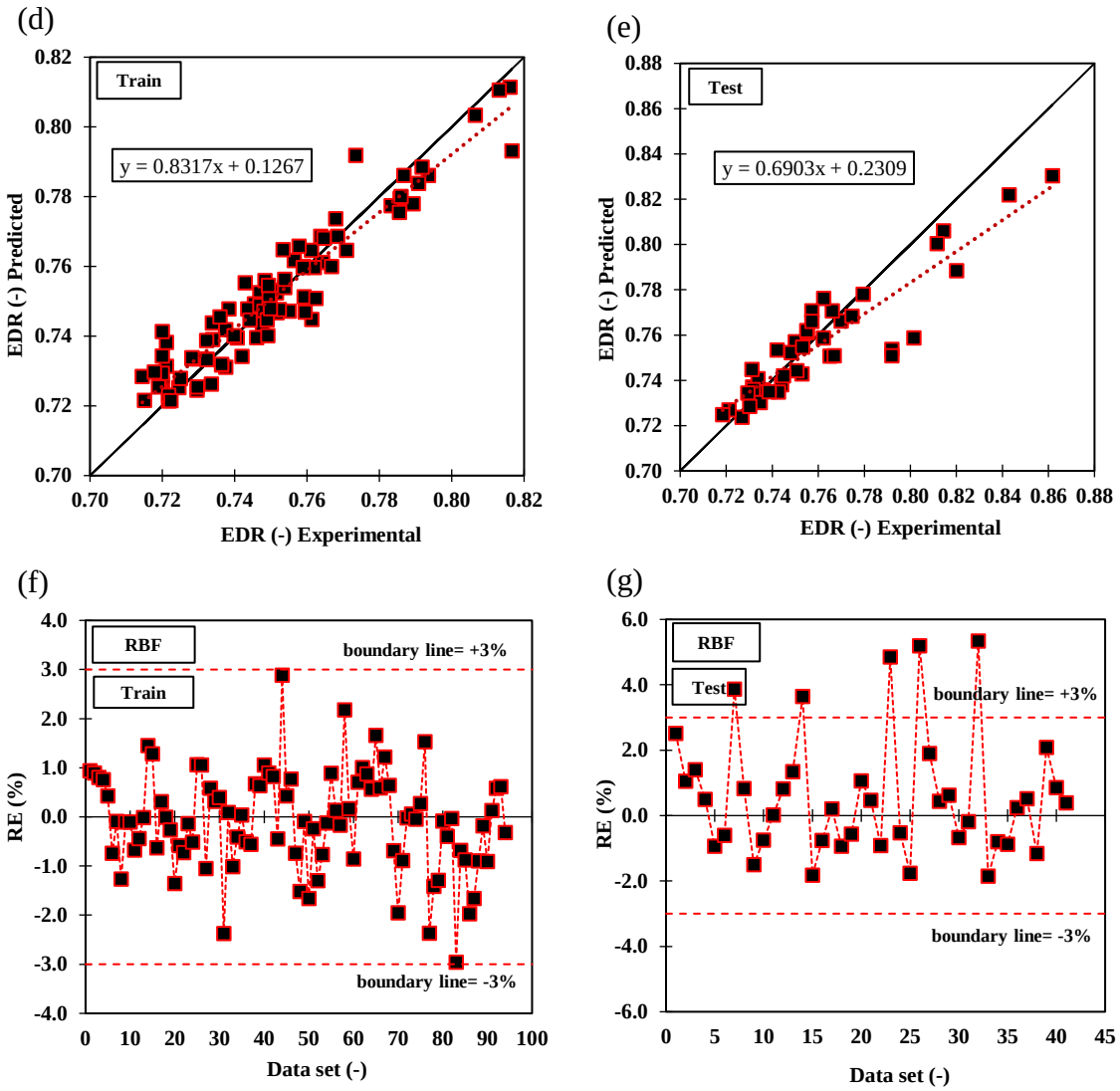


Figure 2. Experimental versus predicted values

In the ANN method, similar to the SVM model, 70% of the data were randomly allocated for training, while the remaining 30% were designated for testing, facilitated by the software. As depicted in Figure (3), the accuracy of the multilayer perceptron (MLP) network improved in comparison to the radial basis function (RBF) network. For the MLP network, the performance metrics of R, RMSE, Mean RE and KGE were 0.972, 0.0064, 0.64%, and 0.958, respectively (training phase). In the testing phase, the statistical metrics were 0.969, 0.0070, 0.73%, and 0.968, respectively.

In contrast, the RBF network yielded training phase results of 0.871, 0.0134, 1.16% and 0.815 for R, RMSE, Mean RE and KGE, respectively. During the testing phase, the corresponding values were 0.943, 0.103, 1.04% and 0.941, respectively. In the test phase, the MLP and RBF networks exhibited data within the ±2.80% and ± 10.3% RE ranges, respectively. Consequently, based on these results, the MLP method was identified as the superior model at this stage.

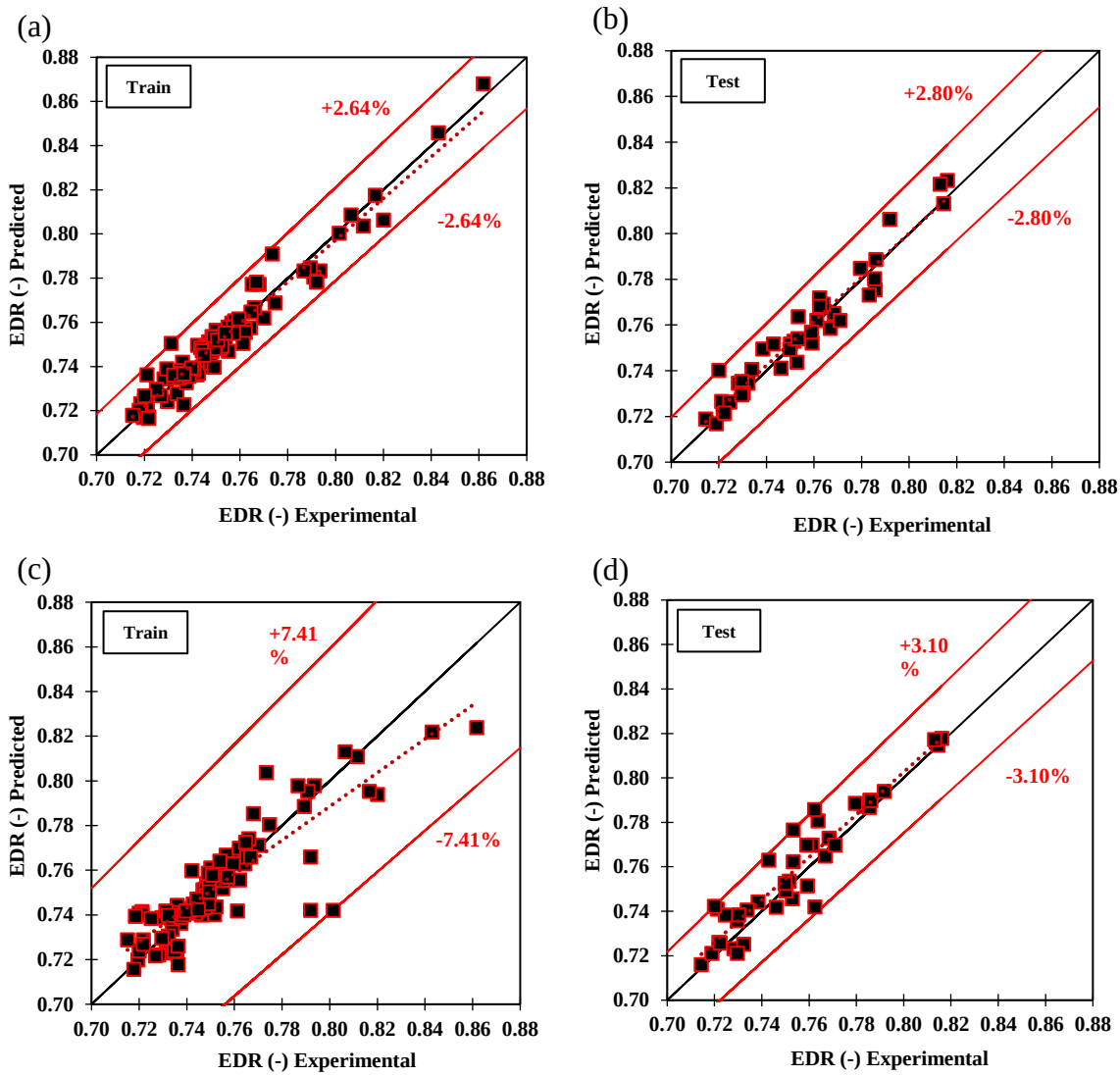


Figure 3. Experimental values versus predicted, a and b) MLP, c and d) RBF

Figures (4a and c) show the scatter diagram of the data in the training and test phase for the RF model. Here, R=0.878, RMSE=0.0188, Mean RE%=1.78% and KGE=0.362 for the training phase. For the test stage, it is equal to 0.898, 0.0193, 1.91%, and 0.369, respectively. Although the value of the Mean RE in the RF model in the training and test phase are 1.78% and 1.91%, respectively, it is not possible to make a decision based on the result of this index. The reason for these values can be pointed to close observed data so that the EDR is in the range of 0.714 to 0.862. Therefore, these results are not good. The KGE for this model is less than 0.4 and it is in the unsatisfactory part, which indicates the lack of proper ability of this model in predicting the amount of EDR. Figures (4b and d) show the overlap of the experimental and predicted data for different data in the training and test phase, which are significantly different from each other. The detailed discussion of the potential reasons of low statistical indexes are as follows:

1. Sensitivity to Data Characteristics: The RF model aggregates predictions from multiple decision trees, which makes it robust to noise but less capable of

capturing subtle nonlinear interactions in data. Since energy dissipation in labyrinth weirs involves complex, nonlinear relationships between hydraulic and geometric parameters, RF may have struggled to adequately capture these complexities.

2. Limited Variability in Experimental Data: The experimental dataset used in this study, while well-structured, covers a relatively narrow range of flow conditions and geometric configurations. This limited variability can reduce the effectiveness of RF, as its ensemble approach relies on diverse data splits to construct highly predictive trees.
3. KGE's Sensitivity to Model Bias: The low KGE observed for the RF model may stem from its tendency to underestimate or overestimate specific ranges of energy dissipation. Since KGE accounts for correlation, bias, and variability, even small biases in RF predictions can lead to a lower overall score compared to metrics like RMSE or mean relative error (RE%).
4. Overfitting to Training Data: Although RF generally reduces overfitting compared to individual decision trees, it can still overfit if the number of trees is too high or the maximum depth of trees is not restricted. Overfitting could have reduced the model's ability to generalize to the testing dataset, thereby affecting its performance.

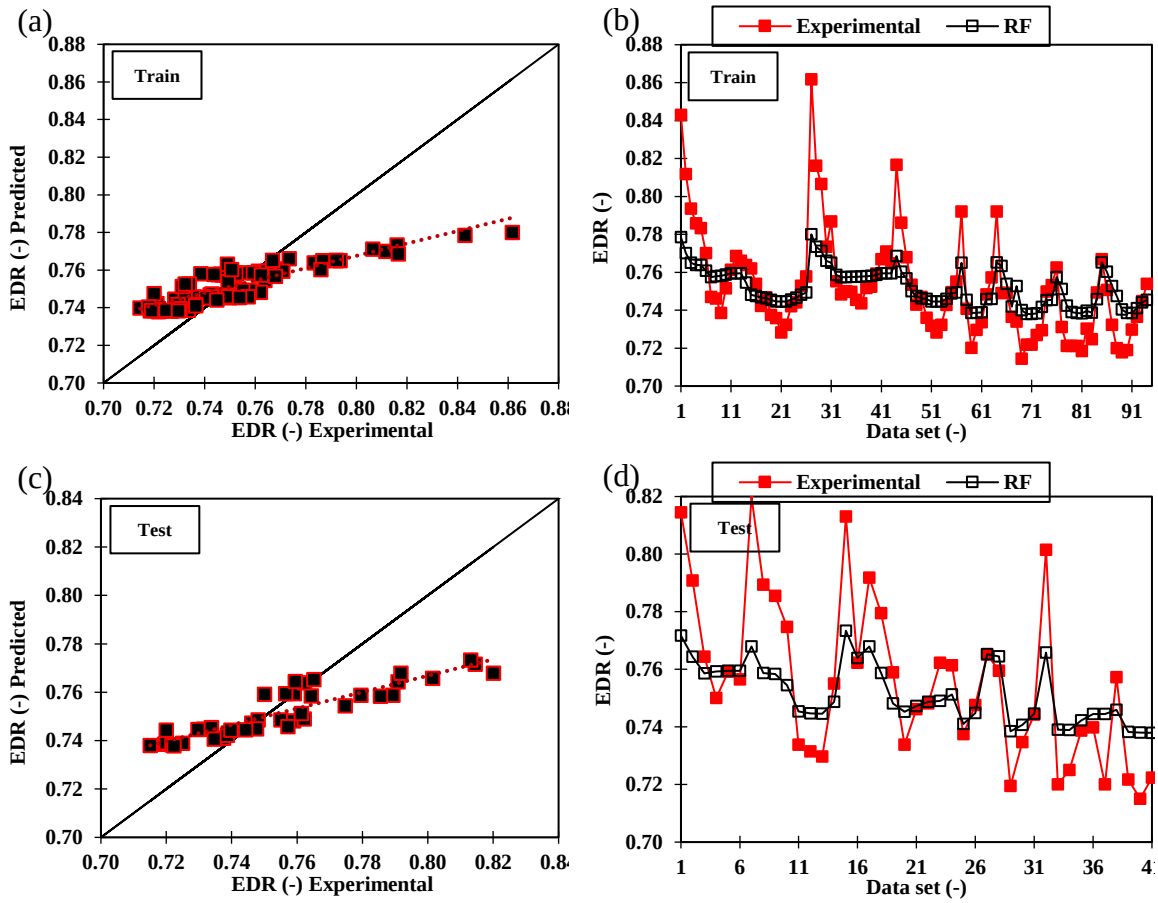


Figure 4. Experimental values versus predicted in RF model

Figure (5) presents the optimal outcomes for each model group−SVM, ANN, and RF −to determine the most effective approach for predicting EDR. As illustrated in Figure (5a), the RF model's predictions fall within a RE range of ±9.36%, with an RMSE and Mean RE% of 0.0193 and 1.91%, respectively. In contrast, the SVM model using the RBF kernel demonstrated improved accuracy over the RF model, yielding data within a RE range of ±5.34% and achieving an RMSE of 0.0153 and a Mean RE% of 1.38%. Among the models, the ANN-MLP method exhibited the most accurate performance, with results closely aligned with experimental data. For the ANN-MLP model, predictions fell within a ±2.80% RE range, with RMSE and Mean RE% values of 0.0070 and 0.73%, respectively. The correlation coefficients for the RF, SVM-RBF, and ANN-MLP models in the test phase were 0.898, 0.907, and 0.969, respectively. A comparative analysis of EDR predictions and experimental data indicates a superior alignment of ANN model outputs with experimental results, as shown in Figure (5b). The superior performance of the ANN can be attributed to several key factors, which are discussed below:

1- Ability to Capture Nonlinear Relationships: The ANN, specifically the Multilayer Perceptron (MLP) architecture used in this study, is inherently well-suited for modeling complex and nonlinear relationships in datasets. Energy dissipation in labyrinth weirs is influenced by multiple interacting parameters, such as flow depth, weir height, and cycle geometry, which exhibit nonlinear dependencies. The ANN's capability to model these interactions more effectively than the SVM and RF algorithms likely contributed to its superior predictive accuracy.

2- Data Characteristics: The dataset used in this study comprises well-structured experimental data with consistent trends and relationships, which ANN models can leverage effectively. The network's ability to adjust weights and biases during training allows it to identify and exploit patterns in the data that may not be as easily captured by other models.

3- Flexible Model Architecture: The architecture of the MLP used in this study, with multiple hidden layers and nonlinear activation functions, provides greater flexibility in learning intricate relationships between input and output variables. This flexibility may explain why the ANN outperformed SVM, which relies on kernel functions, and RF, which aggregates multiple decision trees but may not handle complex nonlinearities as efficiently.

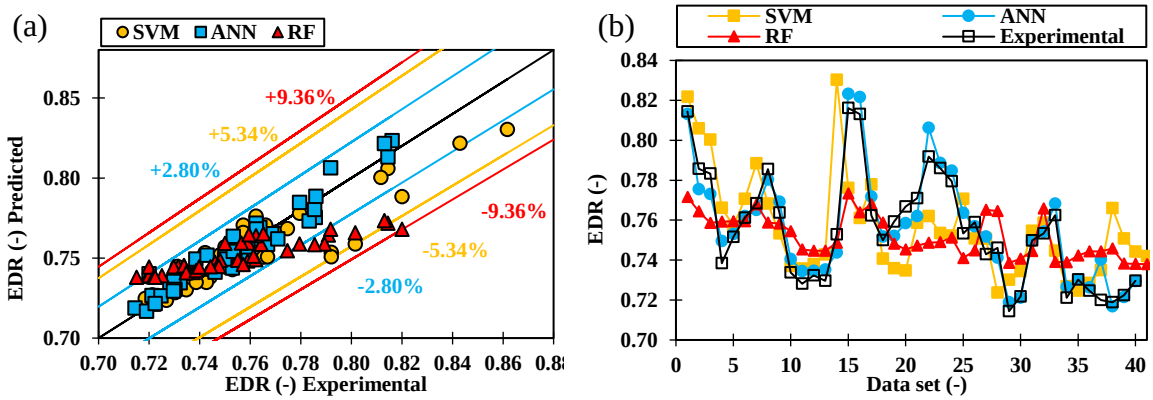


Figure 5. Experimental values versus predicted for different models in the test phase

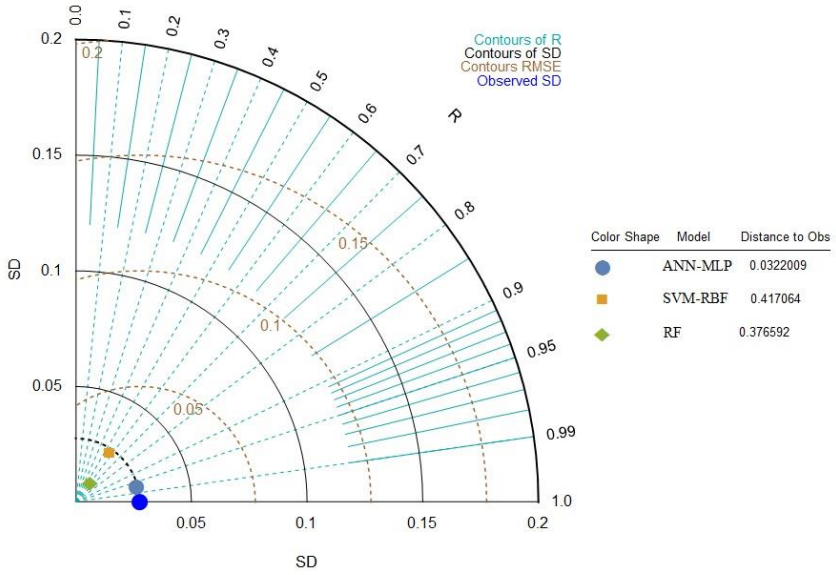


Figure 6. Taylor diagram

The Taylor diagram confirms that the ANN-MLP model significantly outperforms the SVM-RBF and RF models in predicting the EDR for labyrinth weirs (Figure 6). Its high correlation coefficient, low RMSE, and accurate standard deviation matching make it the most robust and reliable model [27]. These findings highlight the ANN model's The high EDR of labyrinth weirs can be attributed to the following main processes:

1. The collision of the flow near the upstream vortices and between the triangular and trapezoidal weir cycles. According to the research of Crookston and Tullis [29] and Mohammadzadeh-Habili et al. [15], the flow impinging on the weir creates a local hydraulic jump condition near the upstream vortices, which leads to energy dissipation.
2. The turbulent flow creates a pool in front of the weir. In a labyrinth weir, the return flow caused by the impact of the flow falling with the channel bed leads to the formation of an eddy flow in the pool behind the flow jet (in front of the weir). The pool flow energy is dissipated through turbulent eddies.
3. Supercritical flow collides at the channel base and a hydraulic jump is formed downstream of the weir. During the hydraulic jump, a significant part of the energy is lost. As the discharge increases, the performance of labyrinth weirs decreases. The main reason for this is that the flow fills the space among the weir cycles. By increasing the discharge, the opportunity to drain the flow from the space among the cycles is lost. The highest value of EDR is related to single-cycle weirs. As L_{cy}/W_{cy} increases, the flow energy dissipation decreases. At $h_0/P \geq 0.5$, this amount goes through the same process. In addition, the reason why the trapezoidal plan weir inferior to triangular plan weir for energy dissipation. This observation is related to the reduction of head dissipation due to the sudden change of the inlet and outlet streamlines [17].

potential as a powerful tool for hydraulic engineering applications, particularly in modeling energy dissipation in complex flow systems. This analysis strengthens the conclusion that ANN is the preferred model for accurate and reliable predictions, making it a valuable contribution to the design and optimization of labyrinth weirs.

In this research, by using Solver in Excel software, relationships have been presented to predict the amount of energy dissipation of labyrinth weirs with triangular and trapezoidal plans, respectively, within the scope of this research:

$$EDR = -5.10\left(\frac{h_0}{p}\right)^{0.004} + 1.30\left(\frac{L_{cy}}{W_{cy}}\right)^{-0.044} + 4.58\left(\frac{W_c}{W_{cy}}\right)^{0.0045} \quad (12)$$

$$EDR = -1.72\left(\frac{h_0}{p}\right)^{0.012} + 0.094\left(\frac{L_{cy}}{W_{cy}}\right)^{-0.825} + 2.418\left(\frac{W_c}{W_{cy}}\right)^{0.004} \quad (13)$$

The results of Mean RE% for the above relationships are 1.86% and 2.12%, respectively. The amount of RMSE are 0.017, and 0.019, respectively. For the relationships, KGE is in the very good range. The results showed that the above relationships have high accuracy in predicting energy dissipation, so for the above relationships, more than 82% and 83% of the data are within the RE range of ±3%, respectively.

The comparison of the statistical metrics for derived equations with those from the previous studies shows the following:

Table 2. The results of the present study with previous studies

Study	RMSE (-)	Mean RE (%)	KGE (-)
Equation (12)	0.017	1.86	0.96
Equation (13)	0.019	2.12	0.94
Mohammadzadeh-Habili et al. [15]	0.021	2.02	0.91
Haghiabi et al. [17]	0.023	2.14	0.89

The derived equations for predicting EDR in labyrinth weirs show superior performance when compared to previous studies. The statistical results, including RMSE, Mean RE%, and KGE, confirm the enhanced accuracy and robustness of these models. The new equations are more reliable and applicable to a wider range of weir configurations, making them a valuable tool for predicting energy dissipation in labyrinth weir design and analysis.

To strengthen the analysis of the derived equations and their relevance to hydraulic principles, we have incorporated a discussion that relates the empirical formulas for energy dissipation rate with established hydraulic concepts. This analysis aims to validate the theoretical underpinnings of the equations and demonstrate their physical relevance in the context of labyrinth weirs.

Hydraulic Evidence for EDR Equations

Energy dissipation in weir structures, particularly labyrinth weirs, is primarily governed by the following hydraulic phenomena:

1. Flow Contraction and Expansion: As water flows over the labyrinth weir, it undergoes contraction at the entrance and expansion at the outlet. These transitions induce turbulence, which is a significant factor contributing to energy loss.

2. Flow Separation and Reattachment: The non-linear geometry of labyrinth weirs, with their multi-cycle configuration, causes complex flow patterns. Flow separation near the weir's crest and the subsequent reattachment downstream creates vortices, which enhance the energy dissipation.

3. Hydraulic Jump: In cases of high discharge, supercritical flow on the weir face may transform into subcritical flow downstream, forming a hydraulic jump. This phenomenon is a major contributor to energy dissipation.

4. Turbulent Flow in the Weir Cycles: The multiple cycles of a labyrinth weir create additional surfaces where water can interact with the channel bed, inducing turbulent flow that contributes to energy loss. This is particularly evident in the formation of eddies and vortices in front of and behind the weir cycles.

The derived equations for EDR incorporate these hydraulic principles through their dependence on key geometrical and flow parameters, such as:
$\boldsymbol{h_0}$: The flow depth above the weir, which influences the potential energy available for dissipation.
$\boldsymbol{P}$: The weir height, which directly affects the flow velocity and, thus, the kinetic energy dissipated.
$\boldsymbol{W_c}$ and $\boldsymbol{W_{cy}}$: These parameters describe the width of the channel and the weir cycles, which control the flow interactions and turbulence intensity.
$\boldsymbol{L_{cy}}$: The length of one weir cycle, which impacts the flow path and the degree of energy dissipation through the turbulence and vortices.

Physical Interpretation of Derived Equations

We can now analyze the physical behavior predicted by the derived equations using hydraulic principles:
The Equations indicate a strong dependence on h_0, P, and W_{cy}. These findings align with established hydraulic theory, where the flow depth (h_0) and weir height (P) are key drivers of flow velocity and energy conversion, respectively.
The presence of W_{cy} and L_{cy} in the equations is consistent with the idea that the geometry of the weir affects the flow dynamics. Wider and longer weir cycles (W_{cy} and L_{cy}) tend to induce more complex flow patterns, including turbulence and vortices, which enhance energy dissipation.
The lower Mean Relative Error (RE%) and Root Mean Square Error (RMSE) values observed for the derived equations suggest that these parameters are effectively capturing the physical processes of energy dissipation. This is consistent with the hydraulic understanding that energy loss is most prominent where flow separation, turbulence, and hydraulic jumps occur, particularly in non-linear weir geometries like those in labyrinth weirs.
By analyzing the derived equations through the lens of hydraulic principles, we demonstrate that the empirical formulas for predicting EDR are not only statistically robust but also consistent with established hydraulic theory. The dependence of the equations on flow depth, weir height, and cycle geometry supports their physical relevance and underscores their ability to model the complex flow phenomena involved in energy dissipation in labyrinth weirs.

4. Conclusions

In this study, data mining techniques−support vector machine (SVM), artificial neural network (ANN), and random forest (RF)−were employed to predict energy dissipation in labyrinth weirs. The primary objective was to assess the predictive accuracy of these methods and identify the most effective approach for modeling this complex hydraulic phenomenon. Each model utilized a dataset split, with 70% of the data allocated for training and 30% for testing. The results revealed several significant findings, limitations, and opportunities for further research, which are detailed below.

Key Findings:

Support Vector Machine (SVM):
The SVM model's performance was critically analyzed using various kernel functions, including polynomial, linear, sigmoid, and radial basis function (RBF). Among these, the RBF kernel demonstrated superior predictive accuracy. The performance metrics for the SVM-RBF model in the testing phase included a coefficient of determination (R) of 0.907, a root mean square error (RMSE) of 0.0153, a mean relative error percentage (Mean RE%) of 1.38%, and a Kling-Gupta efficiency (KGE) of 0.744. These metrics underscore the RBF kernel's ability to closely align with experimental results, making it a robust choice for this application.
Artificial Neural Network (ANN):
The ANN approach explored two types of networks: multilayer perceptron (MLP) and radial basis function (RBF). The MLP

network outperformed the RBF network in terms of predictive accuracy. By leveraging its capacity to model complex non-linear relationships, the MLP network emerged as the most effective among all models tested in this study. This finding highlights the potential of ANN, particularly the MLP structure, in modeling energy dissipation phenomena with high precision.

Random Forest (RF):

While the RF model exhibited acceptable predictive capabilities, its performance was inferior compared to the SVM-RBF and ANN-MLP models. This result aligns with the understanding that ensemble-based models like RF, while robust, may not capture the intricate non-linear relationships in hydraulic systems as effectively as ANN and SVM models.

Non-Linear Polynomial Regression Equations:

In addition to data mining models, non-linear polynomial regression equations were developed to enhance predictive modeling. These equations provided supplementary insights into the relationship between the input variables and energy dissipation, offering a simpler yet less accurate alternative compared to the machine learning models.

Limitations:

Dataset Size and Diversity:

The dataset used in this study was limited in size and scope, which may impact the generalizability of the findings. Future studies should consider larger and more diverse datasets to validate the robustness of the models across different conditions and geometries.

Unconsidered Variables:

The study focused on a specific set of input variables to predict energy dissipation. However, other potentially influential factors, such as flow turbulence characteristics and material properties, were not included. Incorporating these factors in future models could enhance predictive accuracy.

Model Complexity:

While the ANN and SVM models demonstrated high accuracy, their computational complexity might limit their practical application in scenarios requiring real-time predictions. Simplifying these models without compromising accuracy could improve their utility in field applications.

Recommendations for Future Research:

Building upon the findings and limitations of this study, several recommendations for future research are proposed:

Dataset Expansion:

Future studies should prioritize collecting and incorporating larger, more diverse datasets from different labyrinth weir configurations, flow conditions, and experimental setups. This will ensure broader applicability of the models and enhance their generalizability.

Exploration of Advanced Techniques:

While this study focused on SVM, ANN, and RF models, emerging machine learning techniques, such as deep learning, gradient boosting algorithms, and hybrid models, could be explored. These methods may offer improved performance and new insights into the predictive modeling of energy dissipation.

In summary, this study demonstrates the potential of data mining techniques, particularly SVM and ANN, in accurately predicting energy dissipation in labyrinth weirs. Among the models tested, the ANN-MLP model emerged as the most effective, followed closely by the SVM-RBF model. These findings contribute to the growing body of knowledge on the application of machine learning in hydraulic engineering, offering new avenues for optimizing the design and performance of hydraulic structures.

References

1. Hay, N., & Taylor, G. (1970). Performance and design of labyrinth weirs. Journal of the Hydraulics Division, 96(11), 2337-2357.
2. Tullis, B. P., Young, J. C., & Chandler, M. A. (2007). Head-discharge relationships for submerged labyrinth weirs. Journal of hydraulic engineering, 133(3), 248-254.
3. Kumar, S., Ahmad, Z., & Mansoor, T. (2011). A new approach to improve the discharging capacity of sharp-crested triangular plan form weirs. Flow measurement and instrumentation, 22(3), 175-180.
4. Monjezi, R., Heidarnejad, M., Masjedi, A., Purmohammadi, M. H., & Kamanbedast, A. (2018). Laboratory investigation of the Discharge Coefficient of flow in arced labyrinth weirs with triangular plans. Flow Measurement and Instrumentation, 64, 64-70.
5. Azimi, A. H., & Hakim, S. S. (2019). Hydraulics of flow over rectangular labyrinth weirs. Irrigation Science, 37(2), 183-193.
6. Ayaz, M., & Mansoor, T. (2021). Development of ANN model for discharge prediction and optimal design of sharp-crested triangular plan form weir for maximum discharge using linked ANN–optimization model. Water Supply, 21(6), 3027-3041.
7. Samadi, A., Salmasi, F., Arvanaghi, H., & Mousaviraad, M. (2022). Effects of geometrical parameters on labyrinth weir hydraulics. Journal of Irrigation and Drainage Engineering, 148(10), 06022006.
8. Ben Said, M., & Ouamane, A. (2022). Performance of rectangular labyrinth weir–an experimental and numerical study. Water Supply, 22(4), 3628-3644.
9. Zare, H., Vaghefi, M., Mahmoudi, A., & Behroozi, A. M. (2023). Experimental exploration of flow hydraulics and discharge coefficient for an inclined circular labyrinth weir. Water Resources Management, 37(11), 4521-4536.
10. Shehata, A. H., Youssef, T. F., Hamada, H. A., & Samy, A. (2024). Optimizing Trapezoidal Labyrinth Weir Design for Enhanced Scour Mitigation in Straight Channels. Water, 16(17), 2443.
11. Parsaie, A., & Haghiabi, A. H. (2019). The hydraulic investigation of circular crested stepped spillway. Flow Measurement and Instrumentation, 70, 101624.
12. Zhou, Y., Wu, J., Ma, F., & Qian, S. (2021). Experimental investigation of the hydraulic performance of a hydraulic-jump-stepped spillway. KSCE Journal of Civil Engineering, 25, 3758-3765.
13. Biabani, R., Salmasi, F., Nouri, M., & Abraham, J. (2022). Flow over embankment gabion weirs in free flow conditions. Journal of Hydro-Environment Research, 44, 65-76.
14. Salmasi, F., & Abraham, J. (2023). Hydraulic characteristics of flow over stepped and chute spillways (case study: Zirdan Dam). Water Supply, 23(2), 851-866.
15. Mohammadzadeh-Habili, J., Heidarpour, M., & Samiee, S. (2018). Study of energy dissipation and downstream flow regime of labyrinth weirs. Iranian Journal of Science and Technology, Transactions of Civil Engineering, 42, 111-119.
16. Ghaderi, A., Daneshfaraz, R., Dasineh, M., & Di Francesco, S. (2020). Energy dissipation and hydraulics of flow over trapezoidal–triangular labyrinth weirs. Water 12 (7): 1992.
17. Haghiabi, A. H., Nou, M. R. G., & Parsaie, A. (2022). The energy dissipation of flow over the labyrinth weirs. Alexandria Engineering Journal, 61(5), 3729-3733.
18. Idrees, A. K., & Al-Ameri, R. (2023). Investigation of flow characteristics and energy dissipation over new shape of the trapezoidal labyrinth weirs. Flow Measurement and Instrumentation, 89, 102276.
19. Selim, T., Hamed, A. K., Elkiki, M., & Eltarabily, M. G. (2024). Numerical

investigation of flow characteristics and energy dissipation over piano key and trapezoidal labyrinth weirs under free-flow conditions. Modeling Earth Systems and Environment, 10(1), 1253-1272.
20. Vapnik VN (1995) The nature of statistical learning theory. Springer-Verlag, New York
21. Daneshfaraz, R., Santos, C. A. G., Norouzi, R., Kashani, M. H., AmirRahmani, M., & Band, S. S. (2023). Prediction of drop relative energy dissipation based on Harris Hawks Optimization algorithm. Iranian Journal Of Science And Technology, Transactions Of Civil Engineering, 47(2), 1197-1210.
22. Norouzi, R., Sihag, P., Daneshfaraz, R., Abraham, J., & Hasannia, V. (2021). Predicting relative energy dissipation for vertical drops equipped with a horizontal screen using soft computing techniques. Water Supply, 21(8), 4493-4513.
23. Al-Bulushi, N. I., King, P. R., Blunt, M. J., & Kraaijveld, M. (2012). Artificial neural networks workflow and its application in the petroleum industry. Neural Computing and Applications, 21, 409-421.
24. Sun, D., Lonbani, M., Askarian, B., Jahed Armaghani, D., Tarinejad, R., Thai Pham, B., & Huynh, V. V. (2020). Investigating the applications of machine learning techniques to predict the rock brittleness index. Applied Sciences, 10(5), 1691.
25. Jahed Armaghani, D., Asteris, P. G., Askarian, B., Hasanipanah, M., Tarinejad, R., & Huynh, V. V. (2020). Examining hybrid and single SVM models with different kernels to predict rock brittleness. Sustainability, 12(6), 2229.
26. Daneshfaraz, R., Norouzi, R., Abbaszadeh, H., & Azamathulla, H. M. (2022). Theoretical and experimental analysis of applicability of sill with different widths on the gate discharge coefficients. Water Supply, 22(10), 7767-7781.
27. Abbaszadeh, H., Daneshfaraz, R., Sume, V., & Abraham, J. (2024). Experimental investigation and application of soft computing models for predicting flow energy dissipation in arc-shaped constrictions. AQUA—Water Infrastructure, Ecosystems and Society, 73(3), 637-661.
28. Daneshfaraz, R., Norouzi, R., Ebadzadeh, P., & Kuriqi, A. (2023). Influence of sill integration in labyrinth sluice gate hydraulic performance. Innovative Infrastructure Solutions, 8(4), 118.
29. Crookston, B. M., & Tullis, B. P. (2012). Labyrinth weirs: Nappe interference and local submergence. Journal of Irrigation and Drainage Engineering, 138(8), 757-765.

© 2025 by the authors. Licensee SCU, Ahvaz, Iran. This article is an open access article distributed under the terms and conditions of the Creative Commons Attribution 4.0 International (CC BY 4.0 license) (http://creativecommons.org/licenses/by/4.0/).

Placement of data transmission equipment in the flood warning system based on the Internet of Things (case study : Jiroft Dam Basin)

Marzieh Mohseni [*,1], Amineh Naseri [2], Leila Sheikhmamoo [1]

1. Department of Civil Engineering, Sirjan University of Technology, Sirjan, Iran.
2. Department of Computer Engineering, Sirjan University of Technology, Sirjan, Iran.

***Corresponding Author:**
Marzieh Mohseni,

Email: mohseni_m@sirjantech.ac.ir
Received: 2024.12.08
Accepted: 2025.02.16
J. Hydraul. Struct., 2025; 11(4):33-46
DOI: 10.22055/jhs.2025.48451.1331

ABSTRACT

Floods are one of the most damaging natural disasters that have increased in frequency, severity and resulting damages in recent years in Iran and around the world. One solution to reducing flood damages is to develop a flood monitoring and management system to quickly and widely communicate information and warnings to residents. Conventional methods of flood monitoring cannot provide rapid and widespread community notification. As a solution, this study focuses on an Internet of Things-based flood warning system, which is an intelligent technology capable of sending real-time information using smartphones and web services. Jiroft dam basin has been chosen for the implementation of this system. A key challenge in establishing Internet of Things-based flood warning systems lies in the strategic distribution of equipment for data collection and transmission. To address this, a hexagonal algorithm was employed for equipment placement in this study. By identifying the most flood-prone areas within the basin through the use of the K-means clustering algorithm and flood index(*f*), the study reveals the efficacy of combining these tools in determining flood potential and optimal locations for implementing flood warning systems. Following the identification of sensitive points within the basin, the study selects the Maidan sub-basin as the most susceptible to floods. Through the application of the hexagonal algorithm and a WSN-03 module with a 3.5-kilometer data transmission range, 192 suitable locations for equipment installation are pinpointed for data reception and transmission. This study will be useful for the development of early flood warning systems and reservoir management.

KEYWORDS
Hexagonal algorithm, K-means clustering algorithm, Curve number, Time of concentration.

1. Introduction

Floods are among the most destructive natural disasters, and in recent years, their frequency, intensity, and associated damages have increased in Iran and other parts of the world. A review of the history of floods in Iran reveals two main factors contributing to severe and destructive flooding. The first factor is the presence of the Zagros Mountain Range in the southwest and the Alborz Mountain Range in the northeast of Iran. Both ranges act as barriers to air flow, causing rain to accumulate on the windward sides, while central Iran remains dry. The second factor is a combination of soil type, land use, and slope, which results in minimal water infiltration and leads to sudden flash floods during rainfall [1]. These conditions have made floods the second most common natural hazard in Iran after earthquakes[2].

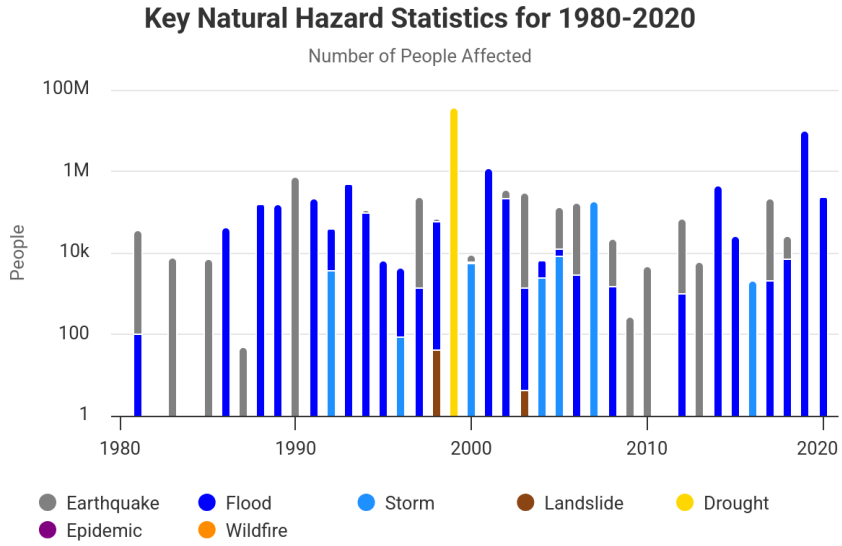


Figure 1. Main hazard risks to Iran, measured by number of people affected, for the period 1985-2020 [2]

In recent years, Iran has experienced numerous floods. For instance, in August 2001, floods in Golestan Province claimed 247 lives, and in 1986, at least 200 people lost their lives due to flooding [1].

Early and widespread flood warnings, which provide sufficient time for evacuation and property protection, are proposed as an effective solution for reducing damages and casualties. However, this is not feasible with conventional methods. In traditional approaches, warnings are often based on visual monitoring. For example, in East Java, Indonesia, each dam in Banyuwangi has a supervisor responsible for monitoring and reporting water conditions. This method is neither efficient nor practical, as the supervisor must remain in the location 24 hours, and there is no guarantee of timely and accurate information transmission [3]. As such, the development of early warning systems in developing countries faces significant technological, social, and political challenges. Additionally, the maintenance and operation of such systems by non-experts present further difficulties. Consequently, developing countries often experience far greater losses and destruction from floods compared to developed countries[4].

In flood warning detection systems, two critical factors are flood detection accuracy and the speed of data collection and transmission. One of the latest techniques for data transmission is the Internet of Things (IoT) [5]. IoT facilitates the control and connection of multiple objects via the internet. The architecture of these networks offers reliability and efficiency. Additionally, due to their minimal need for specific environmental infrastructure, ease of deployment, low energy consumption, and cost, as well as high scalability and customization based on specific measurement needs, they are highly effective [6].

Ancona et al.[7] studied the history of using IoT and wireless smart sensor networks to enhance the reliability and efficiency of flood monitoring systems. In their study, data collected from local cameras and citizen reports were transmitted via the internet to software systems, which then analyzed the data using an alert planning system. Based on the risk level, warning messages were sent to citizens.

Udo and Isong[8] described flood monitoring and detection using a wireless sensor network, where variables such as water level, rainfall intensity, relative humidity, and temperature were employed to monitor and assess flood severity. Flood

intensity was classified qualitatively as low, medium, or high, and warnings were sent to residents in the affected area. Studies by Mousa et al. [9], Madhumathi and Grace[10], and Hartono et al. [11] focused on detecting flash floods using ultrasonic and infrared sensors. Azid et al. [12] used pressure sensors to monitor water levels, sending SMS alerts when water levels exceeded predefined thresholds.

Shah et al. [13] utilized a Raspberry Pi board to collect flood data and a GSM module to send SMS alerts. Their study was conducted in a simple laboratory environment without calculating warning thresholds. Andrade and Oishi [14] recommended using SMS in wireless sensor networks (WMSNs) as a relatively simple and cost-effective method for transmitting information during natural disasters and emergencies.

In flood prediction systems designed by Mitra et al.[15] and Bande and Shete [16], data were collected using sensors, analyzed using artificial neural networks, and communicated via IoT. Citizens were alerted about flood occurrence and warnings through smartphones and internet networks.

Shalini et al.[17] focused on remote monitoring of water levels using wireless sensor networks and sending alerts through SMS, television, and radio, though they emphasized the possibility of delayed warnings.

In the flood monitoring and tracking system developed by Yuliandoko et al.[3], water depth data were processed to detect floods and assess risk levels. The risk level was directly sent from the monitoring center to residents in flood-prone areas, enhancing early flood detection. Zahir et al.[18] proposed a smart flood monitoring and control system for urban and rural areas with low cost and easy maintenance, transmitting information to users via the internet and SMS.

A key challenge in flood monitoring using IoT devices is the effective distribution of data collection and transmission equipment to avoid sensor data overlap. Over-installing IoT devices increases capital and maintenance costs and generates redundant data. Conversely, under-installing IoT devices may result in insufficient data collection for all flood parameters across different geographical locations, adversely affecting and reducing forecasting accuracy. On the other hand, determining the optimal number of IoT devices prevents investment wastage and ensures the collection of necessary data for effective flood monitoring.

Most studies have focused on equipment connectivity and notification mechanisms, with limited research on the optimal placement of IoT devices. In this regard, reference can be made to the study by Sood et al.[6] in which a hexagonal algorithm was proposed for the deployment of IoT equipment in a hypothetical environment with dimensions of 200 meters, with each basin approximately 1 meter. Jiroft watershed is one of the flood-prone areas in the country due to its dry and desert climate conditions. The presence of heavy rainfall events produces significant floods that are a major concern for the inhabitants of the region [19]. In the present study, by considering an IoT-based flood prediction and warning system in Jiroft dam bsin, the placement of IoT equipment using the hexagonal algorithm has been addressed.

2. Data, Methods and Models

2.1. Study sites and data

Jiroft dam is one of the largest concrete dams in Iran, located approximately 40 kilometers northwest of the city of Jiroft on the Halil River. The Jiroft dam basin, located in the southeast of Iran, formed the study area. The basin lies between geographical coordinates of 28° 00′ 0″–29° 58′ 0″ N latitude and 56° 29′ 0″–58° 58′ 0″ E longitude (Fig.2). The basin drainage area covers approximately 5000 km^2. The average annual rainfall in Jiroft basin is over 220 millimeters, reaching over 400 millimeters in the surrounding mountainous areas[20]. Due to the intensity of rainfall and the mountainous nature of the Jiroft watershed, floods occur frequently every year. Figure 2 shows the geographical

location of Jiroft county on the map of Iran and Kerman province, as well as the watershed of the Jiroft Dam.

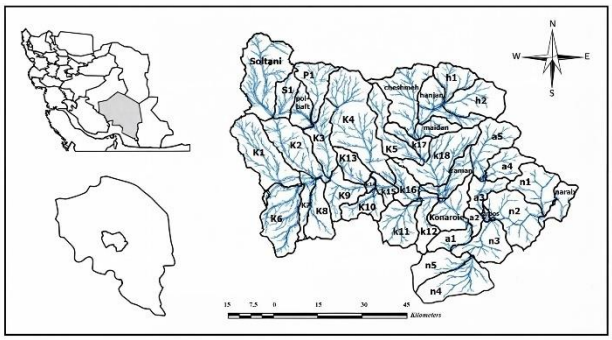


Figure 2. Graphical location of the city of Jiroft (filled by gray color) and geographical location of Jiroft dam basin and division of sub-basins [19].

The Jiroft dam basin has been divided into 43 sub-basins. The characteristics of each sub-basin, are presented in Table 1.

Table 1. Characteristics of the sub-basins of the Jiroft dam basin

No.	Sub-basin	*Slope(%)*	Area of subbasin(km^2)	No	Sub-basin	*Slope(%)*	Area of subbasin(km^2)
1	a1	0.02	78.9	23	k20	0.72	8.3
2	a2	0.73	34.4	24	k3	0.29	142.5
3	a3	0.53	93.2	25	k4	0.14	446.5
4	a4	0.07	112.4	26	k5	0.16	155.4
5	a5	0.12	175.5	27	k6	0.13	244.5
6	aroos	0.74	10.4	28	k7	0.47	72.3
7	cheshmeh	0.05	254.9	29	k8	0.36	128.4
8	H1	0.03	107.7	30	k9	0.13	128.3
9	h2	0.02	181.5	31	konaroie	0.17	146.9
10	hanjan	0.09	156.1	32	maidan	0.12	67.8
11	k1	0.12	287.7	33	n1	0.18	165.5
12	k10	0.06	94	34	n2	0.15	242.6
13	k11	0.06	167.5	35	n3	0.02	163.2
14	k12	0.32	108	36	n4	0.02	23.1
15	k13	0.3	88.9	37	n5	0.02	13.2
16	k14	0.13	12.7	38	narab	0.38	80.8
17	k15	0.3	48.6	39	p1	0.13	95.4
18	k16	0.3	91.4	40	pol-baft	0.19	71.7
19	k17	0.2	67.4	41	raman	0.3	140.1
20	k18	0.19	284.4	42	s1	0.26	76.9
21	k19	0.72	19.1	43	soltani	0.08	338.9
22	k2	0.16	217.2			0.72	8.3

2.2. Internet of Things (IoT)

The Internet of Things is a tool for collecting, filtering, and analyzing data. These data come from sources such as remote sensing, smart cameras, smart buoys, smart sensors, water level sensors, and more. After collecting the data, the Internet of Things filters and analyzes the information, providing a comprehensive view of the extent of flooding and the time of its occurrence. This process informs the community of potential dangers without wasting time [21].

2.2.1. Location of IoT Devices

One of the main challenges in monitoring floods using IoT devices is the appropriate distribution of equipment for receiving and sending data in a way that sensor data do not overlap. Determining the appropriate number of IoT transmission devices prevents investment waste and collects the necessary data for effective flood monitoring. If a small number of IoT devices are installed, they will not be able to collect all the information related to flood parameters for each geographical location, thus reducing the accuracy of the system's predictions. Conversely, installing too many IoT devices increases capital, repair, and maintenance costs and generates additional data. In the present study, a hexagonal algorithm was used for the appropriate location of IoT equipment. The advantage of using hexagonal shapes is that no area is left uncovered, and the distance from the center of one hexagon to the center of another hexagon is equal. An example of the proposed structure is shown in figure 3. The origin coordinates and axes are clearly indicated in this figure. In this two-dimensional coordinate system, the origin coordinates are the most sensitive area in the watershed to flooding, the x-axis is in the direction of the slope of the watershed, and the y-axis is in the direction of the width of the watershed.

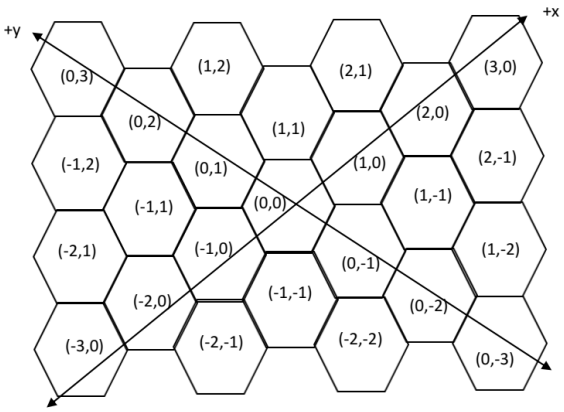


Figure 3. Implementation of the hexagonal algorithm[6]

The implementation of the hexagonal algorithm in the study area is presented in algorithm 1. In algorithm 1, it is assumed that each IoT device covers a hexagonal area with a radius R (the coverage radius of data transmission and reception equipment) to collect data at the desired rate and improve data transfer speed for processing. The size of the hexagon and the number of IoT devices to be installed are interdependent, the number of hexagons is determined based on the coverage area of IoT devices. In other word, the radius of the hexagons is selected according to the board of the receiving and transmitting modules, This means that, with an increase or decrease in the radius of each module's board, the selected radius of each hexagon and consequently the number of hexagons will also change. For example, in this study, a WSN-03 module with a board of 3.5 kilometers has been considered, which will cover an area of approximately 31.85

km^2. If a module with a different board is used, this coverage area will certainly change, resulting in a corresponding variation in the number of devices required.

Algorithm1. The hexagon division algorithm of the geographical area is as follows:

Step 1: Choose the most sensitive watershed area in flood formation as the origin.
Step 2: Set the axis directions:
x-axis from the highest point in the watershed (+x) to the lowest point in elevation (-x)
y-axis: width of the watershed.
Step 3: Set the radius of each hexagon to half the device length (R/2) for each hexagon center to have the same distance.
Step 4: Install each IoT device at the center of the hexagon to cover the radius area (R/2) and obtain the coordinates of the hexagon centers.
Step 5: Record the latitude and longitude of the origin coordinates for geographical reference and obtain the geographical locations of the hexagon centers.

2.3. Flood potential of the Jiroft dam sub-basins

The first step in algorithm 1, is to determine the most sensitive point to floods in the desired watershed. In this section, the determination of the flood potential of the watershed is addressed. Different indicators are used to identify locations with high flood potential. Among the most important and practical indicators used in this regard are the F% and *f* index, which work based on peak discharge extracted from mathematical models. These indicators have been used in various studies, such as the study by Solaimani Sarood et al. [19]. In this study, the Jiroft dam basin is divided into 43 sub-basins, and using the HEC-HMS precipitation-runoff model and RS, GIS techniques, the F% and *f* indicators are calculated. To achieve this, the curve number must first be estimated. In order to determine the curve number in the sub-basins, a soil texture map of the area was initially prepared. Subsequently, using hydrological soil group tables, a hydrological soil map was created. Based on this hydrological soil map, the majority of the area is classified into groups B and C. In the next step, utilizing satellite images and remote sensing techniques, a land use map of the area was produced. The results indicated that a significant portion of the area consists of rock-bare soil, which have a high potential for flooding. Following this, by integrating the hydrological soil map and the land use map, a curve number (CN) map for the watershed was drawn. It should be noted that the findings of Solaimani Sarood et al. [19] were also utilized in these cases. The estimated values for each sub-basin are presented in table 2.

Table 2. Flood index values for the hydrological units of Jiroft dam basin

No.	Sub-basin	CN	*f*	F (%)	No	Sub-basin	CN	*f*	F (%)
1	a1	82.1	0.57	2.7	23	k20	77	0.54	0.27
2	a2	81.3	0.55	1.14	24	k3	77.1	0.52	4.47
3	a3	90.1	0.62	3.47	25	k4	78.1	0.6	16.12
4	a4	87.1	0.48	3.24	26	k5	91.1	0.67	6.29
5	a5	82.1	0.54	5.73	27	k6	94.1	0.76	11.18
6	aroos	78	0.46	0.29	28	k7	88.1	0.63	2.72
7	cheshmeh	75.2	0.48	7.37	29	k8	90.1	0.64	4.98
8	H1	73.1	0.46	2.99	30	k9	92.1	0.71	5.53
9	h2	75	0.44	4.86	31	konaroie	84.1	0.62	5.49
10	hanjan	92	0.74	7.01	32	maidan	90.1	0.71	2.9
11	k1	84.1	0.62	10.79	33	n1	82.1	0.62	6.18
12	k10	88	0.64	3.65	34	n2	78.1	0.57	8.42
13	k11	93.1	0.57	5.81	35	n3	77.2	0.57	5.58
14	k12	78.1	0.51	3.31	36	n4	74.1	0.53	0.74
15	k13	88.1	0.55	2.98	37	n5	67.8	0.39	0.31
16	k14	84.3	0.54	0.42	38	narab	74.4	0.48	2.34
17	k15	82.1	0.53	1.56	39	p1	73.2	0.48	2.77
18	k16	76.5	0.45	2.5	40	pol-baft	87.1	0.67	2.91
19	k17	78.5	0.46	1.88	41	raman	83.1	0.63	5.32
20	k18	91.1	0.72	12.47	42	s1	84.2	0.66	3.06
21	k19	88.1	0.66	0.77	43	soltani	84.5	0.65	13.24
22	k2	79.2	0.57	7.43					

The results of this study showed that the values extracted using the *f* indicator have a correlation coefficient of 0.813 with the curve number values (CN), such that the *f* indicator values change linearly with the change in curve numbers , as shown in figure 4.

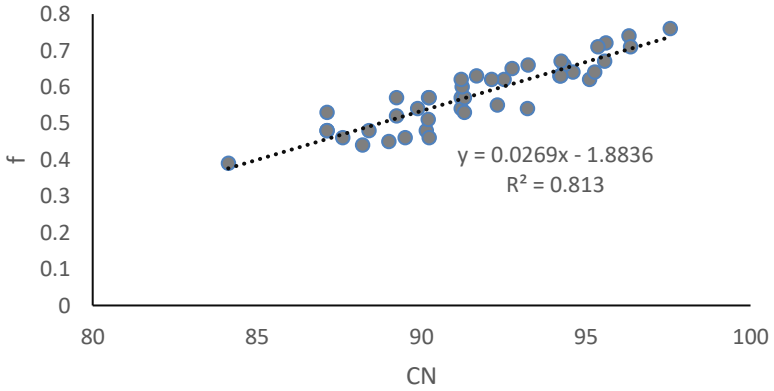


Figure 4. Relationship between curve number (CN) and *f* indicator values

In the Saghafian and Farazjou[22] study, the researchers highlighted the importance of incorporating concentration time into flood warning projects, alongside flood indicators. The study of the Golestan watershed demonstrated that the combination of geographic information systems and hydrological models can reveal the impact of physiographic and climatic factors on flood potential. The researchers also found that a sub-basin with a larger area or higher peak discharge does not necessarily have a greater impact on the total watershed runoff, but the spatial location of sub-basin and river routing also play significant roles. In the current study, the clustering method have been used to determine the flood potential of the sub-basins of the Jiroft dam watershed. The values of curve number and time of concentration for each sub-basin are specified in Table 3.

Table 3. Curve number values and time of concentration in Jiroft dam catchment

No.	Sub-basin	**CN**	time of concentration (min)	No.	Sub-basin	CN	time of concentration (min)
1	a1	82.1	42	23	k20	77	27.5
2	a2	81.3	35.38	24	k3	77.1	33.83
3	a3	90.1	52	25	k4	78.1	41
4	a4	87.1	35.83	26	k5	91.1	39.17
5	a5	82.1	68.67	27	k6	94.1	41
6	aroos	78	35.5	28	k7	88.1	47.83
7	cheshmeh	75.2	40.83	29	k8	90.1	44.17
8	H1	73.1	42.67	30	k9	92.1	71.33
9	h2	75	17.37	31	konaroie	84.1	59.33
10	hanjan	92	36.83	32	maidan	90.1	68.67
11	k1	84.1	40.33	33	n1	82.1	75.53
12	k10	88	64.17	34	n2	78.1	67.02
13	k11	93.1	47.83	35	n3	77.2	67.17
14	k12	78.1	35.5	36	n4	74.1	64.08
15	k13	88.1	28.17	37	n5	67.8	85.38
16	k14	84.3	40.5	38	narab	74.4	33.5
17	k15	82.1	35.5	39	p1	73.2	70.6
18	k16	76.5	34.33	40	pol-baft	87.1	52.17
19	k17	78.5	31.17	41	raman	83.1	42.67
20	k18	91.1	28.93	42	s1	84.2	41.33
21	k19	88.1	34.17	43	soltani	84.5	46.3
22	k2	79.2	31.17				

2.3.1. K-means clustering

Data clustering approach has been used for ranking the flood levels. There are several clustering techniques available, with K-means being one of the most commonly used methods. However, it is important to note that K-means can be heavily influenced by the number of clusters chosen and the initial data provided. The value of K in K-means clustering is used to categorize the levels of flood intensity. For instance, a level

of 0 suggests that there is no risk of flooding, while a level of K signifies a high alert for the area under impact. The upcoming algorithm describes the definition of predate and the clustering method [6].

Algorithm2. K-means clustering algorithm

Require: K, number of clusters; D, a data set of N points
Ensure: A set of K clusters

1. Data points: A set of individual data points is scattered throughout the diagram.
2. Centroids: K number of centroid points are initialized at random locations within the data points.
3. Cluster assignments: Each data point is assigned to the nearest centroid, forming K clusters.
4. Centroid update: The centroids are updated by calculating the mean of the data points in each cluster.
5. Iteration: The process of assigning data points to clusters and updating centroids is repeated until convergence, i.e., when the centroids no longer change significantly between iterations.

Determining the optimal number of clusters is important. In this study, the Silhouette coefficient was used to determine the optimal number of clusters due to its efficiency and simplicity of implementation in MATLAB software. Using this coefficient, the degree of membership of each data point to the cluster, it belongs to is measured.

2.3.1.1. Silhouette Method

The Silhouette method was first introduced by Peter.J. Rousseeuw[23]. The Silhouette method is widely used in determining k value or the number of clusters. K value is determined by the average Silhouette coefficients. For points in i in cluster A, the formula of s(i) for i in cluster from Silhouette of i is as follows:

$$s(i) = \frac{b(i)-a(i)}{\max\{a(i),b(i)\}}, \quad -1 \le s(i) \le 1 \qquad (1)$$

Where: s(i) represents the coefficient indicating the level of membership of a data item (e.g., data i to its respective cluster (e.g., cluster A) following the cluster operation. Meanwhile, a(i) signifies the average distance of data i from other data items within cluster A, and b(i) denotes the smallest average distance of data i within cluster A to other data items in any cluster E that differs from cluster A.

In practical terms, the silhouette coefficient is initially computed for each data item using the equation 1. Subsequently, the average silhouette coefficient $\bar{s}(k)$ is derived for all available data (n) within each cluster (k) through the utilization of equation 2.

$$\bar{s}(k) = 1/n \sum_{i=1}^{n} s(i) \qquad (2)$$

Interpretation of different ranges of silhouette coefficient is presented in Table 4.

Table 4. Guide to interpretation of the silhouette coefficient[24]

Type	Interval silhouette coefficient	Interpretation
1	0.71 – 1.0	The strong structure has been discovered
2	0.52 – 0.70	Reasonable structure has been found
3	0.26 – 0.50	The weak structure may mock
4	< 0.25	Not found substantial structure

2.3.1.2. Data Normalization

Data normalization, also known as standardization of data, is the process of adjusting data values to a common scale)in the range of [0, 0.9] (in this context) in order to facilitate comparison of the data in different ranges.

$$z = 0.1 + 0.8 * \frac{x_i - x_{imin}}{x_{imax} - x_{imin}} \quad (3)$$

In which: z is the standardized variable, x_i is the initial variable, x_{imin} and x_{imax} are the minimum and maximum values of variable x_i , respectively[25].

3. Results and Discussions

3.1. clustering Results

The results related to the effect of the number of clusters on the distance and silhouette coefficient are presented in table 5, as this algorithm is based on unsupervised methods, the silhouette coefficient has been used to find the best number of clusters. As can be seen, the best result is related to the number of 9 clusters.

Table 5. Distance and silhouette coefficient for number of clusters

Number of clusters	silhouette coefficient	Distance in best fit
10	0.78	3.034
9	0.97	2.99
8	0.87	3.6
7	0.791	3.339
6	0.76	3.76
5	0.61	4.138

In Table 6, the results of clustering algorithm based on 9 clusters in the Jiroft dam basin are presented. In this table, cluster 1 sub-basins have the lowest potential for flood, while cluster 9 sub-basins have the highest flood potential. The results of the clustering algorithm differed from those obtained from the flood indicator *f* in some cases. This discrepancy arose because, in clustering method, in addition to the CN parameter, the time of concentration is also considered a very important parameter for prioritizing areas susceptible to flooding. This case, namely the impact of concentration time on determining the flood potential of a watershed, has been confirmed in the study by Saghafian and Farazjou[22]. Based on the results presented in Table 5, sub-basins k9, K10, and Maidan are placed in cluster 9. To select the most sensitive area, the results of the study by Solaimani Sarood et al.[19] have been used. The values of the flood index *f* for sub-basins k9, K10, and Maidan are 0.64, 0.71, and 0.71 respectively. By comparing the results of the present study and the flood index values, the Maidan sub-basin was selected as the most sensitive area (Fig.5). Based on the hydrological soil map of the region, the majority of the soil in the Maidan sub-basin falls within hydrological groups B and C. The land use of Maidan is classified as rock-bare soil, with an average slope of 0.38% and curve number of 95.36. These characteristics clearly indicate that this sub-basin has a very high potential for flood generation. Furthermore, the short distance of this sub-basin to the Jiroft dam, in comparison to sub-basins K9 and K10, makes it a logical choice for identifying the most effective area for flood production in the Jiroft dam watershed. This analysis is entirely consistent with the results of the K-means algorithm and the findings of Solaimani Sarood et al. [19].

Table 6. Results of the clustering algorithm for different areas

No.	sub basin	Cluster number	Distance to centerpoint	No.	sub basin	Cluster number	Distance to centerpoint
1	a1	4	0.059295	23	k20	3	0.089571
2	a2	4	0.061506	24	k3	2	0.023408
3	a3	7	0.088125	25	k4	4	0.055273
4	a4	2	0.044694	26	k5	7	0.06575
5	a5	5	0.04509	27	k6	7	0.13227
6	aroos	2	0.006774	28	k7	7	0.081976
7	cheshmeh	2	0.084785	29	k8	7	0.013878
8	H1	2	0.13482	30	k9	9	0.066619
9	h2	3	0.10365	31	konaroie	8	0.071905
10	hanjan	7	0.10549	32	maidan	9	0.008537
11	k1	4	0.020741	33	n1	5	0.082364
12	k10	9	0.067605	34	n2	5	0.03339
13	k11	8	0.071905	35	n3	5	0.078863
14	k12	2	0.048246	36	n4	6	0.12427
15	k13	1	0.040151	37	n5	6	0.18489
16	k14	4	0.062834	38	narab	3	0.11547
17	k15	4	0.078261	39	p1	6	0.067764
18	k16	2	0.027914	40	pol-baft	7	0.11381
19	k17	2	0.072625	41	raman	4	0.038072
20	k18	1	0.056001	42	s1	4	0.064664
21	k19	1	0.04972	43	soltani	4	0.076295
22	k2	2	0.07181				

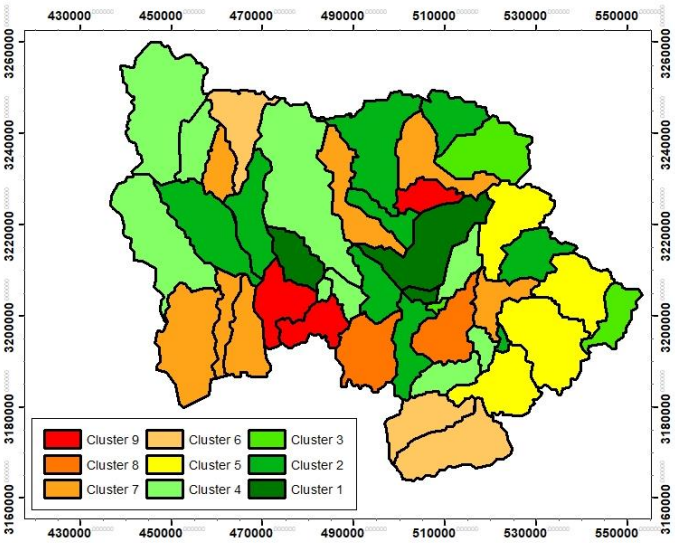


Figure 5. Clustering map of Jiroft dam basin

3.2. Geolocation results of IOT devices

The implementation of hexagonal algorithm in Jiroft dam basin is shown in figure 6. After selecting the Maidan station as the most flood-prone area, this station is

chosen as the origin of coordinates and the x and y axes are drawn as described in Algorithm 1. Starting from the origin of coordinates, hexagons with a radius of 3.5 kilometers (equivalent to the WSN-03 module range) are drawn. The drawing of hexagons continues until the entire watershed area is covered. After drawing the hexagons, the coordinates of the centers of the hexagons are taken as the location for installing IoT equipment, then using the geographic information software ArcGIS, these coordinates are converted to Universal Transverse Mercator coordinate system(UTM). Based on this, the coordinates of 192 points for installing equipment were identified for the installation of equipment. The coordinates of these points are presented in table 6 (due to the large number of points, only a few of them are presented in table 6).

Considering the costs of IoT devices, the implementation of this algorithm will lead to significant savings in installation and maintenance expenses, making the IoT-based flood prediction and warning system economically viable. Another important aspect to address is the energy saving for flood system. By implementing an algorithm to systematically shutdown and activation of devices, some of the IoT devices are put in sleep mode where the flood magnitude and probability of flooding is negligible. However, it is essential that the shutdown of the modules be conducted in a way that does not hinder data transmission and reception.

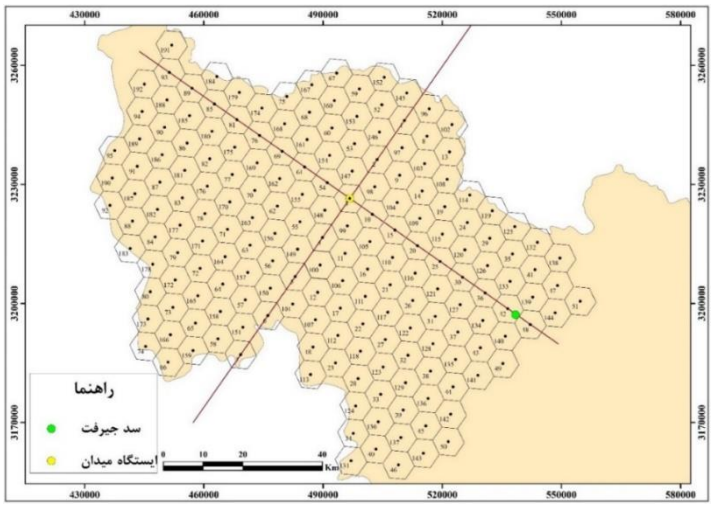


Figure 6. Implementation of the hexagonal algorithm in the Jiroft Dam catchment area

Table 7. Geographic coordinates of the IOT equipment installation location

Location number	Utm(X)	Utm(Y)	Location number	Utm(X)	Utm(Y)	Location number	Utm(X)	Utm(Y)
1	510507.92	3246122.7	39	510205.99	3173130.2	78	460294.88	3222656.8
2	503633.24	3236287.1	40	503331.31	3163294.6	79	453420.2	3212821.2
3	496758.56	3226451.5	41	543383.29	3208503.4	80	446545.52	3202985.6
4	489883.88	3216616	42	536508.61	3198667.9	81	468365.66	3246297
5	483009.2	3206780.4	43	529633.93	3188832.3	82	461490.98	3236461.5
6	476134.52	3196944.8	44	522759.25	3178996.7	83	454616.3	3226625.9
7	469259.84	3187109.2	45	515884.57	3169161.1	84	447741.62	3216790.3
8	516186.5	3242153.6	46	509009.89	3159325.5	85	462687.08	3250266.1
9	509311.82	3232318	47	549061.87	3204534.3	86	455812.4	3240430.6

4. Conclusion

In flood warning systems, two important factors exist: the accuracy of flood detection and the speed of data transmission. The timely and rapid transmission of information in conventional flood warning systems may not be possible, therefore, in this study, internet of things (IoT)-based flood warning systems have been considered. One of the challenges in these systems is the optimal placement of equipment for data transmission in a way that ensures complete data collection without overlapping. In this study, a hexagonal algorithm was used for proper location placement of IoT devices in the Jiroft dam watershed. The first step in implementing the hexagonal algorithm is determining the most sensitive flood-prone area. For this purpose, two methods, K-means clustering and the flood index *f*, were utilized. By comparing the results of these two methods, the Maidan sub-basin was identified as the most sensitive sub-basin, with this sub-basin chosen as the coordinate origin. Subsequently, hexagons were drawn with a radius of R/2 (the radius of the equipment's data transmission range) in a way that covered the entire watershed. The centers of these hexagons were determined, and local coordinates were transformed into UTM coordinates using ArcGIS software. In this study, the coordinates of 192 points were introduced for the installation of equipments. The results of this study will be useful in identifying challenges in the design and evaluation of IoT-based flood prediction and warning systems.

Acknowledgments

This study was funded by Regional water Company of Kerman(Grant numbers :402/04). The authors would like to thank to Kerman Regional Water Company (Research, Planning, and Economic Studies Department) for their financial support of this research.

References

1. Vaghefi SA, Keykhai M, Jahanbakhshi F, Sheikholeslami J, Ahmadi A, Yang, H, Abbaspour KC, (2019). The Future of Extreme Climate in Iran. Scientific Reports 9, Article 1464.
2. World Bank. (2019). Climate Knowledge Portal. [online] Available at:https://climateknowledge portal.worldbank.org/country/iran [Accessed 9 Apr. 2019].
3. Yuliandoko H, Subono S, WardhaniVA, Pramono Sh.H, Suwindarto P, (2018). Design of flood warning system based iot and water characteristics. TELKOMNIKA (Telecommunication Computing Electronics and Control), 16(5), pp: 2101-2110.
4. Basha E, Rus D, (2007), Design of Early Warning Flood Detection Systems for Developing Countries. International Conference on Information and Communication Technologies and Development. Technologies and Development 2007 Dec 15, IEEE: 1-10.
5. Rani Dola Sh, Jayalakshmi GN, Baligar VP, (2020). Low cost IoT based flood monitoring system using machine learning and neural networks: flood alerting and rainfall prediction. 2nd International Conference on Innovative Mechanisms for Industry Applications (ICIMIA), pp: 261-267.
6. Sood SK, Sandhu R, Singla K, Chang V, (2018). IoT, big data and HPC based smart flood management framework. Sustainable Computing: Informatics and Systems 20, pp: 102-117.
7. Ancona M, Dellacasa A, Delzanno G, Camera AL, Rellini I, (2015). An "Internet of Things" vision of the flood monitoring problem. InProc. 5th Int. Conf. Ambient Comput., Appl., Services Technol, pp:26-29.
8. Udo EN, Isong EB, (2013). Flood monitoring and detection system using wireless sensor network. Asian journal of computer and information systems, 1(4).
9. Mousa, M., Zhang, X. and Claudel, C., 2016. Flash flood detection in urban cities using ultrasonic and infrared sensors. IEEE Sensors Journal, 16(19):7204-7216.

10. Madhumathi M, Grace R, (2017). Flood alert management system using iot and microcontroller. International Journal of Innovative Research in Computer and Communication Engineering, 5(4).
11. Hartono A, Satira S, Djamal M, Ramli M, (2017). Characterization Analysis of PVDF Thin Films Fabricated Using Deep Coating Machines. In International Conference on Science and Technology-Promoting Sustainable Agriculture, Food Security, Energy, and Environment Through Science and Technology for Development: 129-132.
12. Azid ShI, Sharma BN, Raghuwaiya K, Chand A, Prasad S, Jacquier A, (2015). SMS based flood monitoring and early warning system. ARPN Journal of Engineering and Applied Sciences, 10(15), pp: 6387-6391.
13. Shah WM, Arif FA, Shahrin A, Hassan A, (2018). The implementation of an IoT-based flood alert system. International journal of advanced computer science and applications 9(11).
14. Andrade MVA, Oishi S, (2014). A Wireless Mesh Sensor Network framework for river flood detection which can be used as a emergency communications network in case of disaster. 104, pp: 284.
15. Mitra P, Ray R, Chatterjee R, Basu R, Saha P, Raha S, Barman R, Patra S, Biswas SS, Saha S, (2016). Flood forecasting using Internet of things and artificial neural networks. 7th Annual Information Technology, Electronics and Mobile Communication Conference: 1-5.
16. Bande S, Shete VV, (2017). Smart flood disaster prediction system using IoT and neural networks. International Conference On Smart Technologies For Smart Nation (SmartTechCon), pp:189-194.
17. Shalini E, Surya P., Thirumurugan R, Subbulakshmi S, (2016). Cooperative flood detection using SMS through IoT. Int. J. Adv. Res. Elect., Electron. Instrum. Eng, 5(3), pp: 3410-3414.
18. Zahir Sh, Ehkan B, Sabapathy Ph, Jusoh Th, Osman M, Yasin M.N, Wahab M N, et al. (2019). Smart IoT flood monitoring system. Journal of physics: conference series, 1339(1), 012043.
19. Solaimani Sarood F, Soltani Kopaii S, Salajeghe A, (2013). Selection of Appropriate Flooding Potential Index by Using RainfallRunoff (HEC-HMS) Model and RS & GIS Techniques in Jiroft Dam Basin, Journal of Watershed Management Research, 4(8), pp:90-105.
20. Sarai MH, Mahmoudi I, Bidsheki A, Kamandari M, (2017). A Study of the Geographical Distribution of Crimes in the Areas of Jiroft City Between 2008-2011. Journal of Geography and Urban Planning Zagros Landscape, 9(33), pp: 21-43.
21. Van Ackere S, Verbeurgt J, Sloover LD, Gautama S, Wulf AD, Maeyer Ph, (2019). A review of the internet of floods: Near real-time detection of a flood event and its impact. Water 11(11), pp: 2275.
22. Saghafian B, Farazjou H, (2007). Determination of place causing flood and respecting the floating of hydrologic units of Golestan Dam catchment. Journal of Iran Watershed Management, 1, pp:1-11, (In Persian).
23. Wulandari S, (2020). Analyze k-value selected method of k-means clustering algorithm to clustering province based on disease case. International Journal of Innovative Technology and Exploring Engineering (IJITEE), 9(3), pp:121-124.
24. Sari BN, (2016). Identification of Tuberculosis Patient Characteristics Using K-Means Clustering. Scientific Journal of Informatics, 3(2), pp:129-138.
25. Tabatabaei M, Solaimani K, Habibnejad Roshan M, Kavian A, (2015). Estimation of Daily Suspended Sediment Concentration Using Artificial Neural Networks and Data Clustering by Self-Organizing Map (Case Study: Sierra Hydrometry Station- Karaj Dam Watershed) . J Watershed Manage Res. 5(10), pp: 98-116, (In Persian).

© 2025 by the authors. Licensee SCU, Ahvaz, Iran. This article is an open access article distributed under the terms and conditions of the Creative Commons Attribution 4.0 International (CC BY 4.0 license) (http://creativecommons.org/licenses/by/4.0/).

Analysis of Supply Chain Risks in Concrete Dam Construction

Mohammad Mirzaahmadi [1], Hamed Sarkardeh [*,2],Ali Katebi [1], Ayda Mirzaahmadi [3]

1. Department of Civil Engineering, University of Kharazmi, Tehran, Iran.
2. Department of Civil Engineering, Hakim Sabzevari University, Sabzevar, Iran.
3. Department of Civil Engineering and Environment, NTNU, Trondheim, Norway.

***Corresponding Author:**
Hamed Sarkardeh,

Email: sarkardeh@hsu.ac.ir
Received: 2024.10.05
Accepted: 2025.02.21
J. Hydraul. Struct., 2025; 11(4):47-56
DOI: 10.22055/jhs.2025.48099.1324

ABSTRACT

This study identifies 35 risks related to the supply chain of concrete dams, of which 25 were selected as critical risks using the Delphi method. Risks were categorized into three groups based on their sources including environmental, network and organizational risks. The Failure Mode and Effect Analysis (FMEA) method was then applied to evaluate the significance of risks in three areas of construction cost, time and quality. The results revealed that 44% of risks in the construction cost category were critical, while 21% of risks in construction time and 12% in construction quality were found to be critical. Appropriate responses to mitigate critical risks were provided, including the use of alternative supply resources, rigorous project scheduling, and diversified financial strategies. This study highlights the importance of risk management in improving project performance in terms of cost, time, and quality, and emphasizes the need for effective communication and continuous risk monitoring throughout the project lifecycle.

KEYWORDS

Supply Chain; Risk Assessment; Concrete Dam; Construction Management; Project Management.

1. Introduction

Application of new technologies and modern management methods has caused a significant growth in construction industry. It has also raised the number of chain supply suppliers to acquire raw materials and services. Therefore, it is essential to communicate with different suppliers, employees, departments and organizations as a team to guarantee the best function [1]. Partners' complex international networks, unpredictable demand, increased costs, use of outsourcing, have raised dependence between different supply chain segments [2]. Affiliation of different supply chain sectors has created many internal and external risks such as economic crises, natural disasters or political conflicts, whose occurrence in any part of supply chain which can directly or indirectly affect other areas [3]. Different kind of risks disturbed supply chain and affected global industry [4]. The supply chain is usually convergent in manufacturing industry and in the construction industry, supply chain activities lead to the production of a product and there may be different risks of varying importance [5]. One of the characteristics of construction of a unique product in a specific location is that different parts of the supply chain are occupied different distances, which are related to the location of products and have acquired deeper insight about this location [6].

The construction industry has been generally characterized by low integration, low productivity, cost and extra time, several conflicts and disagreements over other industries. These problems are rooted in supply chain disruptions in this industry [7]. Attention to supply chain risks management for eliminating or reducing the effects of failures, which arise from potential risks in different sectors such as economic issues, natural disasters or human errors, seems to be necessary [8]. Dam construction as one of the oldest industries, involving many countries, is considered the subset of manufacturing. Dam construction projects are mostly implemented in a relatively long period of time and require significant financial resources [9]. In the context of examining risks in the construction sector, Chen et al. analyzed financial and credit risks in the real estate sector [10]. Wang et al. investigated the impact of adverse weather conditions on the supply chain risks associated with prefabricated structures [11]. Studies show that the cost is estimated to be double for one out of five dams and triple for one out of ten [12]. They should always be designed and constructed with consideration of all aspects because the weakness in the quality of the finished project can cause considerable damages [13]. There have been several studies in field of risks identification and investigation. In one case, supply chain risks, including demand change, manufacturing new product, lack of durable products and delay in supply in products, were investigated by Johnson, working on another field, toy industry [14]. In another research, Qaraqanabadi and Sarkardeh examined supply chain risks in road construction projects [15]. Wilson worked on the effect of transportation on supply chain function by introducing some factors leading disruption of supply chain [16]. Gaudenzi evaluated supply chain risks by AHP method, which includes resource shortage, lack of coordination between different parts, incorrect prediction, lack of information system as well as error in estimation and lack of depot [17]. Supply chain also was investigated by Tuncel and Alpan via FMECA method. In their research, shortage of initial materials, human errors and problems related to equipment were considered as parts of supply chain risks [18]. Giri and Bardhan worked on investigation of supply chain integration method in case of disruptions, such as political instability, labor strikes, earthquakes, fires, disruptions of transit system and floods [19]. In a study conducted by Yang and Xu, several risks like recession, financial fluctuations and lack of liquidity are categorized as supply chain risks [20]. Investigation of the causes of some problems, such as project delay and increasing of costs, in dam construction projects indicates the probability of problem in supply chain management. Some factors, like error in determination of request for initial material, natural hazard, change in plans, are important reasons for delay in dam construction project in Oman [21]. In other example, difference between sections, lack of knowledge, shortage of equipment, incorrect planning are considered as causes for unfinished projects in dam construction area in Albania [22].

Despite to the previous studies and importance of a dam safety, no comprehensive study was performed to identify the construction risks in a concrete dam. In the present research, according to the previous researches, the supply chain risks were identified and using Delphi method, related risks of supply chain of a concrete dam construction were classified. Furthermore, using FMEA, identified risks according to possible factors are prioritized in three parts of construction cost, time and quality. Eventually, interviews were conducted with experts to find the most proper response for the most important risks.

2. Methods and Materials

2.1. Delphi method

Delphi technique helps experts to achieve a unanimous agreement about a specific topic in which to identify of participation is kept unknown [23]. Delphi method process begins with preparing an initial

questionnaire as a general strategy to find answers for researcher's questions. In the first step, a questionnaire is provided for a number of experts to both answer the question and elaborate their further viewpoint. The second questionnaire is designed based on the results of the former one. This process is continued in the next stages and each member's response is shared with others responses to be revised if required. The procedure will be continued until all responses are in coordination. In addition, in this method, each step is constructed based on the previous step [24].

2.2. Supply chain category

There are different categories of supply chain risks. The risks fall into two types of demand and supply risks. Kleindorfer categorized risks according to their source in three groups, including operational source, natural disasters and political source where risks related to concrete dams supply chain, based on their source, are categorized in three groups of environmental, network and organizational risks. Environmental risks include all risks and factors out of supply chain, leading to uncertainty in supply chain functions and can be caused by accidents, social and political actions or natural disasters. Network risks refer to the ones resulting from organizations interactions in supply chain; accordingly, damages rooted in uncoordinated interactions between organization fall in this category. Organizational risks include the risks which are directly involved in main organization boundaries [25-27].

2.3. Identification and classification of concrete dams supply chain

The initial questionnaire, in the present study which was prepared in Delphi method, included questions related to concrete dams supply chain risks choices among 35 identified risks. Furthermore, the source of each risk was investigated. This questionnaire was distributed among seven experts of dam construction area. Ultimate responses were achieved in three steps, in which experts answered and modified the questions. The identified supply chain risks are indicated in Table 1. Eventually, 25 risks were identified as risks related to concrete dams supply chain, in which organizational source made up 36% of the whole risks and environmental and network source constituted 36% and 28% of all risks, respectively.

Table 1. Concrete dams supply chain risks in and the sources

Number	Risk	Risk source	Number	Risk	Risk source
1	Human error in design Incorrect	organizational	14	recession	environmental
2	estimation of initial material	organizational	15	Natural disasters	environmental
3	Lack of equipment and construction and transport technology	organizational	16	Political instability	environmental
4	Damages to equipment	organizational	17	Ownership conflicts	network
5	Transportation problems	network	18	War	environmental
6	Weakness in personnel responsibility	network	19	terrorism	environmental
7	Lack of store for material depot	organizational	20	shortage of sufficient supplier	network
8	Lack of personal hygiene	organizational	21	Lack of resources to supply materials	organizational
9	Low quality in material	organizational	22	Error in initial project schedule	organizational
10	Labor strike	network	23	Geographic and cultural unawareness	network
11	International disputes in the field of water	environmental	24	Work conflicts	network
12	Increase in interest rates	environmental	25	Changes in laws	environmental
13	Exchange rate fluctuations and price changes	environmental			

2.4. FMEA Method

FMEA is a method applied for identifying, reducing or eliminating existing and potential risks of the system and designing products, processing production or distributing prior to products reaching the customers [28]. In FMEA, after risks identification, they are estimated via calculating Risks Priority Number (RPN) for both potential errors and their effects. RPN = S×O×D is obtained by finding the multiplication of three factors, involving the severity of the failure (S), the probability of occurrence (O) and probability of detection (D). These three factors are categorized in a qualitative scale from 1 to 10. Risk priority number is the basis for prioritizing the failure scenario. According to 1-10 domain for these three factors, RPN will have a number between 1 to 1000 [26]. RPN analysis method is one of the most significant requirements in FMEA. Several researchers have identified the value of RPN as priority criteria, yet this category is not sufficient for risks mode analysis since risks deterioration is not taken into account. For instance, although different combination of S, O and D can present equal RPNs, the consequences of each risk and its modes may be different. Moreover, risk priority number is sensitive to disparity in risks factors evaluation. A slight change in number of each factor leads to a major change in RPN, which in turn causes change in grade. In this research, due to the importance of these three factors of severity of the failure, the probability of occurrence and the probability of detection, a criterion is defined and applied as crisis levels explained in detail as follows [29]:

Level 1: normal level, in which all three RPN factors (especially severity and possibility of occurrence) have a value less than 5, or RPN value is very low (RPN<70). This case does not require corrective and preventive actions.

Level 2: semi-critical, in which at least one out of three factors (especially severity and possibility of occurrence) has a value more than 5, or RPN value is moderate or low (70<RPN<140). This case requires corrective and preventive actions.

Level 3: critical level, in which at least two out of three factors (especially severity and possibility of occurrence) have a value more than 5, or RPN value is very high (RPN>140). It is clear that corrective and preventive actions are essential in this case.

2.5. RPN calculation and crisis level determination of concrete dams supply chain

The questionnaire based on FMEA is used for obtaining data which leads to RPN. Each risk in three sectors, severity of the failure, the probability of occurrence and the probability of detection, in three areas, including construction cost, construction time and construction quality are investigated by dam construction experts. Statistical population includes dam construction experts, who are 34 members directly working at least 15 years on dam projects in fields of constructing and designing from beginning to end of project. Table 2 shows the result of cost construction part achieved from analysis of questionnaire [30]. Regarding to these results, the most important risks, in this area, are exchange rate fluctuations, shortage of liquidity, Increase in interest rates. Moreover, the lowest levels of importance are related to disruptions of transit system, shortage of depot, shortage of sanitation. In another part of this study, the importance of risks on construction time is evaluated. According to Table 3, the risks of shortage of liquidity, delay in activities and international conflicts have the highest impact on ultimate time, and the lowest impact is related to shortage of materials quality, shortage of depot and lack of hygiene. The effect of risks on construction quality is shown in Table 4. The results indicate that risks of international conflicts, exchange rate fluctuations and human errors are most effective, and disruptions of transit system, ownership conflicts and shortage of depot have the lowest significance in this part.

Table 2. The Importance of Risks on Construction Cost

Risk	RPN	Crisis level	Risk	RPN	Crisis level
Exchange rate fluctuations and price changes	258.70	critical	Changes in laws	102.75	Semi-critical
Error in initial project schedule	234.80	critical	Workforce strikes	89.06	Semi-critical
Increase in interest rates	229.01	critical	Political instability	77.35	Semi-critical
International conflicts	221.50	critical	Shortage of equipment and technology	67.61	Normal
recession	221.37	critical	Lack of materials quality	62.49	Normal
Weakness in personnel responsibility	210.90	critical	war	55.75	Normal
Lack of resources to supply materials	159.26	critical	Equipment damage	51.90	Normal
shortage of sufficient supplier	138.65	critical	Ownership conflicts	40.10	Normal
Human error in design Incorrect	135.98	critical	terrorism	39.54	Normal
Natural disasters	129.09	critical	Disruptions of transit system	39.44	Normal
Estimation of initial material	123.71	Semi-critical	Shortage of sanitation	29.34	Normal
Geographic and cultural unawareness	110.87	Semi-critical	Shortage of depot	25.00	Normal
Work conflicts	105.91	Semi-critical			

Table 3. The importance of risks on construction time

Risk	RPN	Crisis level	Risk	RPN	Crisis level
Error in initial project schedule	265.69	critical	Incorrect estimation	100.18	Semi-critical
Weakness in personnel responsibility	237.26	critical	Changes in laws	90.83	Semi-critical
International disputes in the field of water	220.06	critical	Shortage of equipment and technology	82.97	Semi-critical
recession	219.99	Semi-critical	Political instability	78.96	Semi-critical
Human error in design Incorrect	194.39	critical	war	64.29	Semi-critical
shortage of sufficient supplier	188.57	critical	Equipment damage	57.39	normal
Exchange rate fluctuations and price changes	156.91	Semi-critical	Disruptions of transit system	49.98	normal
Increase in interest rates	154.84	Semi-critical	Ownership conflicts	47.45	normal
Natural disasters	129.09	Semi-critical	terrorism	45.92	normal
Work conflicts	126.38	Semi-critical	Lack of materials quality	45.40	normal
Geographic and cultural unawareness	118.20	Semi-critical	Shortage of depot	25.38	normal
Human error in design Incorrect	116.01	Semi-critical	Shortage of sanitation	23.54	normal
Workforce strikes	106.33	Semi-critical			

Table 4. The Importance of Risks on Construction quality

Risk	RPN	Crisis level	Risk	RPN	Crisis level
International disputes in the field of water	163.96	critical	Workforce strikes	65.43	normal
Exchange rate fluctuations and price changes	142.55	critical	Timing error	64.04	normal
Lack of resources to supply materials	148.29	critical	Changes in laws	55.02	normal
shortage of sufficient supplier	127.08	Semi-critical	Incorrect estimation	54.88	normal
Human error in design	119.83	Semi-critical	Equipment damage	52.40	normal
Incorrect recession	115.70	Semi-critical	Political instability	50.76	normal
Low quality in material	104.24	Semi-critical	war	35.28	normal
Increase in interest rates	98.89	Semi-critical	Shortage of sanitation	31.19	normal
Natural disasters	90.16	Semi-critical	terrorism	26.85	normal
Lack of equipment and construction and transport technology	87.16	Semi-critical	Disruptions of transit system	24.30	normal
Weakness in personnel responsibility	77.45	Semi-critical	Ownership conflicts	22.59	normal
Work conflicts	72.09	Semi-critical	Sortage of depot	17.69	normal
Geographic and cultural unawareness	68.47	normal			

3. Results and Discussions

Results of interview with experts and using the statistical analysis were discussed in two parts of supply chain risks assessment of concrete dams and risks responses.

3.1. Assessment of Supply Chain Risks of Concrete Dams

In construction cost part, 44% of risks are in critical conditions which need an adequate response immediately. The majority of critical risks in this part have environmental source and rest of them are divided between organizational and network source. Semi-critical risks make up 26% of whole which should be investigated by risk management experts who make essential modifications during the study for prevention of such risks. Portion of network source is more than others in this part. Furthermore, crisis level of 30% of risks is normal in which organizational source is more effective than others (Figure 1). Construction time investigation indicates that 21% of risks are critical and require response straightaway. The sources of these risks are 40% organizational, 40% network and 20% environmental. Half of risks are semi-critical which must be investigated persistently, and also require an appropriate response. 58% of semi-critical risks have environmental source and rest of them have organizational and network source. Crisis level of 29% of construction time part are normal which organizational source constitutes 57% of all, environmental and network make up 14% and 29% of whole respectively (Figure 2). Risks evaluation in part of construction quality importance indicates that only 12% of all risks are in critical level which 67% of them have environmental source and 33% have organizational source. There are no risks with network source in this part. Semi-critical condition accounts for 36% of risks which have an equal portion in all three sources. In addition, 52% of risks are in normal condition in construction quality part, and the source of 38% of them is organizational; meanwhile, each of environmental and network sources make up 31% of all risks (Figure 3).

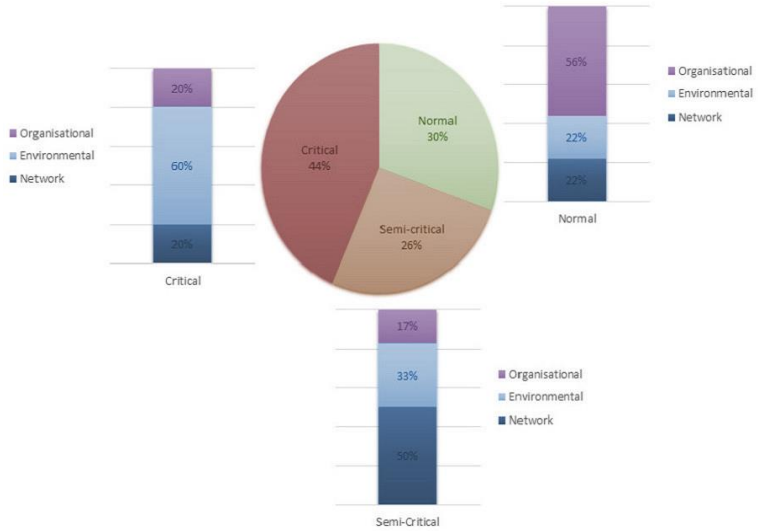


Figure 1. Risks evaluation in construction cost part

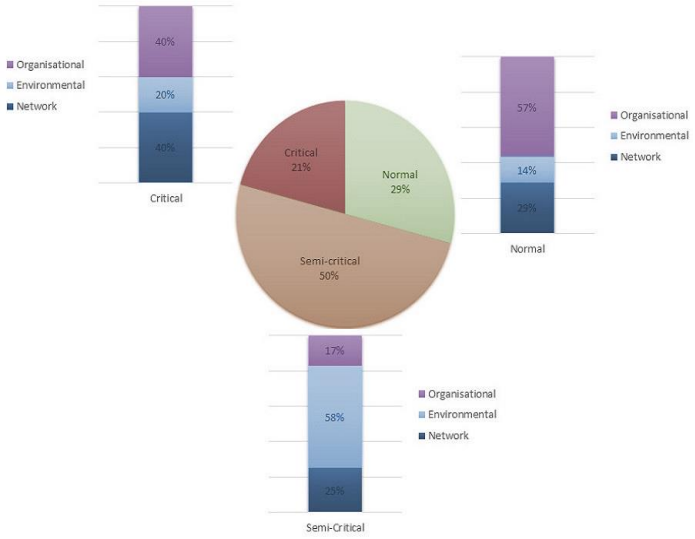


Figure 2. Risks evaluation in construction time

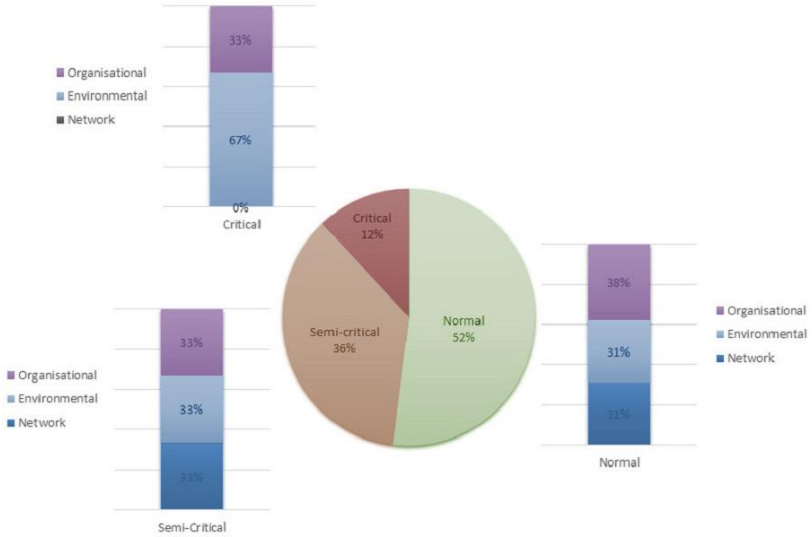


Figure 3. Risks evaluation in construction quality

3.2. Responses to the risks

Organizations should take corrective actions as soon as possible to decrease critical risks; thus, in this article appropriate responses are elicited from interview in three parts including, construction cost, time and quality. Totally, 10 risks are in critical conditions for which there are proper responses (Table 5).

Table 5. Responses to the risks

Critical risks	response
Exchange rate fluctuations and price changes	Deposit exchange in beginning of project Redesign of project according to exchange rate fluctuations Use of new supply resources
Error in initial project schedule	Regular Supervision and investigation of payments Supply of financial resources by banks mediation Investigation of different parts of organization to find ways for deposit
Increase in interest rates	Diversify the portfolio of companies Debt of settlement in short timeframes Select of sources with lower interest rates
International disputes in the field of water	Use of different suppliers from different countries Investments in upgrading technology and knowledge of suppliers Negotiation to resolve disputes
recession	Use of mediation to supply resources Saving liquidity for recession Expanding investment in different sectors Reducing extra costs
Weakness in personnel responsibility	Accurate coordination between different parts of the supply chain Learn from past events and delays Prevent unnecessary repetition of activities
Lack of resources to supply materials	Providing accurate daily reports of project trends Providing flexible scheduling Accurate investigation of activities relations
Shortage of sufficient supplier	Accurate estimation of required materials and services Use of different methods for distribution and shipping Considering alternative supply resources
Human error in design Incorrect	control and supervision of project Determination of the rules and regulations at each stage of the project Use of experts related to their responsibilities
Natural disasters	Collaboration with insurance companies to conclude contracts Construction of dams and increase of vegetation Pay attention to the predictions and early warning signs

4. Summary and Conclusions

In this study, 35 supply chain risks are identified from previous studies which 25 of them are chosen via Delphi method as a concrete dam construction supply chain risks. These risks are classified in three categories based on their source. Then, FMEA is applied to evaluate the importance of risks in three parts namely, construction cost, time and quality. In critical level, there are 10, 5 and 3 risks in construction cost, time and quality parts, respectively. In addition, the risks and impacts in each part of the supply chain can be extended to other sections, ultimately affecting the entire project. It should be noted that more attention to related risks of supply chain of dam construction and management can lead to better financial resources management. It also increases accuracy of time management, quality of construction, labor productivity and environmental friendliness.

References

1. Wong A (1999). Total quality management in the construction the construction industry in Hong Kong: A supply chain management perspective. Total Quality Management, 199-208.
2. Lavastre O, Gunasekaran A, Spalanzani A (2012). Supply chain risk management in French companies. Decision Support Systems, 828-838.
3. Abidin NAZ, Ingirige B (2018). Identification of the "Pathogenic" Effects of Disruptions to Supply. Procedia Engineering, 467-474.
4. Jüttner U (2005). Supply chain risk management. International Journal of Logistics Management, 120-141.
5. Vrijhoef R, Koskela L (2000). The four roles of supply chain management in construction. European Journal of Purchasing & Supply Management, 169-178.
6. Dallasega P, Rauch E, Linder C (2018). Industry 4.0 as an enabler of proximity for construction supply chains: A systematic literature review. Computers in Industry, 205-225.
7. Xue X, Wang Y, Shen Q, Yu X (2007). Coordination mechanisms for construction supply chain management in the Internet environment. International Journal of Project Management, 150-157.
8. Halil FM, Mohammed MF, Mahbub R, Shukur AS (2016). Trust Attributes to Supply Chain Partnering in Industrialised Building System. Procedia - Social and Behavioral Sciences, 46-55.
9. Ansar A, Flyvbjerg B, Budzier A, Lunn D (2014). Should we build more large dams? The actual costs of hydropower megaproject development. Energy Policy, 43-56.
10. Chen ZS, Zhou J, Zhu CY, Wang ZJ, Xiong SH, Rodríguez RM, Martínez L, Skibniewski MJ (2023). Prioritizing real estate enterprises based on credit risk assessment: an integrated multi-criteria group decision support framework. Financial Innovation, 9, 120.
11. Wang ZJ, Sun Y, Deveci M (2024). Smart Contract Application in Resisting Extreme Weather Risks for the Prefabricated Construction Supply Chain: Prototype Exploration and Assessment. Group Decision and Negotiation, 1049-1087.
12. Taleb NN (2007). The Black Swan: The Impact of the Highly Improbable. Random House.
13. Chanson H (2009). Embankment overtopping protections system and earth dam spillways. In W.P. Hayes, Dams: Impacts, Stability and Design pp. 101-132. NY: Nova Science Publishers.
14. Johnson ME (2001). Learning From Toys: Lessons in Managing Supply Chain Risk from the Toy Industry. California Management Review Reprint Series, 106-124.
15. Qaraqanabadi F, Sarkardeh H (2024). Identification and evaluation of supply chain risks in road construction projects. Structural and Construction Engineering (In Persian)
16. Wilson MC (2007). The impact of transportation disruptions on supply chain performance. Transportation Research Part E, 295-320.
17. Gaudenzi B, Borghesi A (2006). Managing risks in the supply chain using the AHP method. International Journal of Logistics Management, 114-136.
18. Tuncel G, Alpan G (2010). Risk assessment and management for supply chain networks: A case study. Computers in Industry, 250-259.
19. Giri BC, Bardhan S (2015). Coordinating a supply chain under uncertain demand and random yield in presence of supply disruption. International Journal of Production Research, 5070-5084.
20. Yang Y, Xu X (2015). Post-disaster grain supply chain resilience with government aid. Transportation Research Part E, 139-159
21. Nasser Alamri, O. A. (2017). Analysis Of Construction Delay Causes In Dams Project In Oman. European Journal of Business and Social Sciences, 19 - 42.
22. Blloku M, A. Ö. (2013). A case study of the delays of dam and channels construction in Albania. International Balkans Conference on Challenges of Civil Engineering, pp.23-25. Tirana.
23. Marietjir R. De Villiers, P. J. (2005). The Delphi technique in health sciences education research. Medical Teacher, 639-643.
24. Sinead Keeney, F. H. (2001). A critical review of the Delphi technique as a research

methodology for nursing. International Journal of Nursing Studies, 195-200.
25. Paul R. Kleindorfer, G. H. (2005). Managing Disruption Risks in Supply Chains. Production and Operations Management, 53-68.
26. Uta Jüttner, H. P. (2003). Supply chain risk management: outlining an agenda for future research. International Journal of Logistics Research and Applications, 197-210.
27. Stamatis DH (2003). Failure Mode and Effect Analysis: FMEA from Theory to Execution. ASQ Quality Press.
28. Kudláč S, V. Š. (2017). Using the Saaty Method and the FMEA Method for Evaluation of Constraints in Logistics Chain. Procedia Engineering, 749-755.
29. Ebrahemzadih M, G. H. (2014). Assessment and Risk Management of Potential Hazards by Failure Modes and Effect Analysis (FMEA) Method in Yazd Steel Complex. Open Journal of Safety Science and Technology, 127-135.
30. Katebi A, Mirzaahmadi M, Sarkardeh H (2020). Identification, classification, and evaluation of supply chain risks in concrete dams in terms of cost. Iranian Dam and Hydroelectric Powerplant 7 (26), 39-47 (In Persian).

© 2025 by the authors. Licensee SCU, Ahvaz, Iran. This article is an open access article distributed under the terms and conditions of the Creative Commons Attribution 4.0 International (CC BY 4.0 license) (http://creativecommons.org/licenses/by/4.0/).

Optimizing Minor Drainage Tunnel Position to Mitigate Groundwater Inflow in Main Tunnel Projects

Hadi Farhadian[*,1]

1. Department of Mining Engineering, Faculty of Engineering, University of Birjand, Birjand, Iran.

***Corresponding Author:**
Hadi Farhadian

Email: farhadian@birjand.ac.ir
Received: 2025.01.02
Accepted: 2025.01.30
J. Hydraul. Struct., 2025; 11(4):57-67
DOI: 10.22055/jhs.2025.48675.1334

ABSTRACT

Optimizing the positioning of minor drainage tunnels is a crucial strategy in mitigating groundwater inflow within main tunnel projects, a significant concern in civil engineering and infrastructure development. Groundwater inflow can lead to serious challenges, including tunnel instability, flooding, and increased construction costs. This makes effective management of water in underground projects paramount. The strategic placement of minor drainage tunnels facilitates the efficient collection and diversion of seepage water, reducing the risks associated with groundwater inflows. This study employs numerical finite element modeling to examine the optimal positioning of drainage tunnels relative to main tunnels, considering various configurations and hydrogeological conditions. Results indicate that placing the drainage tunnel below the main tunnel significantly reduces groundwater inflow, especially as tunnel radii and groundwater head levels increase. These findings provide a practical framework for enhancing tunnel drainage efficiency, ensuring structural stability, and minimizing environmental impacts by introducing the final model in optimizing minor drainage tunnel positions to mitigate groundwater inflow in main tunnel projects.

KEYWORDS
Tunnel, Drainage, water inflow, Numerical modeling.

1. Introduction

Tunneling is a critical aspect of civil engineering, particularly for infrastructure projects that require the construction of underground passages such as roadways, pipelines, and transit systems. One of the prominent challenges in tunnel construction is managing groundwater inflow, which can significantly impact both the safety and economic viability of tunnel projects. Groundwater inflows are often considered unpredictable geological hazards that can lead to instabilities in the surrounding rock formations, posing serious risks such as injuries, fatalities, and substantial financial losses [1–3]. The importance of understanding groundwater conditions cannot be overstated, as they play a decisive role in the design and operation of tunnels. Accurate prediction and evaluation of these inflows are paramount for effective tunnel drainage system design and for assessing the environmental impacts of associated drainage measures [1, 4, 5]. Despite the advances in methods proposed by researchers for estimating groundwater inflow, a comprehensive review of these methodologies remains absent in the current literature [1].

In addition to groundwater inflow, tunnel construction faces various operational challenges, such as the handling and transporting of materials in confined spaces. Limited access points complicate the delivery of essential construction materials and equipment, necessitating careful planning to ensure timely and safe operations [6]. Managing the varying geological conditions is another critical aspect of tunneling, as unexpected geological features can result in construction delays and increased costs. To mitigate these risks, thorough site investigations and ongoing monitoring during and after the excavation process are essential [7–9]. Groundwater management systems, including dewatering pumps and drainage strategies, play a crucial role in controlling water-related challenges and ensuring the stability of tunnel structures [6, 9].

The positioning of minor drainage tunnels plays a critical role in managing groundwater inflows and ensuring the stability of main tunnel projects. An effective drainage system is vital for mitigating the risks associated with groundwater, which can lead to tunnel instability, flooding, and significant construction delays [4].

Correctly locating minor drainage tunnels helps in efficiently collecting and redirecting seepage water from the surrounding rock and soil strata. This is particularly important in urban tunneling projects where unexpected high-water inflows can compromise the structural integrity of both the tunnel face and surface structures above [4]. An accurate characterization of subsurface conditions and hydrological modeling is essential to predict potential inflow points and design the drainage systems accordingly [4, 10].

Mitigating groundwater inflow in main tunnel projects is critical for maintaining tunnel stability and operational efficiency. A variety of strategies can be employed to address this issue, ensuring that water management is integrated into the planning and design phases. Effective drainage systems are essential for controlling groundwater levels. Comprehensive drainage plans should be developed to efficiently divert water away from the tunnel site, incorporating features such as detention ponds and swales to manage excess water during heavy rainfall events [11]. The strategic positioning of minor drainage tunnels can enhance the overall drainage efficiency and help in the timely removal of infiltrating water. Excavated water can be reused for various purposes, such as surface dust control or aquifer recharge, which not only minimizes water wastage but also mitigates the impacts of water inflow on the main tunnel [12]. These standards advocate for comprehensive environmental impact assessments that consider water quality and the potential impacts of groundwater extraction and inflow on local ecosystems. Integrating digital monitoring systems equipped with smart sensors allows for real-time tracking of groundwater levels, water quality, and tunnel structural health [13]. By continuously monitoring these parameters, engineers can make informed decisions to mitigate groundwater inflow and address issues before they escalate. By implementing these mitigation strategies, engineers can significantly reduce the risks associated with groundwater inflow, contributing to the safety and sustainability of tunnel projects. Tunneling projects face a myriad of challenges and difficulties that can significantly impact their execution and safety. In addition to the geological and hydrological, financial considerations also pose difficulties. Securing funding and navigating bureaucratic processes for approvals and permits are crucial stages that can slow down progress. Financial planning must address the extensive costs associated with tunnel construction, and delays in securing necessary approvals can disrupt project timelines significantly [6]. The design and maintenance of tunnel systems also require rigorous attention. Insufficient or improper maintenance can lead to major

dysfunctions, threatening the tunnel's operational capabilities and user safety. Thus, prioritizing the quality and durability of equipment is vital to minimizing the need for frequent maintenance interventions, which can be complicated by ongoing traffic conditions [14]. Few studies have explored the impact of the minor tunnel's position relative to the main tunnel on reducing groundwater inflow. The study of Lin et al. identified that placing a secondary (minor) tunnel beneath the primary (main) tunnel is the most effective configuration for minimizing water inflow. This arrangement achieves greater groundwater flow reduction compared to other placements, such as positioning the minor tunnel below but offset from the main tunnel. However, the effectiveness diminishes as the distance between the two tunnels increases, highlighting the importance of closer positioning [15]. Therefore, this study aims to determine the optimal location for the drainage tunnel (minor tunnel) relative to the main tunnel to effectively reduce groundwater inflow. To achieve this, a parametric study was conducted using numerical finite element modeling.

2. Numerical modeling

Numerical modeling and simulation techniques have become valuable tools for predicting groundwater behavior in the vicinity of tunnels. By creating detailed models that account for varying hydrogeological conditions, engineers can identify the most effective locations for minor drainage tunnels, thus minimizing the risk of groundwater inflows and optimizing the overall design [4]. Various methods, including analytical and empirical approaches, provide insights into inflow rates and inform decision-making in tunnel design and construction [4, 16, 17].

Over the past few decades, various numerical methods have been developed for predicting water flow into tunnels, including both continuum and discontinuous media approaches. In addition to the commonly used methods such as Continuum-Based Methods and Discontinuum-Based Methods. In continuum media typically used Finite Difference Method (FDM), Finite Element Method (FEM), Finite Volume Method (FVM), and Boundary Element Method (BEM). FDM is efficient and straightforward for solving groundwater flow equations on structured grids. However, its limitations in handling complex geometries and heterogeneous materials led us to explore more flexible approaches. FEM is well-suited for modeling irregular tunnel shapes and varying permeability distributions, making it a preferred choice for complex geological conditions. FVM is particularly advantageous because it ensures local mass conservation, which is crucial for accurately estimating water inflow in tunnel environments. BEM is effective for problems with infinite or semi-infinite domains, such as groundwater flow in unbounded media. However, its application is more suitable for simplified cases due to its reliance on boundary-only discretization. Also, in discontinuous media frequently used Discrete Element Method (DEM), Discontinuous Deformation Analysis (DDA), and Bonded Particle Method (BPM). DEM is useful for modeling fractured rock masses and discontinuous media, which can significantly influence water inflow patterns. However, it is computationally intensive for large-scale simulations. DDA is specifically designed for blocky rock masses and is effective in capturing deformation and fluid interactions within jointed rock formations. BPM is beneficial for simulating the mechanical and hydraulic behavior of fractured rock masses at a particle scale. It provides detailed insights into permeability changes due to rock fragmentation and deformation. [18–24]. Several innovative methods such as Hybrid Continuum/Discontinuum Approaches [25, 26] and Stochastic Analysis [27] have emerged that enhance the accuracy and efficiency of these predictions.

Numerical solutions play a crucial role in predicting groundwater inflow into tunnels under complex geotechnical and hydrogeological conditions. Several commercial software programs have been developed over the past decades based on FEM and DEM to analyze groundwater flow in rock masses, both in steady-state and transient regimes. Examples of such software include SEEP/W, FLAC, and UDEC for both 2D and 3D models. This study employs the finite element commercial code SEEP/W-V8.15.1.11236 to predict steady-state groundwater inflow into the main tunnel. The SEEP/W 2D model is capable of simulating various flow conditions, including saturated and unsaturated states in confined or unconfined aquifers. It takes into account the hydraulic conductivity and volumetric water content as functions of pore water pressure. This model has been widely applied to address geological and geotechnical challenges by simulating related hydrogeological issues [3, 21, 28–32]

The governing partial differential equation for two-dimensional saturated/unsaturated groundwater flow is derived by coupling the continuity equation with Darcy's law:

$$\frac{\partial}{\partial x}\left(K_x \frac{\partial h}{\partial x}\right) + \frac{\partial}{\partial y}\left(K_y \frac{\partial h}{\partial y}\right) = C\frac{\partial}{\partial t}(h) + Q \quad (1)$$

Here, K_x and K_y are the hydraulic conductivities in the x and y directions, respectively. Q represents the recharge or discharge per unit volume, h denotes the hydraulic head, t is time, and C is the slope of the water storage curve. The hydraulic head is related to volumetric water content (θ) by the following equation ([33]:

$$\frac{\partial \theta}{\partial t} = C\frac{\partial h}{\partial t} \quad (1)$$

The Galerkin approach has been utilized in SEEP/W 2D to solve this two-dimensional flow equation.

3. Analyses and discussion

In this study, to investigate the optimization of the drainage tunnel (minor tunnel) relative to the main tunnel, the water inflow to the tunnel was evaluated at five different positions of the secondary tunnel relative to the main tunnel. Since the numerical model used for the simulation is symmetrical, the five considered positions for the minor tunnel relative to the main tunnel were located at the upper, upper-right, right, lower-right, and lower sections (Figure 1). To analyze these positions, a finite element method was applied, with a numerical model of optimized dimensions of 100 by 50 meters and a square mesh grid. Detailed explanations of the methodology used to determine model dimensions and conduct sensitivity analyses can be found in previous studies [22, 23, 31]. The permeability coefficient was assumed to be 1×10^{-8} (m/s), the radius of the main tunnel was 2.5 meters, and the radius of the minor tunnel was 0.5 meters. Additionally, the water level above the tunnel center varied from 5 meters to 100 meters. It should be noted that the permeability coefficient is a crucial parameter in determining the inflow rate of water into the tunnel. Specifically, an increase or decrease in permeability directly leads to a corresponding increase or decrease in water inflow, indicating a fully proportional relationship. For instance, a tenfold increase or decrease in permeability, while keeping other parameters constant (such as water head, tunnel radius, and model dimensions), results in a tenfold increase or decrease in water inflow, respectively. Therefore, the overall trend of inflow remains consistent. Since the primary objective of this study is to identify a general trend for determining the optimal distance between the minor tunnel and the main tunnel, a permeability coefficient of 1×10^{-8} (m/s) was assumed as a default value. Figure 2 shows an example of the tunnel's position at the upper-right and lower sections, along with flow contours

and potential lines. Preliminary examinations of these five positions reveal that the minor tunnel, when excavated as a drainage tunnel at the lower part of the main tunnel, experiences the lowest water inflow across different groundwater head conditions (Figure 3). This finding provides initial confirmation of Lin et al.'s study [15], which investigated various positions for drainage tunnels relative to the main tunnel.

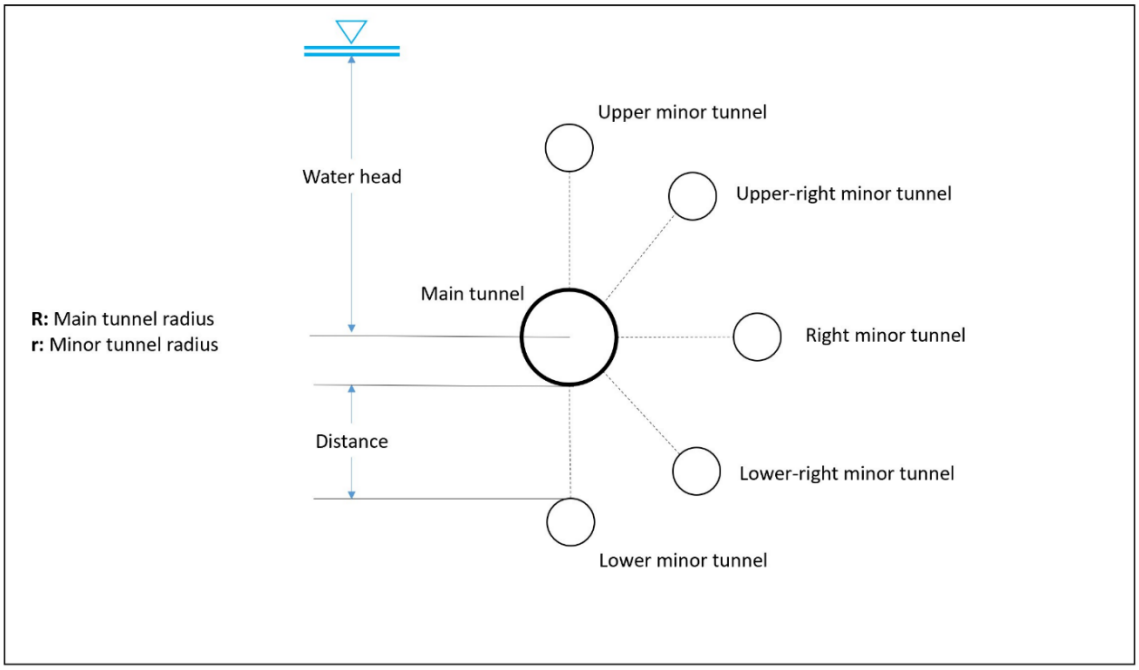


Figure 1. Schematic model of the positions of the drainage tunnels (minor) relative to the main tunnel.

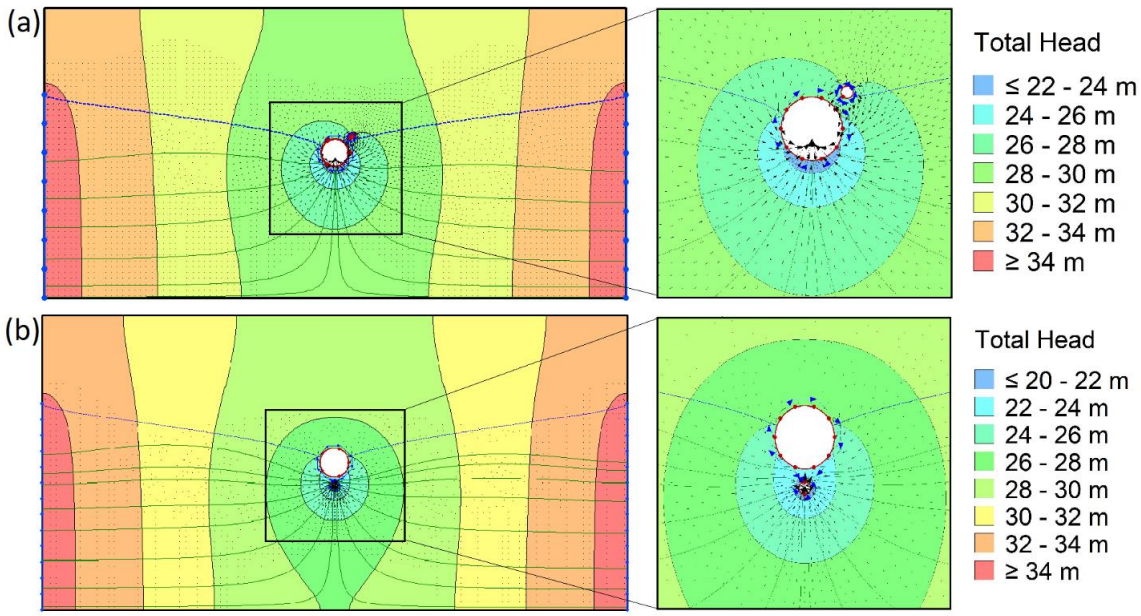


Figure 2. Simulated model of water inflow into the tunnel along with contour display of potential lines and streamlines, H: 10 m, permeability coefficient: 1×10^{-8} m/s, and tunnels distance: 1 m, R: 2.5 m, r: 0.5 m, a) Simulated model for the upper-right tunnel, b) Simulated model for the lower tunnel.

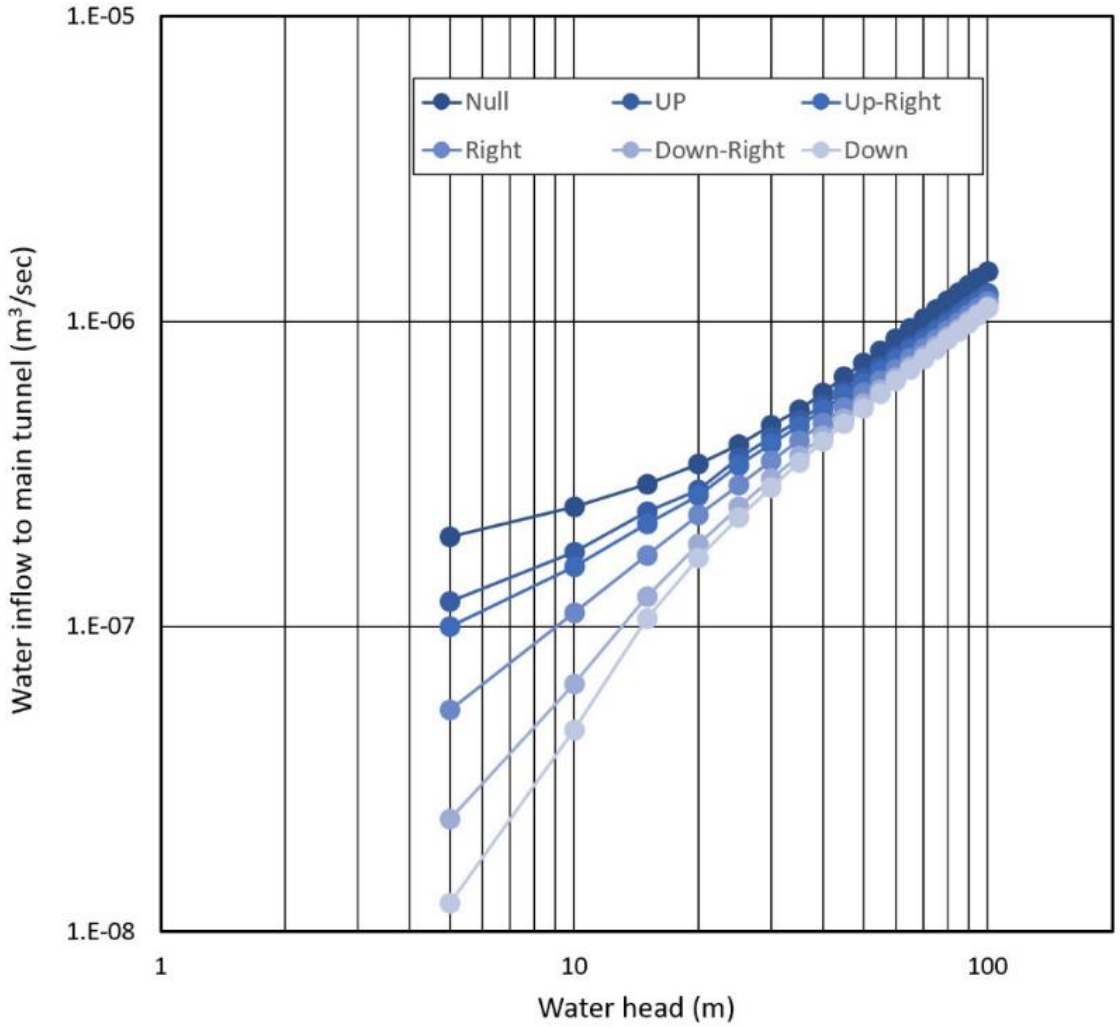


Figure 3. Inflow of water to the main tunnel concerning different groundwater head levels at various positions of the minor tunnel (Null: when the minor tunnel is not excavated).

In the next step, based on the results which indicated that the position of the lower tunnel relative to the main tunnel has the lowest water inflow to the tunnel, the water inflow rate for different water head levels was calculated considering various radii of the main tunnel and a fixed radius of the minor tunnel (0.5 meters) (Figure 4). As shown in this figure, it is expected that with the increase in tunnel radius, the water inflow to the tunnel increases as well. Additionally, as the water head above the tunnel increases, the water inflow to the tunnel also increases. However, it is important to note that as the water head increases, the water inflow to the tunnel tends to stabilize at nearly a constant value at higher waterheads (100 meters of water head and above).

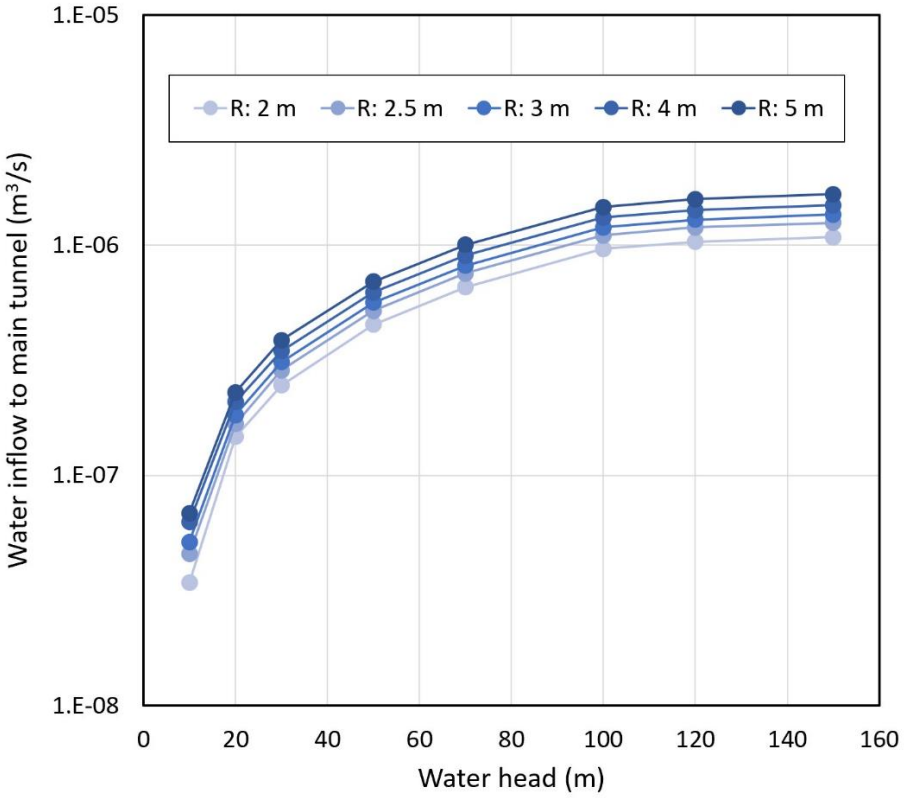


Figure 4. Inflow of water to the main tunnel concerning different groundwater head levels in various scenarios of the main tunnel radius (the minor tunnel is excavated below the main tunnel)

To achieve the desired outcome and determine the optimal distance between the drainage tunnel (minor tunnel) and the main tunnel, various scenarios were examined. In these scenarios, the position of the drainage tunnel relative to the main tunnel was considered at the lower section of the tunnel with a fixed radius of 0.5 meters. The radius of the main tunnel was set at 0.5, 1, 1.5, 2, 2.5, 3, 3.5, 4, 4.5, and 5 meters, with groundwater levels of 20, 50, and 100 meters, and varying distances between the main tunnel and the minor tunnel from 1 to 15 meters, with a step size of 1 meter. Additionally, a permeability coefficient of 1e-7 meters per second was used. As a result, 450 different numerical models were simulated.

Figure 5 shows the water inflow to the tunnel for different distances between the drainage tunnel and the major tunnel, considering various radii of the main tunnel and different water head levels. As seen in Figure 5a, the main tunnel is located 20 meters below the groundwater surface. As the distance between the tunnels increases, the water inflow into the main tunnel decreases. The rate of decrease in water inflow to the tunnel becomes more noticeable in tunnels with larger radii as the distance between the tunnels increases. In other words, as the distance between the tunnels increases, the water inflow to the tunnel will stabilize at a constant value after a certain distance (the threshold distance), beyond which the reduction in water inflow to the tunnel will be less than 5%. This threshold distance is marked with a dashed red line. Similarly, this behavior occurs for different water head levels of 50 meters and 100 meters (Figures 5b, 5c), with the distinction that when the main tunnel is deeper relative to the groundwater surface (at a water head of 100 meters), the water inflow to the tunnel reaches a constant value more quickly as the distance between the tunnels (minor tunnel and main tunnel) increases.

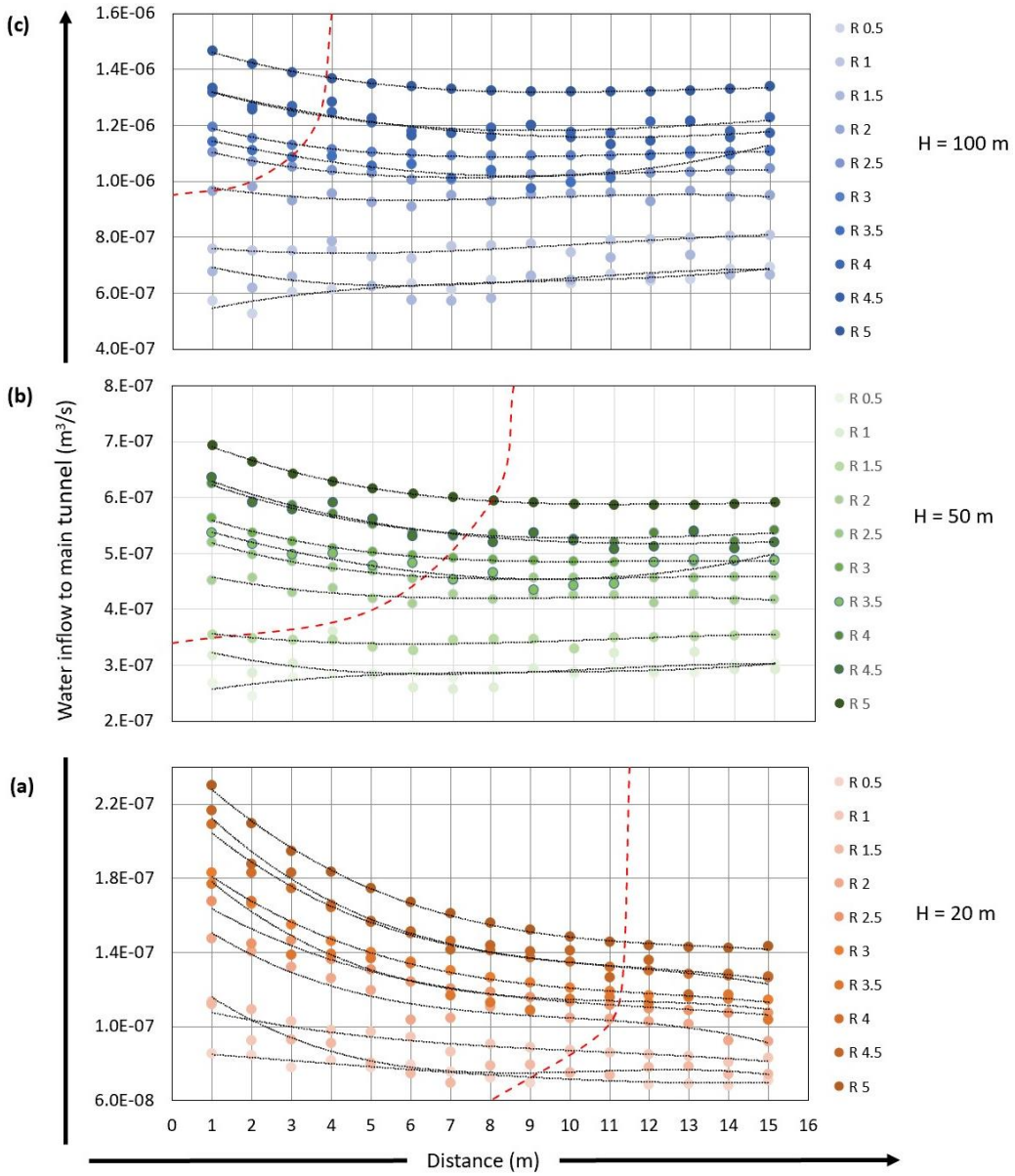


Figure 5: The inflow of water to the main tunnel relative to the different distances of the minor tunnel from the main tunnel at various main tunnel radius and different water head levels.

To present a final model, based on various groundwater head levels (the depth of the main tunnel relative to the groundwater surface), different radii of the main tunnel, and varying distances between the tunnels (main tunnel and lower sub-tunnel), Figure 6 is proposed as the final model to determine the optimal distance for reducing water inflow to the main tunnel, considering a radius of 0.5 meters at the minor tunnel. For this purpose, boundary lines for different water head levels of 20, 50, and 100 meters were initially implemented in the general diagram showing water inflow to the tunnel relative to varying distances (represented by red lines). Then, using interpolation, contour lines for the 30, 40, 60, 70, 80, and 90-meter levels were drawn. Using this figure, the optimal distance of the drainage tunnel (minor lower tunnel) relative to the main tunnel can be determined based on the radius of the main tunnel and the water head.

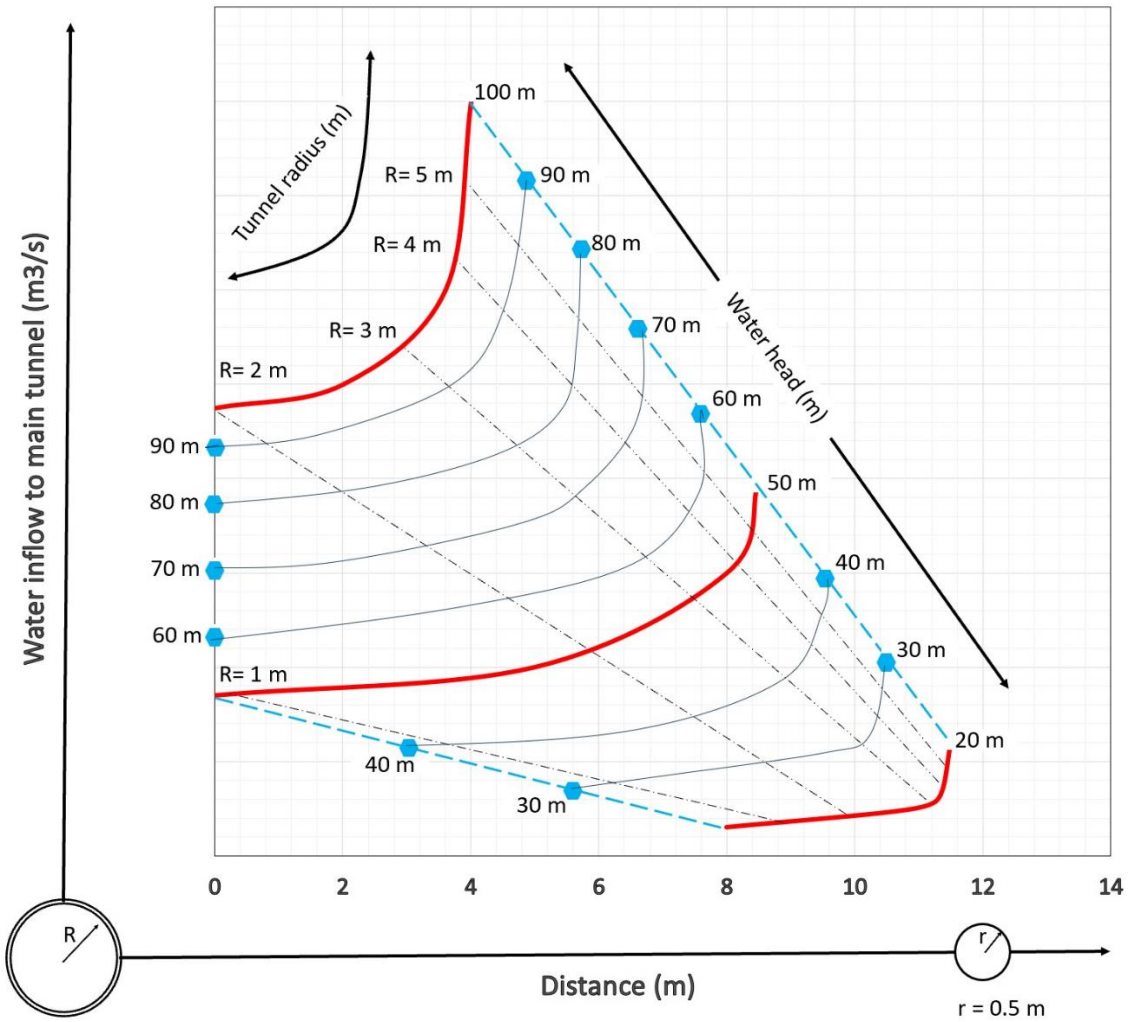


Figure 6: The final model to obtain the optimal distance of the drainage tunnel (lower minor tunnel) relative to the main tunnel based on the radius of the main tunnel and the underground water head levels.

4. Conclusion

The study confirms that the strategic positioning of drainage tunnels is vital in addressing groundwater inflow challenges in tunnel projects. Numerical simulations revealed that the optimal location for the minor drainage tunnel is below the main tunnel, where inflow rates were significantly reduced. Additionally, as the groundwater head and main tunnel radius increase, this configuration becomes even more effective. Key insights include:

1. Water Inflow Dynamics: As the distance between the drainage and main tunnels increases, water inflow stabilizes beyond a certain threshold, which varies with tunnel dimensions and groundwater levels.
2. Optimal Design Parameters: The optimal distance between the drainage and main tunnels was identified (Figure 6), providing practical guidelines for engineers. This ensures minimal inflow rates without excessive excavation.
3. Environmental and Sustainability Considerations: Integrating the findings with sustainable water management practices—such as reusing excavated water for environmental restoration—can significantly reduce the ecological footprint of tunnel construction.

This research bridges the gap between theoretical modeling and practical

application, offering a robust framework for engineers to design safer and more efficient tunnel drainage systems. By adopting these strategies, projects can achieve improved cost-effectiveness, structural integrity, and environmental sustainability.

Reference

1. Dematteis A, Torri R, Looser M (2007) Water Resources Management in Tunneling: insights in the decision-making process to improve tunnels environmental sustainability. Proc. XXXV IAH Congress, Groundwater and Ecosystems, Lisbon
2. Vincenzi V, Piccinini L, Gargini A, Sapigni M (2010) Parametric and numerical modelling tools to forecast hydrogeological impacts of a tunnel. Aqua Mundi 1:135–154
3. Maleki Z, Farhadian H, Nikvar-Hassani A (2020) Geological hazards in tunnelling: The example of gelas water conveyance tunnel, iran. Quarterly Journal of Engineering Geology and Hydrogeology. https://doi.org/10.1144/qjegh2019-114
4. Frenelus W, Peng H, Zhang J (2021) Evaluation methods for groundwater inflows into rock tunnels: a state-of-the-art review. International Journal of Hydrology 5:152–168
5. Farhadian H, Eslaminezhad SA (2022) Estimation of Groundwater Seepage Risks into Tunnel Using Radial Basis Function Networks. Journal of Irrigation Sciences and Engineering 45(2):109-124
6. Swannell NG, Greig TRM, Belhomme F, Bamforth A (2001) Forming a new route for drainage. Tunnels & Tunnelling International 33:
7. Farhadian H (2021) A new empirical chart for rockburst analysis in tunnelling: Tunnel rockburst classification (TRC). Int J Min Sci Technol
8. Farhadian H, Nikvar-Hassani A (2020) Development of a New Empirical Method to Tunnel Squeezing Classification (TSC). Quarterly Journal of Engineering Geology and Hydrogeology
9. Hlad C (2011) Sustainable Design Strategies for Tunneling Projects. Underground Construction 66:20
10. Farhadian H, Nikvar-Hassani A (2019) Water flow into tunnels in discontinuous rock: a short critical review of the analytical solution of the art. Bulletin of Engineering Geology and the Environment. https://doi.org/10.1007/s10064-018-1348-9
11. Cashman PM, Preene M (2020) Groundwater Control for Tunnelling Projects. In: Groundwater Lowering in Construction. CRC Press, pp 233–288
12. Vvedenskij R V, Gendler SG, Titova TS (2018) Environmental impact of the tunnel construction. Magazine of Civil Engineering 141–150
13. Marinos V (2020) Engineering Geology and Tunnels. Tunnel Engineering-Selected Topics
14. Chen Z, Su Z, Li M, Shen Q, Fan L, Zhang Y (2024) Investigation of the Tunnel Water Inflow Prediction Method Based on the MODFLOW-DRAIN Module. Water (Basel) 16:1078
15. Lin B, Lee C, Yu J (2000) Analysis of groundwater seepage of tunnels in fractured rock. Journal of the Chinese institute of Engineers 23:155–160
16. Katibeh H, Aalianvari A (2012) Common Approximations to the water inflow into Tunnels. Drainage systems 75–88
17. Anvari AA, Katibeh H, Sharifzadeh M, Farhadian H (2010) Estimation of fault zone permeability with fuzzy-delphi AHP (FDAHP) method. Rock Mechanics in Civil and Environmental Engineering - Proceedings of the European Rock Mechanics Symposium, EUROCK 2010
18. Bobet A (2010) NUMERICAL METHODS IN GEOMECHANICS. Arabian Journal for Science & Engineering (Springer Science & Business Media BV) 35:
19. Jing L, Hudson JA (2002) Numerical methods in rock mechanics. International Journal of Rock Mechanics and Mining Sciences 39:409–427

20. Jing L (2003) A review of techniques, advances and outstanding issues in numerical modelling for rock mechanics and rock engineering. International Journal of Rock Mechanics and Mining Sciences 40:283–353
21. Moeini H, Farhadian H, Nikvar-Hassani A (2018) Determination of the optimum sealing method for Azad pumped storage dam considering seepage analysis. Arabian Journal of Geosciences 11:1–13
22. Farhadian H, Salehzadeh MH, Nikvar-Hassani A (2021) Model dimension effect in DEM and FEM simulations for assessment of water inflow into a tunnel. In: ARMA US Rock Mechanics/Geomechanics Symposium. ARMA, p ARMA-2021
23. Nikvar Hassani A, Katibeh H, Farhadian H (2015) Numerical analysis of steady-state groundwater inflow into Tabriz line 2 metro tunnel, northwestern Iran, with special consideration of model dimensions. Bulletin of Engineering Geology and the Environment. https://doi.org/10.1007/s10064-015-0802-1
24. Farhadian H, Maleki Z, Eslaminezhad SA (2021) Assessment of the Optimum Depth of Sealing Cutoff Walls in the Clay Core of Peygham-Chay Dam. Journal of Hydraulic Structures 7:59–76
25. Hokr M, Škarydová I, Frydrych D (2012) Modelling of tunnel inflow with combination of discrete fractures and continuum. Comput Vis Sci 15:21–28
26. Jahanmirir S, Aalianvari A, Ebrahimpour-Komleh H (2024) Optimizing Groundwater Seepage Prediction in Tunnels Using the Human Mental Search (HMS) Algorithm: A Cognitive-Inspired Approach to Complex Geotechnical Challenges. Journal of Mining and Environment
27. López-Acosta NP (2016) Numerical and analytical methods for the analysis of flow of water through soils and earth structures. Groundwater-Contaminant and Resource Management
28. Farhadian H, Aalianvari A, Katibeh H (2012) Optimization of analytical equations of groundwater seepage into tunnels: A case study of Amirkabir tunnel. Journal of the Geological Society of India. https://doi.org/10.1007/s12594-012-0122-z
29. Aryafar A, Doulati Ardejani F, Singh RN (2009) Numerical modeling of groundwater inflow from a confined aquifer into Sangan open pit mine, northeast Iran. Geomechanics and Geoengineering: An International Journal 4:189–199
30. Farhadian H, Bahmani Shahraki F (2024) Enhancing analytical methods for estimating water inflow to tunnels in the presence of discontinuity areas. Environ Earth Sci 83:339
31. Farhadian H, Hassani AN, Katibeh H (2016) Groundwater inflow assessment to Karaj Water Conveyance tunnel, northern Iran. KSCE Journal of Civil Engineering. https://doi.org/10.1007/s12205-016-0995-2
32. Butscher C, Scheidler S, Farhadian H, Dresmann H, Huggenberger P (2017) Swelling potential of clay-sulfate rocks in tunneling in complex geological settings and impact of hydraulic measures assessed by 3D groundwater modeling. Eng Geol. https://doi.org/10.1016/j.enggeo.2017.03.010
33. Farhadian H, Gholami Z (2024) Hydraulic Response to Geometry: Finite Element Modeling of Underground Spaces in Saturated Environments. Journal of Hydraulic Structures 10:66–79



© 2025 by the authors. Licensee SCU, Ahvaz, Iran. This article is an open access article distributed under the terms and conditions of the Creative Commons Attribution 4.0 International (CC BY 4.0 license) (http://creativecommons.org/licenses/by/4.0/).

An Experiment on the Effect of Sills with Orifices Under a Sluice Gate on Energy Dissipation and Hydraulic Jump

Rasoul Daneshfaraz [1],Reza Norouzi [1],Behnaz Akhondi [1], Mehdi Djahanghiri [2]

1. Department of Civil Engineering, Faculty of Engineering, University of Maragheh, Maragheh, East Azerbaijan Iran.
2. Department of Mathematics, Faculty of Basic Sciences, University of Maragheh, Maragheh, Iran.

***Corresponding Author:**
Rasoul Daneshfaraz,

Email: daneshfaraz@maragheh.ac.ir
Received: 2025.02.10
Accepted: 2025.04.23
J. Hydraul. Struct., 11(4): 68-78
DOI: 10.22055/jhs.2025.48970.1336

ABSTRACT

In the present study, sills with orifices were utilized to enhance energy dissipation downstream of these structures. For this purpose, a sill with the same width as the channel, a fixed height, and 1 to 4 perforations with a constant diameter of 2 centimeters was experimentally investigated. The results indicated that in the presence of the sill, the specific energy and Froude number downstream of the gate decreased by an average of more than 13% across all models. The introduction of sills and the increase in their number in the orifice led to increased turbulence in the flow, resulting in a reduction in specific energy downstream of the gate. A quantitative analysis of specific energy downstream of the gate reveals that orifice sills, configured with 1, 2, 3, and 4 orifices, reduce particular energy employing 29%, 32%, 40%, and 48%, respectively, relative to a non-orifice sill. Furthermore, the non-orifice sill achieves a 14% reduction in specific energy compared to the baseline non-sill condition. Furthermore, the analysis of depth ratios and energy dissipation in hydraulic jumps revealed that the sill with 4 orifices sill the lowest depth ratio of the jump, while a decrease in the number of orifices increased the contribution of the hydraulic jump to the energy dissipation of the flow.

KEYWORDS
Energy Dissipation, Hydraulic Jump, Vertical Gate, Sill With Orifice.

1. Introduction

Sluice gates are one of the essential structures for controlling water flow in channels, dams, ports, basins, water reservoirs, and various irrigation and desalination structures. These structures are categorized differently based on their location and intended use. One of the most commonly used types of these structures is the sluice gate [1]. Downstream of the gates, the flow is supercritical and possesses destructive kinetic energy; therefore, it is necessary to implement measures to dissipate this energy. Such measures may include the use of sill upstream, downstream, and even beneath the gate, the use of blocks against supercritical flow, and the implementation of rough beds to prevent cavitation phenomena [2]. Numerous studies have been conducted on energy dissipation downstream of gates, and a brief overview of some of these studies is presented below.

The study investigated hydraulic jumps over a rough bed downstream of a gate and demonstrated that bed shear stress is dependent on the flow Froude number. Additionally, the characteristics of the hydraulic jump are influenced by shear stress and relative roughness[3]. Showed that using strip roughness reduces the length and depth of hydraulic jumps over a rough bed[4]. Experimentally investigated the effect of a wavy bed with relative roughness ranging from 0.19 to 0.324 and a Froude number range of 4 to 12 on the characteristics of hydraulic jumps. The results indicated that the wavy bed reduces the conjugate depth and length of the jump by approximately 20% and 35%, respectively[5]. A numerical simulation using four turbulence models for a vertical gate demonstrated that the turbulence model affects the contraction section and the calculation of the contraction coefficient. The results showed that T-shaped elements with a density percentage of 8 provided more favorable results compared to rectangular elements with a density percentage of 10[6]. Investigated energy dissipation in a vertical gate within a sloped channel. Their results showed that as the bed slope and relative opening height of the gate increased, energy dissipation decreased[7]. Experimentally investigated energy dissipation in a vertical gate with a prismatic sill. They showed that the prismatic sill located beneath the gate increases the flow energy dissipation by 10%[8]. Abdulmonem et al., (2018), used a pendulum sill to investigate the characteristics of hydraulic jumps. Their results indicated that the implementation of the pendulum sill increases the efficiency of the hydraulic jump by 20%[9]. Created an orifice in the vertical gate to experimentally examine the characteristics of the hydraulic jump downstream. Their results showed that the introduction of an orifice in the vertical gate increases the energy dissipation of the hydraulic jump[10]. Conducted an experimental study on energy dissipation of hydraulic jumps in a sluice gate within a channel with a reverse slope. Their study results showed that an increase in slope leads to greater energy dissipation[11]. Demonstrated that the characteristics of the formed hydraulic jump improve by creating a sudden opening downstream of the gate. Additionally, [12] demonstrated that sill with various geometric shapes placed beneath the gate resulted in the greatest depth downstream when using circular sills. Investigated experimentally the effect of gate opening and the presence of a sill with different widths on energy dissipation under free flow conditions. The results showed that in the case without a sill and at various openings, the relative energy loss has an inverse relationship with the gate opening. On average, at an opening of 2 centimeters, the energy loss compared to upstream and downstream is 67.47% and 47.71% greater than that at a 4-centimeter opening, respectively. Based on the experimental results, the relative energy loss in the presence of a sill is greater than in the case without a sill for all widths. Furthermore, as the width of the sill increases and consequently the total opening decreases, the relative energy loss increases compared to sills with smaller widths[13].

As discussed in the literature review, hydraulic jumps are commonly used to dissipate energy downstream of sluice gates. Various strategies have been employed to improve the characteristics of hydraulic jumps in stilling basins. Since energy dissipation increases due to increased turbulence and shear forces on the bed, it is necessary to utilize appropriate methods to enhance energy dissipation while also protecting the channel bed. In this study, in order to improve the efficiency of vertical gates in energy dissipation downstream, for the first time, channel-width-aligned sills with fixed-diameter orifices placed at different numbers and symmetrically spaced transversely beneath the gate have been utilized.

2. Materials and Methods

2.1. Dimensional Analysis

Considering Figure 1, the parameters influencing energy dissipation downstream of the sluice gate equipped with an orifice sill are expressed as equation (1):

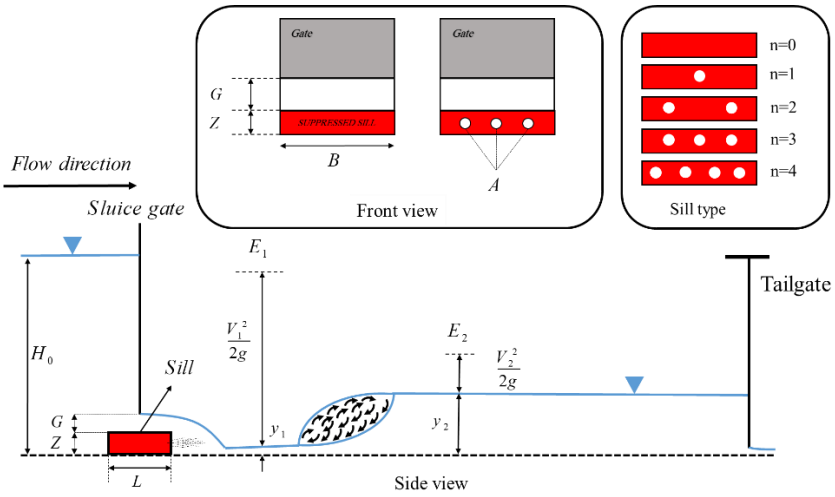


Figure 1. Schematic of flow in a sluice gate with an orifice sill

$$\Delta E = f_1(q.\mu.\rho.n.A.Z.B.g.G.\sigma.y_1.y_2) \quad (1)$$

In the above equation, ΔE represents the energy loss between sections 1 and 2, (L) denotes the length, q is the unit discharge (L^3T^{-1}), is the dynamic viscosity of water ($ML^{-1}T^{-1}$), Specific gravity of water (ML^{-3}), n refers to the number of orifices (dimensionless), A is the cross-sectional area of the orifice (L^2), Z is the height of the threshold (L), B is the length of the sill or width of the channel (L), g is the acceleration due to gravity (LT^{-2}), G is the height of the gate opening (L), σ is the surface tensionof water (ML^{-2}), y_1 is water depth upstream the jump, and y_2 is the water depth downstream the hydraulic jump (L). According to the Buckingham theorem and considering y_1, q, and μ as repeating variables, the dimensionless parameters are presented as equation (2).

$$\frac{\Delta E}{y_1} = f_2(n.\frac{q^2}{y_1^3 g}.\frac{\rho q}{\mu}.\frac{A}{y_1^2}.\frac{Z}{y_1}.\frac{B}{y_1}.\frac{G}{y_1}.\frac{q\sigma}{y_1\mu}.\frac{y_2}{y_1}) \quad (2)$$

In the above equation, Fr_1 is the Froude number of the flow before the hydraulic jump, *Re* is the Reynolds number, and *We* is the Weber number. Given that the cross-sectional area of the orifice, channel width, and height of the threshold are constant, the expressions B/y_1 and Z/y_1 can be disregarded. Finally, by performing these simplifications, equation (3) is simplified as follows:

$$\frac{\Delta E}{y_1} = f_3(Fr_1.Re.n.We.\frac{G}{y_1}.\frac{y_2}{y_1}) \quad (3)$$

Considering that the flow is turbulent, the Reynolds number and Weber number can be disregarded (Raju, 1984, and Loria et al., 2020), and equation (3) can be expressed as equation (4):

$$\frac{\Delta E}{y_1} = f_4(Fr_1.n.\frac{G}{y_1}.\frac{y_2}{y_1}) \quad (4)$$

In equation (4), the relative energy dissipation between sections 1 and 2 is

represented and is usually expressed as ΔE. Therefore, energy dissipation can be written as a function of other parameters:

$$\frac{\Delta E}{E_1} = f_5(Fr_1.n.\frac{y_2}{y_1}.\frac{G}{y_1}) \quad (5)$$

Considering that in the above equation, the Froude number and the ratio of depths of the hydraulic jump depend on the upstream flow characteristics, particularly the geometric characteristics of the threshold, equation (5) is simplified as follows:

$$\frac{\Delta E}{E_1} = f_6(Fr_1.n.\frac{G}{y_1}) \quad (6)$$

$$\frac{y_2}{y_1} = f_7(Fr_1.n.\frac{G}{y_1}) \quad (7)$$

2.2. Experimental setup

A rectangular flume with a horizontal bottom slope was used for experiments, measuring 5 meters in length, 0.325 meters in width, and 0.45 meters in height [14, 15]. The walls are made of tempered glass, and the bottom is made of steel. This flume is equipped with a storage tank where water is pumped in by two pumps. After traveling the length of the flume (5 meters), the water is returned to the storage tank in a circular manner from the end of the flume. A vertical gate made of polyethylene with a sharp edge was selected, with an opening height of 2 and 3 centimeters. The length of the tank behind the gate was considered to be one meter.

The sills made of polyethylene have dimensions of length, width, and height of 3cm, 0.325 m, and 4cm, respectively. They were constructed with 1, 2, 3, and 4 gate openings, each with a diameter of 2cm. The arrangement of the sill with orifice was such that they were positioned symmetrically along the width. To create a tailwater depth and form a hydraulic jump downstream of the flume, a sluice gate was used. After installing the sluice gate and sill, the pump was turned on and then adjusted using a rotameter with an accuracy of ±2. Once the flow conditions stabilized, which took some time, the tailwater depth was adjusted so that the jump toe remained fixed at a specific location and the flow conditions over the sluice gate were free [16]. With the stabilization of the hydraulic jump toe, the initial and secondary jump depths were measured using a point depth gauge with an accuracy of one millimeter. To reduce device error and human error, data collection was performed at several points across a cross-section.



a) The flow and hydraulic jump state of an orifice with a constant flow rate of 650 liters per minute.



b) The hydraulic flow and jump in the two-orifice condition with a constant flow rate of 650 liters per minute.



c) Hydraulic flow and jump in a three-orifice configuration with a constant discharge of 650 liters per minute in top view.



d) Hydraulic flow and jump in a three-orifice configuration with a constant discharge of 650 liters per minute in front view



e) Hydraulic jump and flow in the four-orifice state with a constant flow rate of 650 liters per minute.

Figure 2. The hydraulic jump formed under the laboratory conditions of the current research

3. Results and Discussion

In Figure 3, the relationship between flow rate (Q) and dimensionless height (H/G) behind the gate was analyzed. The results show a clear upward trend in water height with increasing flow rate. As the flow rate increases, the height behind the gate rises, demonstrating the direct impact of discharge on water levels in the system. This is consistent with the expectations of hydraulic flow dynamics, where higher flow rates typically result in greater water depths due to the increased energy in the system.

Furthermore, this behavior aligns with findings from previous research. In various studies, similar trends have been observed, where higher flow rates lead to an increase in water depth behind sluice gates or weirs. These results support the general understanding in fluid mechanics that flow rate is a key determinant in controlling water depth, especially in systems where flow is regulated by gates or barriers.

By comparing the data obtained in this study with previous works, it is evident that the trends are consistent across different experimental setups. The relationship between discharge and water depth observed here supports the conclusions drawn in earlier studies, reinforcing the validity and reliability of the current findings. Therefore, this study contributes to the existing body of knowledge on hydraulic flow behavior, showing that increased discharge correlates with increased water height, as previously established by other researchers in the field.

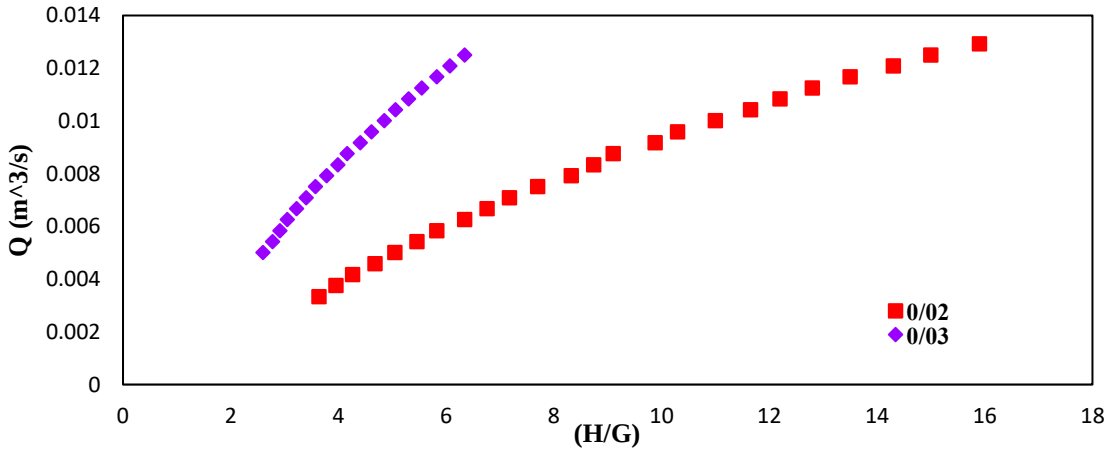


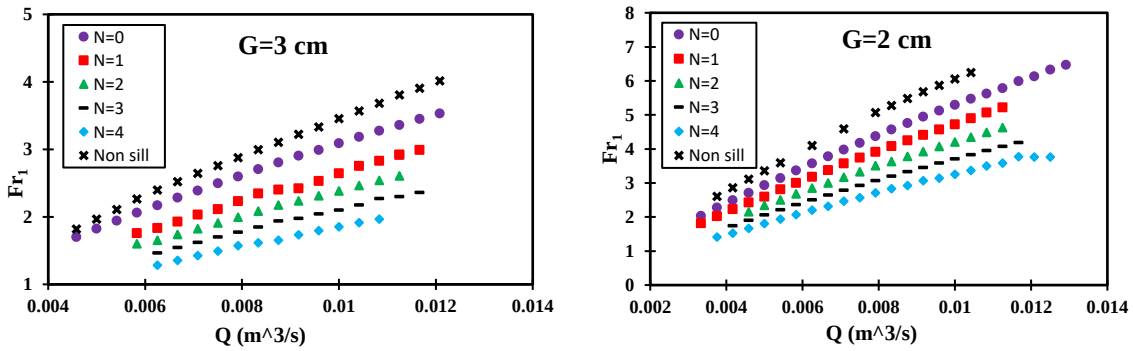
Figure 3. Graph showing the relationship between dimensionless height (H/G) and discharge for gate openings.

3.1. Downstream Froude number of the gate

In Figure 4, the gate of the downstream Froude number of the gate is shown against discharge for two gate opening heights. As observed, the use of a sill compared to the non-sill condition reduces the range of the Froude number at both gate opening heights. This occurs due to the turbulence caused by the backflow towards the sill. On the other hand, the presence of orifices and the increase in the number of orifices at the sill lead to increased turbulence and disruption of flow lines after the gate, resulting in a decrease in the Froude number of the flow at both gate opening heights. Therefore, the lowest gate of the Froude number occurs for the sill gate with 4 orifices, while the highest range of the Froude number corresponds to the gate without a sill. At both gate opening heights, the sill with 1, 2, 3, and 4 orifices reduces

the range of the Froude number by an average of 12.5%, 20.5%, 27%, and 36.3%, respectively, compared to the non-orifice condition. The sill gate without orifices also reduces the range of the Froude number by 13% compared to the gate without a sill.

Considering the gates of the Froude number at both gate opening heights, for gates with orifice sills, Type 1 and Type 4 stilling basins can be used for energy dissipation. Specifically, for the gate with orifice sills at a gate opening height of 3 centimeters, a Type 1 stilling basin can be used, while for the gate without orifices and the gate without a sill, both types of stilling basins can be utilized. On the other hand, for a gate opening height of 2 centimeters in the non-sill condition and a discharge exceeding 8 liters per second, Types 2 and 3 stilling basins are recommended. For the sill without orifices, stilling basins of Type 2 and Type 3 are suggested for discharges exceeding 10 liters per second.



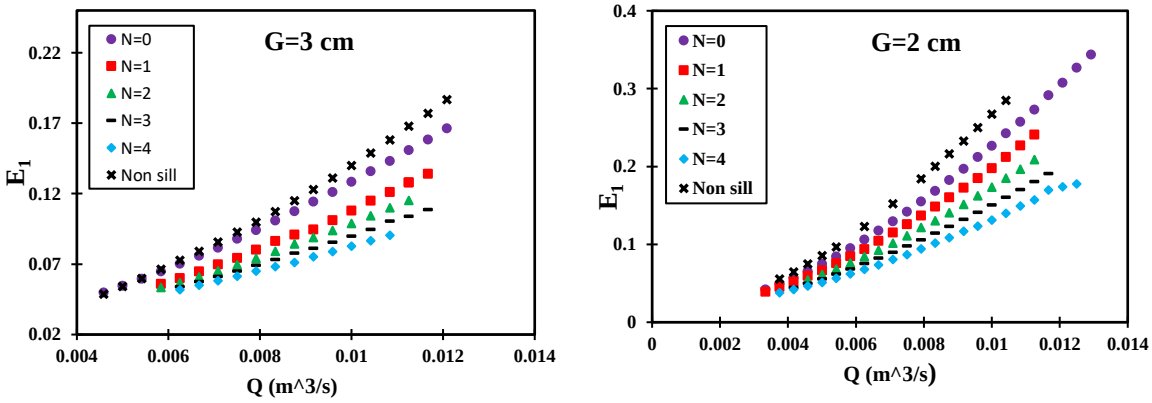
a) G=3 cm **b) G=2 cm**

Figure 4. Downstream Froude number of the gate versus discharge

3.2. Specific energy downstream of the gate

The specific energy downstream of the gate for all models in the current study is shown against the flow discharge for two gate opening heights in Figure 5. As observed, the results indicate that at both gate opening heights, with an increase in discharge, the specific energy increases, and the highest specific energy corresponds to the non-sill condition, while the lowest value is associated with the sill gate with 4 orifices. The increase in the number of orifices at the sill leads to a reduction in the specific energy downstream of the gate. The turbulence generated in the flow after the gate is one of the main causes of this phenomenon. Part of the turbulence occurs due to the backflow towards the sill, and another part is created by the flow passing through the orifices. As the number of orifices increases, the flow exiting from them interferes with each other, and this flow interference causes disruption of the flow lines and increases turbulence. Comparing the specific energy values at a constant discharge for all models shows that an increase in gate opening height also leads to a decrease in specific energy after the gate.

A quantitative comparison of the results obtained from the specific energy downstream of the gate shows that the gate with orifice sills, with 1, 2, 3, and 4 orifices, reduces the specific energy downstream of the gate by an average of 29%, 32%, 40%, and 48%, respectively, compared to the non-orifice sill. Additionally, the non-orifice sill reduces the specific energy downstream of the gate by 14% compared to the non-sill condition.

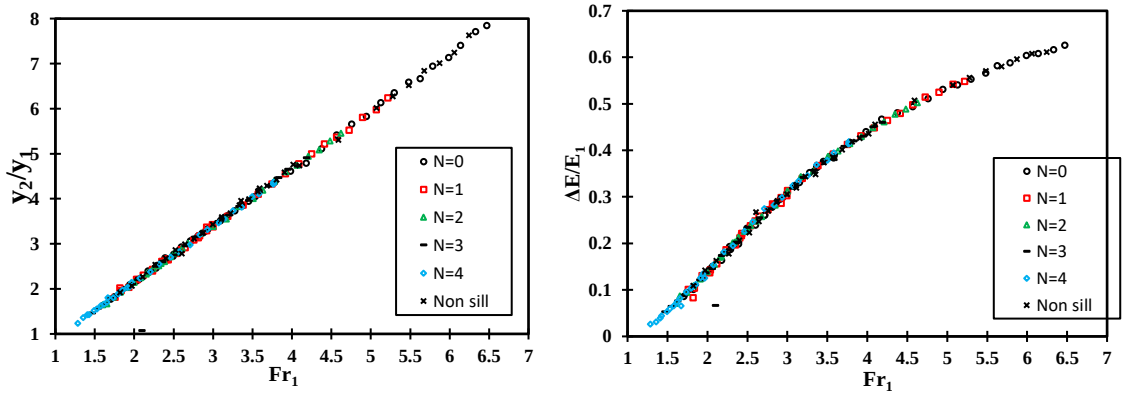


a) G=3cm **b) G=2cm**

Figure 5. Specific energy downstream of the gate versus flow rate

3.3. Depth ratio and energy consumption in hydraulic jump

In Figure 6, the gates of energy dissipation and the ratio of hydraulic jump depths downstream of gates equipped with a sill orifice are presented against the Froude number. It can be seen that the energy dissipation. It is a power function of the Froude number and increases with its increase. On the other hand, due to the fact that sills with the number of apertures 4 have a lower Froude number range than other models, it creates a lower energy dissipation range at a constant flow rate; Because a major part of the depreciation created in it happened before the hydraulic jump and by the turbulence caused by the impact of the flow coming out of the holes. Therefore, the contribution of the hydraulic jump to its energy dissipation is lower than in other models. This statement is also true for the hydraulic jump depth ratio, and it can be seen that the highest gate of depth ratio is specific to the model without a sill. Reducing the depth ratio of the hydraulic jump is important because it can reduce the height of the wall for the construction of the relaxation pond, and lead to the reduction of the materials used and the cost of the construction of the relaxation pond. On the other hand, due to the fact that the length of the hydraulic jump is a function of the Froude number and the secondary depth of the hydraulic jump, therefore, it can be said that the gate with a sill with 4 orifices, compared to other models, since the range of the Froude number and depth ratio It is less, it creates a shorter length of hydraulic jump and it will be economical in this sense.



a) Energy consumption **b) Depth ratio**

Figure 6. Energy and depth ratio in hydraulic jump

3.4. Checking the flow pattern

Examining the flow pattern and consequently the flow lines is one of the important factors in identifying the flow regime and understanding the flow characteristics. In this research, the effect of using the aperture on the sill on the flow through the sluice gate was investigated. Figure (7) shows the flow pattern governing the downstream of the sluice gate with a sill with the orifice. In the state without an orifice, smooth and unbroken flow lines dominated the flow. Because no deviation was seen. By using a sill with 2 orifices, high-speed currents were observed downstream. These lines are shown in blue in Figure (7). By using the sill with 3 and 4 orifices, the amount of high-speed currents increased, respectively. The hydraulic reason for this is the presence of small-diameter holes. With the increase in the number of gate openings, the high-speed currents in the downstream increased. The yellow lines indicate the flow lines with lower speed. These lines include currents that pass over the crest of the sill, and due to the larger orifice surface, they have a lower speed than the blue lines.

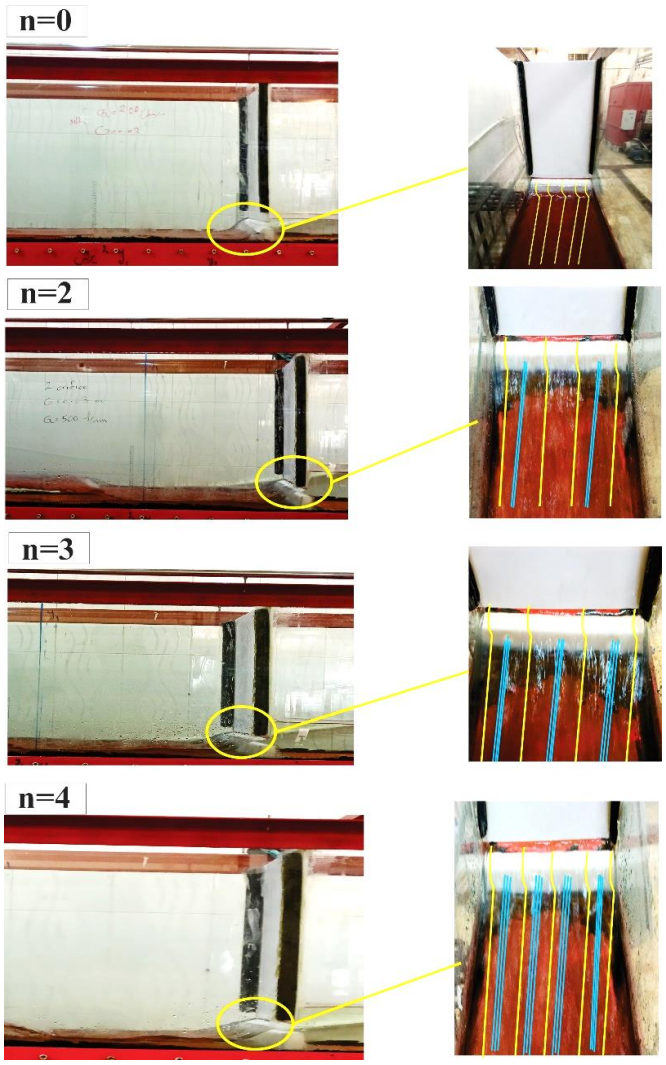


Figure 7. The flow pattern governing the downstream of the sluice gate with a sill with an orifice

4. Conclusion

In the present research, the downstream energy dissipation of a gate equipped with an orifice lower sill with two gate opening heights was investigated. Sills with fixed aperture orifices and aperture numbers 1, 2, 3, and 4 orifices were considered. The flow limit for the experiments was considered between 200 and 750 liters per minute. The results showed that due to the use of a sill under the gate, the range of landing number and specific energy downstream of the gate decreased compared to the case of non-sill, and the presence of orifice in the sill and the increase in the number of orifice also reduced the range compared to the case without a sill. Landing number and special energy after hatch. After reducing the range of Froud number, for the energy dissipation of the flow downstream of the gate, the results of the hydraulic jump formation downstream of the sill gate showed that, for sills with orifice, a large part of the energy di occurs in the section before the formation of the jump, and the sill with the number of orifice 4, it includes the lowest ratio of hydraulic jump depths. Since the consumption of energy downstream of the gate is an important and necessary thing to prevent the destruction and erosion of the bed, therefore, the use of a sill with an orifice is recommended, considering that it helps to reduce the energy of the flow before the hydraulic jump is formed.

Fundings:
This research received no external funding.

Conflict of Interest:
The authors declare that they have no conflict of interest.

Author Contributions
All authors contributed to the study conception and design.

References

1. Novak, P., Moffat, A. I. B., Nalluri, C., & Narayanan, R. A. I. B. (2017). Hydraulic structures. CRC Press.
2. Peterka, A. J. (1978). Hydraulic design of stilling basins and energy dissipators (No. 25). Department of the Interior, Bureau of Reclamation
3. Rajaratnam, N. (1968). Hydraulic jump on rough bed. Transaction of the Engineering Institute of Canada, 11 (A-2), 1-8.
4. Hughes, W. C., & Flack, J. E. (1984). Hydraulic jump properties over a rough bed. Journal of Hydraulic Engineering, 110(12), 1755-1771. https://doi.org/10.1061/(ASCE)0733-9429(1984)110:12(1755)
5. Tokyay, E. (2005). Effect of a wavy bed with relative roughness on hydraulic jump characteristics. Proceedings of the World Water and Environmental Resources Congress: Impacts of Global Climate Change, Anchorage, Alaska.
6. Cassan, L., & Belaud, G. (2008). Rans simulation of the flow generated by sluice gates. RANS Simulation of the Flow Generated by Sluice Gates, 217-225. http://dx.doi.org/10.1400/177116
7. Retsinis, E., Dimitriou, D., & Demetriou, J. (2011). Local Energy Change around Sluice Gate and Weir Flows within Inclined Channels. In Proceedings of the 3rd International CEMEPE & SECOTOX Conference, Skiathos.
8. Jalil, S. A., Sarhan, S. A., & Yaseen, M. S. (2015). Hydraulic jump properties downstream a sluice gate with prismatic sill. Research Journal of Applied Sciences, Engineering and Technology, 11(4), 447-453. http://dx.doi.org/10.19026/rjaset.11.1801
9. Abdelmonem, Y. K., Shabayek, S., & Khairy, A. O. (2018). Energy dissipation downstream sluice gate using a pendulum sill. Alexandria Engineering Journal, 57(4), 3977-3983. https://doi.org/10.1016/j.aej.2018.01.019
10. Eltoukhy, M. A. R., & Alsaydalani, M. O. (2019). Hydraulic jump characteristics downstream of a sluice gate with an orifice.

International Journal of Scientific & Engineering Research, 10(10).
11. Abbaspour, A., Taghavianpour, T., & Arvanaghi, H. (2019). Experimental study of the hydraulic jump on reverse bed with porous screens. Applied Water Science, 9, 1-7. https://doi.org/10.1007/s13201-019-1032-7
12. Daneshfaraz, R., MajediAsl, M., Mirzaee, R., & Tayfur, G. (2021). Hydraulic Jump in a Rough Sudden Symmetric Expansion Channel. AUT Journal of Civil Engineering, 5(2), 245-256. doi: 10.22060/ajce.2020.18227.5667
13. Daneshfaraz, R., Norouzi, R., Ebadzadeh, P., Di Francesco, S., & Abraham, J. P. (2023). Experimental study of geometric shape and size of sill effects on the hydraulic performance of sluice gates. Water, 15(2), 314. https://doi.org/10.3390/w15020314
14. Daneshfaraz, R., Abbaszadeh, H., Gorbanvatan, P., & Abdi, M. (2021). Application of sluice gate in different positions and its effect on hydraulic parameters in free-flow conditions. Journal of Hydraulic Structures, 7(3), 72-87. https://doi.org/10.22055/jhs.2022.39208.1196
15. Daneshfaraz, R., Majediasl, M., & Bagherzadeh, M. (2020). Experimental analysis of inclined gabion drop behavior in comparison to the standard stilling basins (USBR). Iranian Journal of Soil and Water Research, 51(10), 2531-2541. https://doi.org/10.22059/ijswr.2020.303078.668625
16. Daneshfaraz, R., Bagherzadeh, M., Ghaderi, A., Di Francesco, S., & Asl, M. M. (2021). Experimental investigation of gabion inclined drops as a sustainable solution for hydraulic energy loss. Ain Shams Engineering Journal, 12(4), 3451-3459. http://dx.doi.org/10.1016/j.asej.2021.03.013
17. Daneshfaraz, R., Majedi-Asl, M., & Bagherzadeh, M. (2023). Laboratory Study and Comparison of Gabion Inclined Drop Energy Dissipation Equipped with Vertical Screens. Irrigation and Water Engineering, 13(3), 38-54. https://doi.org/10.22125/iwe.2023.168166

© 2025 by the authors. Licensee SCU, Ahvaz, Iran. This article is an open access article distributed under the terms and conditions of the Creative Commons Attribution 4.0 International (CC BY 4.0 license) (http://creativecommons.org/licenses/by/4.0/).

Journal of Hydraulic Structures

Volume 11 – Issue 4 – October 2025

Contents:

01 Studying the impact of climate change on hydroelectric energy production (Case study: Karun 4 Dam)

Ferdous Karimi Alkoohi; Hosein Ghorbanizadeh Kharrazi; Seyyed Mahmood Jazayeri Moghaddas; Mohsen Solimani babarsad; Saeb Khoshnavaz Koumleh

16 Application of Intelligent Models in Investigating the Energy Dissipation in Labyrinth Weirs with Various Cycles Form

Hamidreza Abbaszadeh; Reza Tarinejad; John Abraham

33 Placement of data transmission equipment in the flood warning system based on the Internet of Things (case study : Jiroft Dam Basin)

Marzieh Mohseni; Amineh Naseri; leila sheikhmamoo

47 Analysis of Supply Chain Risks in Concrete Dam Construction

Mohammad Mirzaahmadi; Hamed Sarkardeh; Ali Katebi; Ayda Mirzaahmadi

57 Optimizing Minor Drainage Tunnel Position to Mitigate Groundwater Inflow in Main Tunnel Projects

Hadi Farhadian

68 An Experiment on the Effect of Sills with Orifices Under a Sluice Gate on Energy Dissipation and Hydraulic Jump

Rasoul Daneshfaraz; Reza Norouzi; Behnaz Akhondi; Mehdi Djahanghiri

Shahid Chamran University of Ahvaz